UNIVERSITY of CALIFORNIA
Santa Barbara

Nanoscale Studies of Proton Exchange Membranes under Real Operating Conditions

A dissertation submitted in partial satisfaction of the
requirements for the degree of

Doctor of Philosophy

in

Chemistry

by

Dallon James Penney

Committee in charge:

Professor Steven K. Buratto, Chair

Professor Mattanjah de Vries

Professor Horia Metiu

Professor Lior Sepunaru

March 2024

The dissertation of Dallon James Penney is approved:

Professor Mattanjah de Vries

Professor Horia Metiu

Professor Lior Sepunaru

Professor Steven K. Buratto, Chair

February 2024

Acknowledgements

To my advisor Steve Buratto, for supporting my efforts both in my research and my entrepreneurial pursuits, despite consistent failures and setbacks. To my lab mates who I have learned from and who I have had the pleasure of sharing my research with, especially Austin Barnes and YingYing Jin, who have helped me tremendously in learning the intricacies of atomic force microscopy. To all of the undergraduate and high school researchers who I mentored during my time at UCSB, from our interactions I gained a large appreciation for the value of teamwork and project planning while having fun along the way. To my lovely wife and companion Rachel, for her unwavering support, for motivating me to finish this whole thing, and for being an amazing person in general. I couldn't have asked for a better person to be quarantined with during the Covid pandemic. To all of the UCSB Chemistry Department staff and faculty, for their diligent service, kindness, and willingness to help and share their knowledge. I would especially like to thank Professors Horia Metiu, Lior Sepunaru, and Mattanjah de Vries. Professor Sepunaru was very helpful and welcoming when I first began looking at UCSB for graduate study. To my family for listening to my attempts at explaining what this research is about and for their enthusiastic support.

Curriculum Vitæ

Dallon James Penney

Education

2024	Ph.D., Chemistry, University of California, Santa Barbara
2017	Bachelor of Science, Chemistry, Brigham Young University Idaho, Rexburg,ID
2010	Sanger High School, Sanger,CA

Publications

"A 3D Printed Electrochemical Cell for Ion Exchange Membrane Nanoscale Analysis under Simulated Energy Device Conditions using Atomic Force Microscopy", Dallon Penney, Steven Buratto. *Preprint*, (2024)

"A Nanoscale Conductive AFM Investigation of Nafion under Vanadium Oxygen Fuel Cell Conditions", Dallon Penney, Steven Buratto, *Preprint*, (2024)

"Simulating the Oxidation of Methanol on Catalytic Vanadium Clusters with Density Functional Theory" Anthony Zheng, Dallon Penney, Steven Buratto, RMP Symposium Paper, (2019)

Professional Experience

Nov 2021-Jul 2023	CEO, Tesserol Inc, Goleta CA
Jan 2018-Sep 2018	Chemist 1, Freeport McMoran, Safford AZ

Abstract

Nanoscale Studies of Proton Exchange Membranes under Real Operating Conditions

by

Dallon James Penney

In this research we present the novel technology that was developed using low-cost materials and 3D printing to allow for *in operando* nanoscale investigations of perfluorosulfonic acid membranes under vanadium oxygen fuel cell (VOFC) and direct methanol fuel cell (DMFC) conditions, using conductive atomic force microscopy. We detail the process of designing, iterating, fabricating, and validating our novel 3D printed imaging cell. The justifications for the design choices are explained in detail. Heating and relative humidity control are added to the cell as additional features for more accurate environmental simulation. Using the cell, we image Nafion membranes under VOFC conditions and compare our findings with previous research. We found that thinner membranes show higher current densities than thicker membranes. Furthermore, under VOFC conditions we observe the same shrinking behavior observed in previous research as the ionic strength of electrolytes that Nafion is exposed to increases. We imaged Nafion membranes under DMFC conditions and found that the operating temperature and anode catalysts play an important role in observing nanoscale proton conductivity. Finally, we detail the process

of synthesizing low-valency vanadium/sulfuric acid electrolytes and end with an investigation into VO/TiO_2 catalysts using density functional theory. This investigation helps to explain the atomic processes occurring on a model catalyst system that can catalyze the oxidative dehydrogenation of methanol to formaldehyde.

Contents

Chapter 1

Introduction

With the need for more efficient, sustainable, and environmentally-friendly energy sources ever increasing, there has been a concerted global effort among scientific researchers to explore technologies which can harness the energy from electrochemical reactions to power our world. Fuel cells and secondary batteries are among the most commercially mature and heavily studied among these technologies[1]. Specifically, hydrogen fuel cells (HFCs) and small organic molecule fuel cells (SOMFCs) have been used to power a wide variety of applications[114], while redox flow batteries (RFBs) are helping to speed the transition to renewable energy sources by storing intermittent solar and wind power for peak use, thus helping to stabilize the electrical grid[5][79].

These two technologies have not yet achieved ubiquitous use, due to a number of factors[1]. A common barrier to adoption for both technologies is the need for a separa-

tor which forms a dielectric barrier between the anode and cathode of the device while allowing for charge-balancing ions to pass through it[1][79][114]. This separator performs critical functions for the device and is often the most costly component while also being a major efficiency and performance bottleneck[21][98]. Figure 1.1 depicts the block diagrams for a typical flow battery and fuel cell, respectively. Separation can be achieved with either a liquid or solid electrolyte, with solid being more common in RFBs than in fuel cells[98], which if employing a gas fuel, can use a water-based alkaline solution as an efficient electrolyte separator[67].

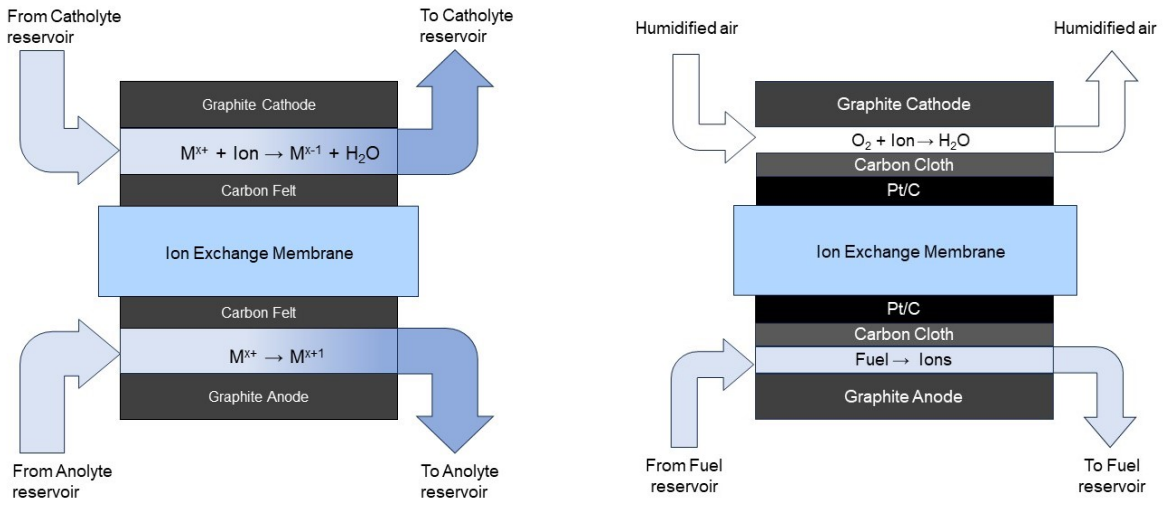

(a) (b)

Figure 1.1: Block diagrams of a typical RFB (a) and a fuel cell (b), showing the need for a charge-balancing separator membrane.

For low temperature RFBs and fuel cells, the de facto separator technology used has

been ion exchange membranes (IEMs)[79][114][41][98]. These form an electrically insulating barrier to separate the anodic and cathodic electrochemical reactions while allowing ions and water (for aqueous-dependent chemistries) to pass between the two sides[41]. For any given RFB or fuel cell, the IEM is often chosen based on its ion selectivity, ion conductivity, and its ability to withstand the operating environment of the cell over the lifetime of the device[114][98]. Polymer electrolyte membranes (PEMs) represent the most commonly used IEMs in commercial fuel cells and RFBs[114][41][98]. These materials are most often composed of a polymer backbone that has been either chemically modified with charged pendant side chains, or mixed with a ionically-conductive substance. Common monomers used to form the polymer backbone of these materials include tetrafluoroethylene, benzimidazole, phthalazinone ether ketone, and fluorenyl ether ketone.

Nafion is the most commercially successful polymer electrolyte membrane to date, having had widespread use in HFCs, SOMFCs, and RFBs owing to its durability, chemical stability, and high ion conductivity[84][94]. Due to its ubiquity and the plethora of studies focused on it, we chose to base the majority of our investigations on Nafion membranes in the context of RFBs and fuel cells. The purpose of this study is to widen our scientific understanding of the structure-function relationship of Nafion under a variety of hitherto-unstudied environmental conditions, using state-of-the-art metrology techniques as well as novel instrumentation development. The knowledge gained from this study can lead

to IEMs that are tailor-suited to the electrochemical cell that they are designed for, which can increase efficiency, thus lowering the barrier to widespread adoption. Nafion is often sold as a solution cast sheet of dried polymer, with the basis weight and thickness identified using a numerical designator, as seen in Table 1.1

Membrane	Basis Weight (g cm^{-2})	Thickness (µm)
N211	0.005	25
N212	0.01	50
N115	0.025	127
N117	0.036	183

Table 1.1: Commercial Nafion membranes numerical designators, their basis weights, and thicknesses.

1.1 Nafion Review

The overall bulk structure of Nafion under hydrated conditions has been the focus of many different studies[84]. Nafion is synthesized via the copolymerization of a perfluorinated vinyl ether co-monomer with tetrafluoroethylene, and when cast from solution into a thin film forms a highly complex matrix of negatively charged, water-filled tubes surrounded by hydrophobic polytetrafluoroethylene (PTFE) domains. Figure 1.2 depicts the chemical structure of a Nafion monomer unit. Nafion is considered a random co-polymer, with the sulfonic acid-terminated pendant side chains occupying the PTFE backbone at random intervals. Protons have been theorized to conduct through the water-filled, anionic channels via a Grötthus type mechanism, where protons "hop" between hydronium

molecules through the channels[93]. The diameters, connectivity, and behavior of these channels have been studied extensively with a variety of techniques and theoretical approaches, which we will briefly discuss.

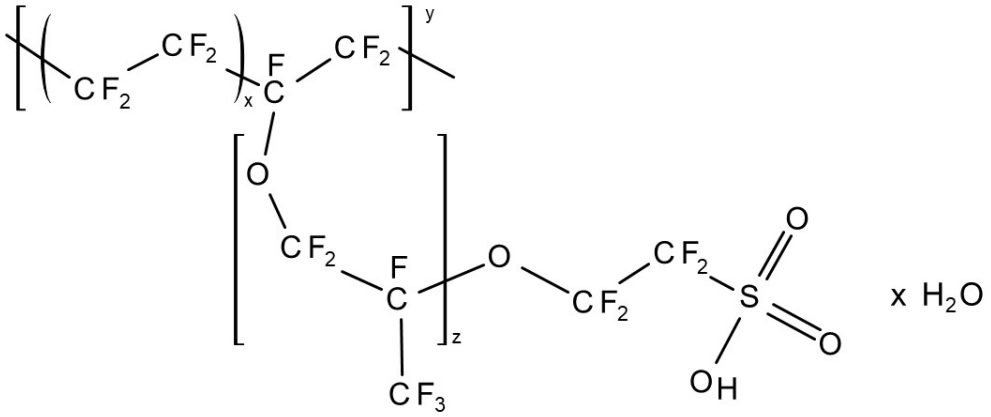

Figure 1.2: Structure of Nafion random co-polymer, with x, y, and z representing the different polymer unit ratios.

Early studies of the bulk structure of Nafion used small angle X-ray or Neutron scattering (SAXS/SANS) techniques, where the scattering angle theta of the incident beam produces an "ionomer peak" as measured by Gierke et al at $q = 2\pi/(\lambda Sin(\theta))$, where λ is the incident beam wavelength, θ is the scattering angle, and q is the measured intensity of the scattered beam[42]. This data was used to propose a "spherical inverted-micelle water clusters" model of Nafion by Gierke where the cluster diameter was inferred from the bragg spacing $d = 2\pi/q$ (4nm) as measured using SAXS[42]. This model

has since been revised by Schmidt-Rhor and Chen using their parallel cylindrical water channel model which takes into account the crystallinity of Nafion to more accurately reproduce a wide range of Nafion SAXS data using a Fourier transform approach[104]. In their model the structure of Nafion resembles parallel channels of inverted micelles or "pores", surrounded by semi-crystalline hydrophobic domains, with the diameter of these proposed channels being between 1.8-3.5nm. While these techniques have provided valuable insights into the structure of Nafion, they fail to capture the dynamic nature of this material under real operating conditions.

1.2 Atomic Force Microscopy as a Tool for Studying Nafion

Atomic force microscopy (AFM) has proven to be a powerful tool in determining both the surface and bulk structure of Nafion as well as the material properties under variable conditions[84][73][85]. Briefly, AFM is a scanning probe microscopy technique which measures the interactions of a sharp tip and a material surface, which can be used to spatially resolve the material surface height variation beyond the diffraction limit of visible light. The AFM tip can interact with the surface in a myriad of ways: electrostatically[20], electrochemically[66], thermally[111], and mechanically[18], to name a few. The wide variety of nanoscale analysis techniques make AFM a powerful tool in studying surfaces with dynamic properties.

The first investigations of Nafion using AFM were taken by Lehmani et al in 1998: they used tapping mode to study the surface of Nafion 117[73], where they studied the basic surface morphology and roughness parameters. Later AFM studies by McLean et al and James et al in the early 2000s explored the capability of AFM to differentiate the ionic cluster domains of Nafion using tip-surface interaction[85][56][57]. These investigations revealed new insights into the co-polymer surface arrangement under different hydration conditions as well as the formation of a fluorine-rich barrier surface layer. The first use of conductive AFM to study the ionic conductivity of Nafion were performed by Kazuaki and Siroma in 2005, where they used a Pt-coated cantilever to oxidize hydrogen gas on a Nafion film with a negative tip electrical bias, which allowed them to resolve the proton conducting regions on the surface[109]. Their analysis revealed a disparity between the predicted bulk proton conducting channel diameter and those on the surface, with the latter being much larger than predicted (5nm vs 50nm).

Our research group first published a study on the conducting channels of Nafion using AFM in 2007, where David Bussian and James O'dea fabricated half of a hydrogen fuel cell membrane electrode assembly (MEA) by hot-pressing a platinum coated carbon cloth electrode to a sample of Nafion 117, which was then loaded onto a copper flow cell to which hydrogen gas was fed while imaging the Nafion in both contact and tapping mode[19]. They showed that a Pt-coated AFM cantilever can be used as an oxygen

reduction cathode to drive an electrochemical potential between the tip and a platinum coated hydrogen oxidation anode, with the Nafion membrane acting as a proton conducting barrier separating the two reactions, thus simulating a hydrogen fuel cell within the AFM. Using this technique, our group showed that the relative number of conducting ionic domains can be resolved on the surface as a percentage of the total observable ionic domains[19]. As first demonstrated by James et al[56], the AFM phase contrast channel can distinguish the ionic clusters on a Nafion surface from the semi-crystalline hydrophobic domains based on the differences in probe-sample adhesion. When in intermittent contact tapping mode, the tip feels a larger attractive force from the water-rich ionic domains and a subsequent larger power dissipation when close to the surface, which when in the repulsive regime results in a sharp phase contrast from the ionic regions on the surface. James O'dea from our research group showed that the phase-ionic cluster correlation depends on the tapping mode regime: when in attractive mode (< 90 degrees) the phase correlates closely with the topography- areas of high tip-sample interaction appear as negative amplitude phase shifts, while in repulsive mode (> 90 degrees) areas of high tip-sample interaction appear as positive amplitude phase shifts[92]. Repulsive mode occurs at smaller tip-sample distances which can allow for intermittent tip-sample contact at the cost of slightly lower phase-domain correlation resolution[92]. Attractive tapping mode is essentially a non-contact technique, which requires any current data to be collected separately from the height and phase data, usually in contact mode[19][35].

The 2007 study published by our research group was among the first to use a Pt-coated cantilever to catalyze the oxygen reduction reaction in order to image proton conductivity in Nafion and correlate it with the phase-contrast ionic domain images[109]. This study helped to elucidate the structure-function relationship of Nafion under hydrogen fuel cell conditions by measuring the relative number of active channels, which at only 40%, led to the conclusion that channel connectivity and access to active catalyst sites were the major factors in determining channel conductivity[19]. This study paved the way for future research into IEMs using conductive probe atomic force microscopy (cp-AFM): our group went on to publish the results of cp-AFM studies on other IEMs including hydroxide conducting polymer exchange membranes[10], utilizing the techniques pioneered in the 2007 study. These, along with many other studies[120][50][51][52][4][3] have shown the veracity of AFM as a tool to study IEMs under real electrochemical energy device conditions.

1.3 Vanadium Redox Flow Battery Review

Vanadium Redox Flow Batteries (VRFBs) are a promising secondary battery technology which takes advantage of the four stable oxidation states of vanadium in solution: V^{2+}, V^{3+}, VO^{2+}, and VO_2^+[110]. The battery architecture separates these via a dielectric H^+/water permeable separator into two reversible redox pairs, with $V^{2+}\backslash V^{3+}$ on one electrode and $VO^{2+}\backslash VO_2^+$ on the other electrode. In reference to the standard hydrogen electrode (SHE), the reversible redox reactions are separated by 1.26V:

$$V^{2+} \longleftrightarrow V^{3+} + e^{-} \text{ (-0.26V vs SHE)} \tag{1.1}$$

$$VO_2^{+} + 2H^{+} + e^{-} \longleftrightarrow VO^{2+} + H_2O \text{ (+1.00V vs SHE)} \tag{1.2}$$

However, real operating voltages of fully charged VRFBs are usually lower than this due to kinetic barriers at the electrodes[102] and ohmic losses[75]. As an RFB, VRFBs are usually comprised of three separate, integral components: a pair of external electrolyte reservoirs which hold the dissolved vanadium ions in a conductive electrolyte (usually H_2SO_4), a stacked group of electrochemical cells in series where the redox reactions take place, and a hydraulic system for moving electrolyte through the battery to either store or extract electrical energy. Figure 1.3 depicts a block diagram of a typical VRFB architecture.

VRFBs can play a key role in the renewable energy transition[79], providing a scalable system to store peak renewable energy sources for use during highest electrical demand[83]. They have the following advantages over incumbent Li-ion grid-scale batteries:

- **Scalability.** Due to using aqueous electrolytes to store electrical energy, the capacity of the battery is decoupled from the power and can be scaled by simply increasing the external electrolyte tank volume.
- **Long life.** VRFBs can have operational lifespans of over 12,000 cycles[116], as compared to residential Li-ion having lifetimes of around 5,000 cycles[12].

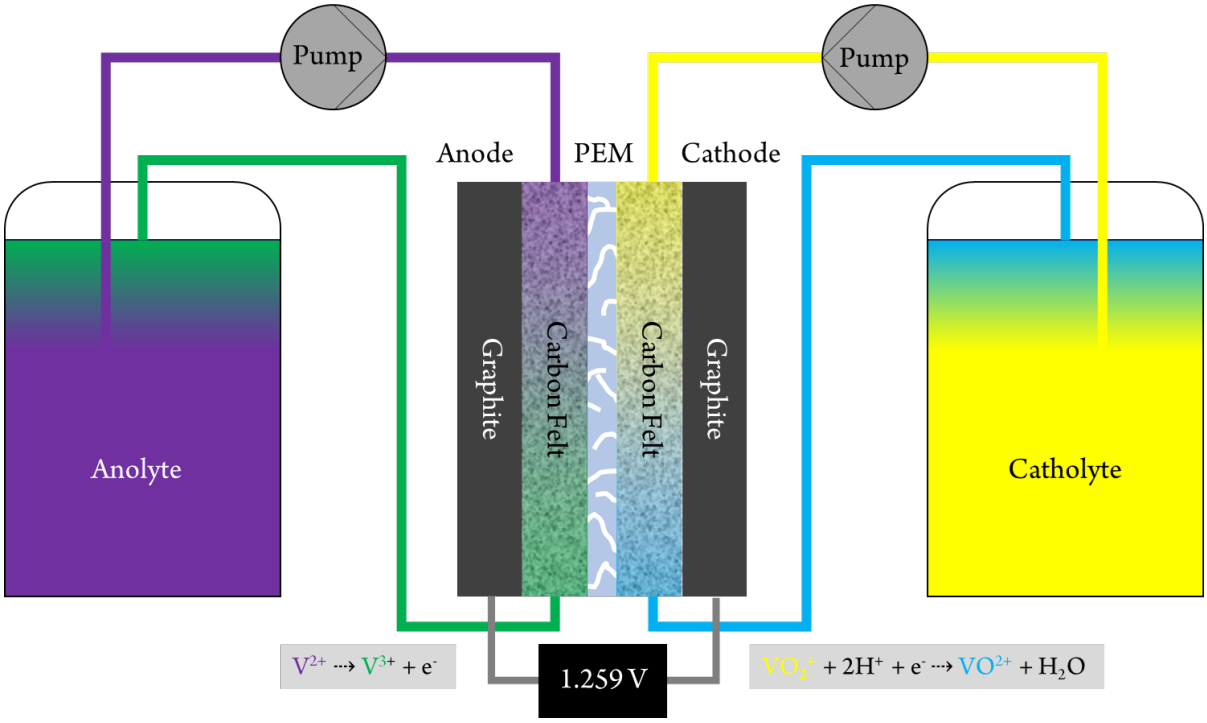

Figure 1.3: A schematic block-diagram of a typical VRFB, showing the cathodic and anodic reaction during discharge as well as the physical arrangement of the various components including the cell, pumps, and reservoirs.

- **Low Fire Hazard.** Due to using aqueous electrolytes, there is no risk of fire or thermal runaway in the case of cell failure, as opposed to Li-ion[24].

Unfortunately, VRFBs have several disadvantages, including:

- **Self-discharge.** Due to vanadium ion crossover through the ion-conducting membrane, VRFBs are prone to self-discharge over time[80][113].

- **Electrolyte hazards.** The electrolytes used contain dangerous concentrations of corrosive acids.

- **Low energy density.** Due to solubility constraints[89], the energy density of standard sulfuric acid-based VRFB electrolytes is limited to ∼20-30 Wh L^{-1}[124],

compared to a typicle Li-ion battery pack having 200-500 Wh L^{-1}[6].

Much of the research surrounding VRFBs has focused on the IEM, with the goal of improving the operational efficiency and reducing self-discharge[98][74][59]. The standard IEM used for VRFBs in Nafion, due to its high chemical stability and high proton conductivity[98][46]. One of the main goals of this research is to study the structure-function of Nafion at the nanoscale while under the operating conditions of a typical VRFB, as the following chapters will elucidate.

1.4 Overview of Thesis and Project Goals

This work is built on the experimental and theoretical framework established by the previous researchers in our group as well as other early IEM investigators using AFM techniques[92][35][120][50][51][52][4][3][10]. With our group having shown the utility of AFM investigations of IEMs under HFC conditions, we began this project with the overall aim to extend our capabilities to study IEMs under a variety of electrochemical device conditions, with the main goal being to simulate the conditions of a vanadium redox flow battery in order to study the structure function relationship of IEMs while under those conditions. Thus, the main scientific endeavor of this work is to uncover the structure-function relationship of Nafion under real device operating conditions, with the focus on RFBs and SOMFCs.

In terms of AFM data, we were interested in collecting *in operando* height, phase,

and current, which would allow us to determine the relative number of IEM conducting channels and correlate them with surface morphology as a function of environmental variables. Further studies could make use of the metallized cantilever as the working electrode for potentiostatic measurements of the IEM surface. This could allow for single ionic domain nanoscale characterization techniques including ion flux measurements using linear sweep voltammetry and/or electrochemical impedance spectroscopy.

To simulate the electrochemical environments (VRFBs) we were interested in studying, we went through the process of designing, fabricating, and validating a novel electrochemical imaging cell. This cell was used to study the surface morphology and ionic domain sizes of Nafion while exposed to various dilute acid solutions and VRFB electrolytes. Using the cell and the AFM's ability to simultaneously map surface height, tip-sample amplitude phase shifts, and tip-sample current, we studied Nafion under vanadium-oxygen fuel cell conditions to determine how exposure to V^{2+}/H_2SO_4 electrolyte effects Nafion's ionic domain size and conductivity distribution as compared to HFC or SOMFC conditions. Using our technique, we studied the effect on the ionic domain size and conductivity distribution of Nafion under methanol fuel cell conditions and compared our results with our previous findings. Statistical analysis was performed on data obtained of Nafion under various conditions to draw conclusions about the structure-function response under variable operating conditions. The results from this study could prove useful to future researchers interested in studying materials at the nanoscale under

real device operating conditions.

The supplementary chapters detail the process of making low valency vanadium electrolyte solutions as well as a separate investigation that was made into vanadium oxide clusters on a rutile titanium oxide surface for the catalytic oxidation of methanol to formaldehyde using ab initio computational packages. This was done in support of experimental data obtained on the same set of conditions using scanning tunneling microscopy and was accomplished through collaboration with other researchers.

Chapter 2

Imaging Cell Design, Development, and Validation

2.1 Introduction

Taking into consideration the scientific goal of the project: simulating VRFB conditions inside of an AFM to study the structure-function relationship of IEMs at the nanoscale, in this chapter we first overview the current state of knowledge regarding IEMs under VRFB conditions. This review helps to frame the project among various efforts to better understand IEMs and their performance in VRFBs. Furthermore, in this chapter we lay down the practical and theoretical approaches taken in designing and fabricating the first imaging cell prototypes for this project. We begin with a brief overview of IEMs in the context of VRFBs in general, the issues surrounding their performance, a look into the

previous investigations made into Nafion both physical and theoretical (in VRFBs) and build towards the justification of the need for our nanoscale investigation. The constraints around the project are enumerated. We detail the design and validation of the successive iterations of our novel AFM imaging cell, along with considering what aspects of a VRFB should and should not be included in the cell design from a theoretical and practical standpoint. We end the chapter with details on how temperature and relative humidity control features were added to the imaging cell.

2.2 The Role of Membranes in VRFBs

IEMs play a pivotal role in both the development and commercialization of VRFBs, being identified as one of the largest barriers to higher performance and market adoption[98]. IEMs fulfill several requirements for proper battery cycling including:

- **Charge balance.** IEMs must allow protons to migrate across the cell during cycling. Protons are consumed and produced at the cathode.
- **Separation.** IEMs must form a dielectric barrier between the anode and cathode and prevent the electrolytes from mixing.
- **Water management.** IEMs must maintain water balance between the electrolytes when osmotic gradients form during cycling.

The performance of the VRFB is directly tied to the IEM, which is the main bottleneck in terms of current density and coulombic efficiency[98][108][105][115][46][31]. A perfectly

optimized IEM for a VRFB would have the following properties:

- **Chemical stability.** owing to the corrosive nature of the sulfuric acid and oxidative nature of $VO_2{}^+(V^{5+})$ ions, the membrane must be able to withstand degradation and\or loss of function over the operational lifespan of the battery.

- **Proton conductivity.** high proton conductivity allows for faster charge and discharge cycling and improves overall efficiency.

- **Ion selectivity.** chemical potential and osmotic drag are the driving force for vanadium ions to diffuse through an IEM during operation, leading to self-discharge. Thus, IEMs which have high proton selectivity and low vanadium ion permeability are preferred.

- **Low cost.** Due to the grid-scale niche that VRFBs fill, many square meters of IEM are needed per installation. Thus, costs must be kept to a minimum.

2.2.1 Nafion in VRFBs

While there has been significant research invested into new IEMs and separators for VRFBs, the most studied and commercially adopted is Nafion[98]. Having covered much of the previous work done on understanding the bulk and nanoscale structure of Nafion ex situ and in the context of hydrogen fuel cells in the previous chapter, this chapter's focus on Nafion is in the context of VRFBs. Nafion fulfills two of the four requirements for an optimal VRFB separator:

- High thermal and chemical stability owing to the large C-F bond energy (485 kJ/mol) inherent in Nafion's tetrafluoroethylene backbone.

- High ion exchange capacity and proton conductivity owing to its unique anionic channel structure (See Figure 1.2).

Unfortunately, Nafion fails in the other two categories; the cost of Nafion has remained high since its invention, with a US OSTI report citing the cost of Nafion as being one of the biggest hurdles for the adoption of HFCs in the automotive market[55]. In estimating the cost of a VRFB cell stack, Nafion accounts for ∼30-40% of the total cost[105][118]. Nafion also has poor ion selectivity; Multivalent vanadium ions have solvated diameters (∼0.6nm)[61] smaller than the lower estimates of the channel diameters of Nafion (∼1.5nm)[104]. Density functional theory studies on the interaction of vanadium ions with Nafion have shown spontaneous coordination of SO_3^- terminal acid groups with solvated vanadium ions: Intan et al estimated SO_3^- attachment energy barriers for V^{2+} and V^{3+} as 0 eV and barriers for VO^{2+} and VO_2^+ as >0.3 eV using canonical ensemble Car-Parrinello molecular dynamics (CMPD)[54]. Several groups have experimentally measured vanadium ion flux through Nafion, with measurements ranging from ∼1-8 µmol h^{-1} cm^{-2}, depending on ion valency and experimental setup[28][65][72]. A VRFB optimized IEM must strike the perfect balance between chemical stability, proton conductivity, ion selectivity, and cost. Thus, understanding the structure-function relationship of Nafion under VRFB conditions can inform the development of VRFB optimized IEMs and/or uncover new routes to mitigate the vanadium ion permeability of Nafion.

2.2.2 The Structure-function of Nafion in VRFBs

Our current understanding of the relationship between the operating conditions of a VRFB and the performance of IEMs have been made almost exclusively with bulk measurements[98][108][46]. IEM conductivity and resistivity in VRFB single cells has been measured using potentiometric techniques including electrochemical impedance spectroscopy (EIS)[119][58]. Other bulk measurements include titration to determine ion exchange capacity[108][59], and the use of a diffusion cell to measure ion permeability[65][58]. Nafion represents the perfect test subject for our study as there are currently no investigations that have looked at its nanoscale structure-function relationship under VRFB operating conditions *in operando* or *in situ* despite it being the most commonly used IEM for VRFBs.

While measuring ion crossover at the nanoscale is within our ability, it is not the focus of this research. We are more interested in the channel connectivity, conductivity, and morphology of IEMS at the nanoscale under VRFB conditions. As explained in an earlier chapter, our group has previously used AFM to study the structure-function relationship of IEMs under simulated hydrogen fuel cell conditions[19][35]. These studies gave insights into the relationship between IEM channel connectivity, conductivity, and morphology as a function of relative humidity, IEM formulation, and environmental conditions.

2.3 AFM Imaging Cell Design

Figure 1.3 (see Chapter 1) depicts a cross section of a typical VRFB battery, with graphite current collectors, carbon felt electrodes, PEM, pumps, and electrolyte storage tanks. We approached the design of our first prototypes with the goal of simulating as many aspects of a true VRFB system as possible while staying within the constraints placed on the project, which proved to be both difficult and unnecessary, as we will later show.

Like the previously used modified polyheater cell (see Figure 2.4) which simulated a HFC half-cell, the cell needed to be constructed in a similar way so that the IEM forms a barrier in the AFM imaging plane between the metallized cantilever and a VRFB "half-cell". To this end we planned to incorporate a system with an external reservoir for supplying fresh electrolyte to the cell during imaging, a fluid pumping system to move the electrolyte, and an interface which would allow for a small carbon felt electrode between the cell and an IEM sample. This was analogous to the approach that our group had taken in simulating an HFC for AFM studies: an Asylum research polyheater cell was modified to house a HFC half-membrane electrode assembly, with hydrogen gas fed from an external tank to the cell through added tubing. Since we were breaking new ground in instrumentation development for the AFM available to us, we did not have any references to study as a starting point beyond the modified polyheater cell previously mentioned.

2.3.1 Design Constraints

The first thing we considered were the design constraints. Foremost among these for the cell was preventing oxidation of V^{2+} via contact with atmospheric oxygen. Any material that is water-tight is naturally air-tight, so the cell body itself posed few concerns in this regard. The main sources of oxidation were identified to occur from leaks in the system connections, air exposure during sample preparation, and from oxygen diffusing through the membrane during data collection[88]. During sample preparation, V^{2+} electrolyte must be transferred from a separate container to the imaging cell without encountering air. Having a way to load the cell with an IEM sample and then add the electrolyte secondly would have been ideal as it would preclude having an open reservoir of V^{2+} electrolyte that would have to be sealed in place with the IEM. We did not have access to a glove box in our laboratory, but we procured "glove bags" which are described in Appendix A. These would let us load samples with V^{2+} electrolyte in an oxygen-free environment. The only way to practically limit oxygen diffusion through the IEM after loading the electrolyte was to make the IEM area as small as possible to limit the surface area. However, the IEM area needed to be large enough so that the edges could be sealed to prevent electrolyte leaks, and to have enough room so that the counter electrode was surrounded by sufficient electrolyte. We were working under the assumption that capillary action would naturally draw the electrolyte between the electrode and the IEM as it was pumped into the cell. Furthermore, the AFM cantilever holder needed adequate space to approach the sample without crashing into any of the cell components, which

also placed a limit to how small the IEM area could be.

The corrosive/oxidizing nature of VRFB electrolytes placed tight constraints on the types of materials that could be used to build the cell. The material chosen would need to be easy to work with and resist attack from electrolyte. Metals would have to be avoided mostly due to needing to avoid contamination of the electrolyte due to ion dissolution, as studies have shown that dissolved metal ions can have substantial effects on VRFB performance[95]. For our first prototypes we gravitated towards thermoplastics, in particular high density polyethylene (HDPE), as these were relatively inexpensive and easy to work with.

The next constraint is the spatial limitations of the AFM imaging stage. Figure 2.1 is a CAD drawing made of the center of the AFM imaging stage with the dimensions shown in mm. The central cavity in the stage and the available space between the stage and the scanner are the most important constraints; The cell must sit between the scanner head and the stage, leaving plenty of room for the scanner to move without crashing into any part of the system. Ideally, the entire system should fit within the available volume. With the initial goal of having external pumps and reservoirs there would be auxiliary systems which would need to be located adjacent to the AFM.

The final and perhaps most important constraint was our budget. The system was

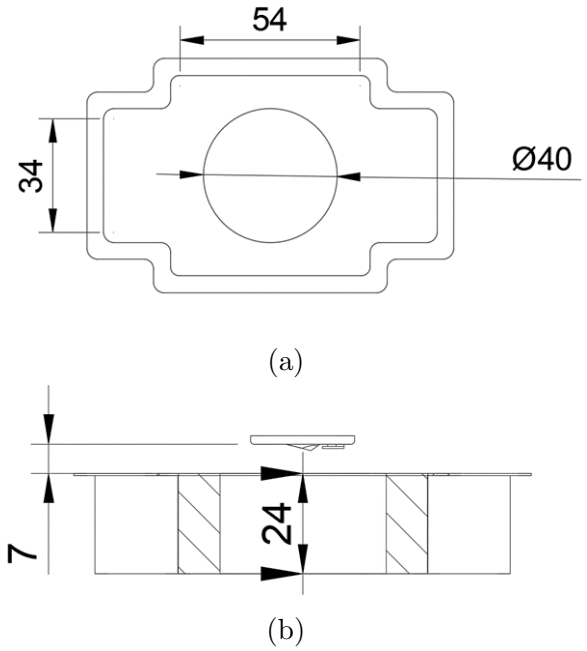

Figure 2.1: (a) Top-down view CAD drawing of the AFM imaging stage with units shown in mm. (b) Cutaway side view of the AFM imaging stage along with the AFM scanner shown above it. The 7mm gap corresponds to the maximum space available between the scanner and the stage.

not so abstract or technically challenging as to pose an issue for an experienced machinist or CAD designer, but needing to rely on outside services to design and fabricate the many iterative prototypes would incur large costs. Furthermore, we planned on starting with simple systems and gradually adding on more control and measurement capabilities to the system through successive iterations, which would prevent us from pouring our resources into a single design. Thus, both to save money and to further our understanding, we relied heavily on our in-lab fabrication capabilities which included access to a small desktop CNC machine and two 3D printers- a fused deposition modeling (FDM) printer and a mono stereolithography apparatus (MSLA). All the 3D CAD modeling was done using Fusion 360 from AutoDesk, using a student license. Most of the budget was allocated

for the purchase of reagents, raw materials, AFM cantilevers, and electronics. It is worth nothing that the role of 3D printing in scientific research has grown tremendously over the past decade as it allows for rapid prototyping using a huge variety of materials with a wide range of properties[106].

2.3.2 The Vanadium-Oxygen Fuel Cell Starting Point

Considering our constraints, the simplest starting point was to replace the cathode $VO^{2+}/VO_2^+(V^{4+}/V^{5+})$ redox couple with an oxygen reduction reaction while keeping the V^{2+}/V^{3+} redox couple at the anode. This allowed AFM imaging in air which greatly simplified the data collection. Having an air cathode served as a good starting point because it still forced us to tackle the problem of having a vanadium oxidation reaction drive a faradaic current between the cell and the AFM tip while not requiring any modifications to the AFM, specialized cantilevers, or corrosion resistant scanning heads. Furthermore, we could use the same imaging techniques used in previous investigations on IEMs in HFCs. Other problems we would tackle with this approach included how to expose an IEM to a V^{2+} electrolyte inside the limited area of the AFM imaging stage while preventing leaks, V^{2+} oxidation from air, and imaging artifacts.

While this system cannot be considered a true analog of a VRFB cell, it is an acceptable model system and valuable data could still be collected and analyzed. The prototype would use the model system of a vanadium-oxygen fuel cell (VOFC), which

has been studied by several groups to overcome the low energy density of VRFBs due to the absence of the V^{5+} ion which precipitates into V_2O_5 out of solution above ~1.5M[25]. V^{2+} and V^{3+} have wider solubility windows and concentrations of up to 3.6M have been reported[100], more than doubling the energy density versus true VRFB chemistry. Furthermore, VOFCs have a higher theoretical cell voltage (1.49V vs 1.23V) and require half the volume of electrolyte of a VRFB.

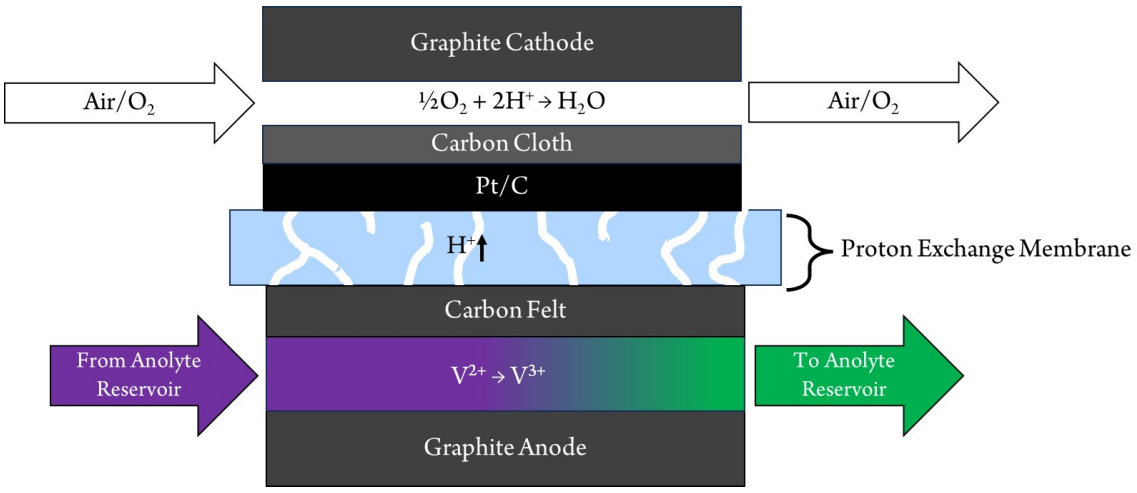

Figure 2.2: Block diagram of a typical VOFC, showing the anodic and cathodic reactions as well as the proton conducting membrane which separates them.

Figure 2.2 depicts a cross-section of a VOCF cell. Much of the research in VOFCs has focused on preventing vanadium diffusion through the IEM to the cathode[88][23], preventing oxygen diffusion to the anode[88][23], studying bifunctional ORR/OER cathode catalysts to allow for 'recharging' the vanadium electrolyte[100], and further increasing the concentration of V^{2+}/V^{3+} electrolytes with stabilizers[100]. It was found that the major source of coulombic efficiency loss in a VOFC is due to oxygen diffusing through

the IEM and reacting with V^{2+} in the electrolyte[87][88]. Besides the need for a bifunctional air cathode, the main limiting factor for VOFCs is the IEM, for many of the same reasons as in VRFBs[23]. Our focus will mainly be on the IEM.

From this starting point, we would gain valuable insight into the best design and fabrication approaches as well as what should and should not be kept as part of the final design. After completing the basic VOFC cell we planned to add the following features:

- **Temperature control.** IEMs respond to temperature changes under HFC conditions26 but it is unknown how they respond under VOFC conditions at the nanoscale. Adding a heating element and temperature sensor would allow us to study this relationship. VRFBs have a narrow operating temperature range and thus temperature studies would provide fewer insights than in the case of a VOFC or another temperature-dependent device.

- **Relative humidity control.** Adding connections which would allow gas to flow over the IEM sample during AFM imaging, thus allowing for streams of gas with different relative humidities to influence the IEM.

Once these control features were validated using the VOFC cell, we planned to simulate a true VRFB cell by making the following changes:

- **PEEK scanner.** Procuring a polyether ether ketone (PEEK) corrosion resistant cantilever chip holder from Oxford Instruments would allow us to scan in either of the VRFB electrolytes.

- **Insulated cantilevers.** If we attempted to perform cp-AFM in VRFB electrolyte using a regular metallized cantilever, the charge transfer would not be localized to the tip, thus we would need to procure specialized cantilevers which on top of being metallized have a dielectric and corrosion resistant coating everywhere except for the tip.

Using these two changes we could simulate a true VRFB environment in an AFM, as shown in the diagrams in Figure 2.3. Because of this most of the early prototypes included a ring of material surrounding the sample, like the polyheater design (See Figure 2.4), with the idea being that this would be filled with electrolyte once the changes were made and thus, we would not need to modify the hardware of the cell.

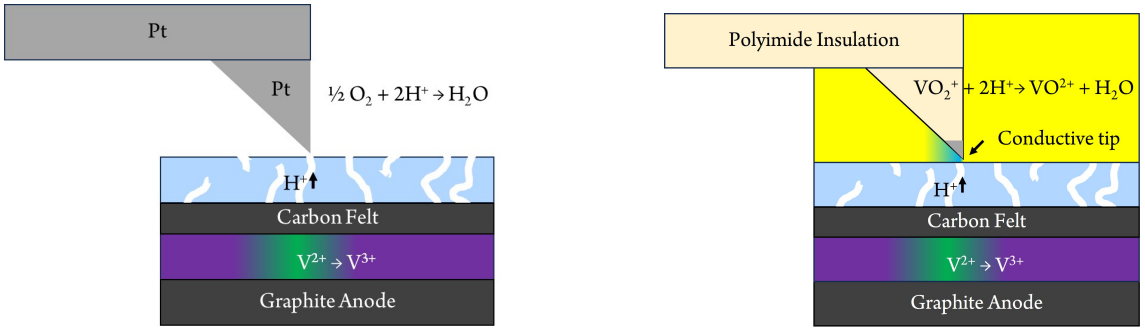

(a) (b)

Figure 2.3: (a) Block diagram of the AFM cantilever acting as the cathode in a nano sized VOFC. (b) Block diagram of a polyimide insulated cantilever with an exposed, metallized tip acting as a cathode in a nano sized VRFB.

2.3.3 Cell Design Approaches

Using the modified polyheater cell as a starting point, we needed to implement some fundamental changes to the approach used in its original design to stay within the constraints on the project. Specifically, we needed a new way to seal an IEM sample, a new way to introduce reactants (electrolyte), and a new way to make electrical contact with the sample via an external bias wire. Figure 2.4a depicts a cutaway view of the original modified polyheater cell, showing the bias wire placement as well as how H_2 gas was fed to the half-MEA. Figures 2.4b and 2.4c are pictures of the modified cell.

Membrane Sealing

For sample preparation, the constraint to prevent V^{2+} oxidation led to the conclusion that it would be better to have the IEM sample mechanically sealed to the cell before adding the electrolyte. This contrasts with how HFC half-MEAs samples were prepared for the modified polyheater cell; samples were hot-pressed onto a stainless-steel puck which was then fixed to the cell with small screws, as seen in Figures 2.4 and 2.5a. The puck had two holes which aligned with the cell which could feed hydrogen gas to the half-MEA. The hydrogen gas fed to the puck was at a low enough pressure so that the adhesion between the IEM and the stainless steel was sufficient to hold it in place. This would not work for the VOFC half-cell- the IEM sample will swell when it encounters the electrolyte causing it to delaminate from the puck.

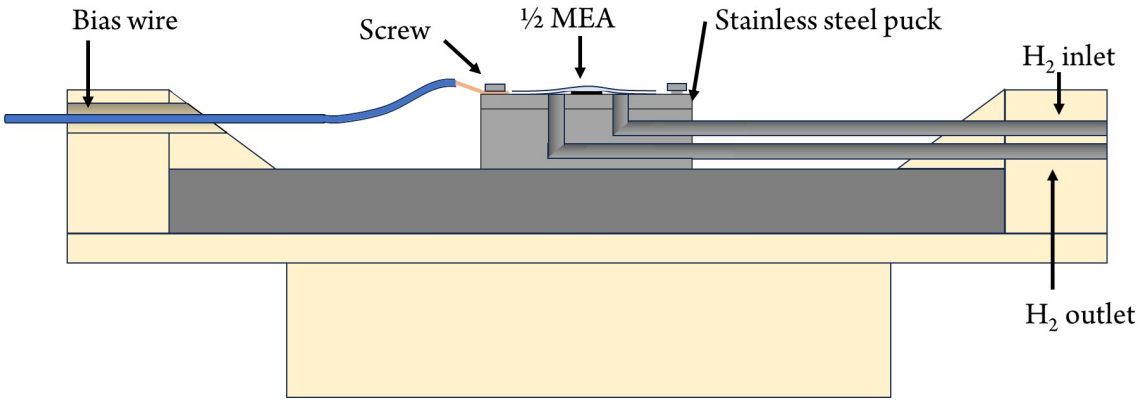

(a)

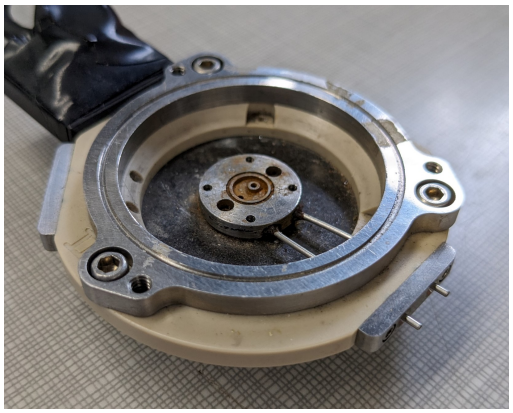

(b)

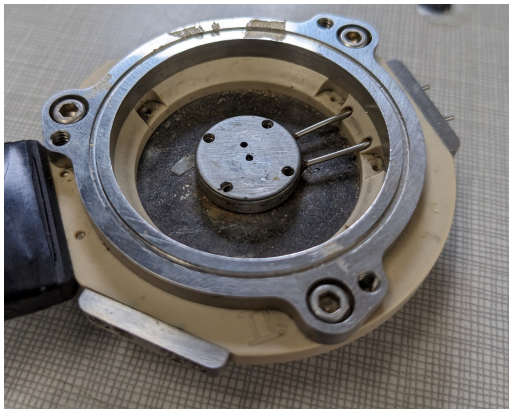

(c)

Figure 2.4: (a) Cutaway side view of the modified polyheater cell used to simulate a hydrogen fuel "half-cell". (b) Photograph of the cell in (a), showing the exposed plumbing. (c) Photograph of the cell in (a), with the stainless-steel puck.

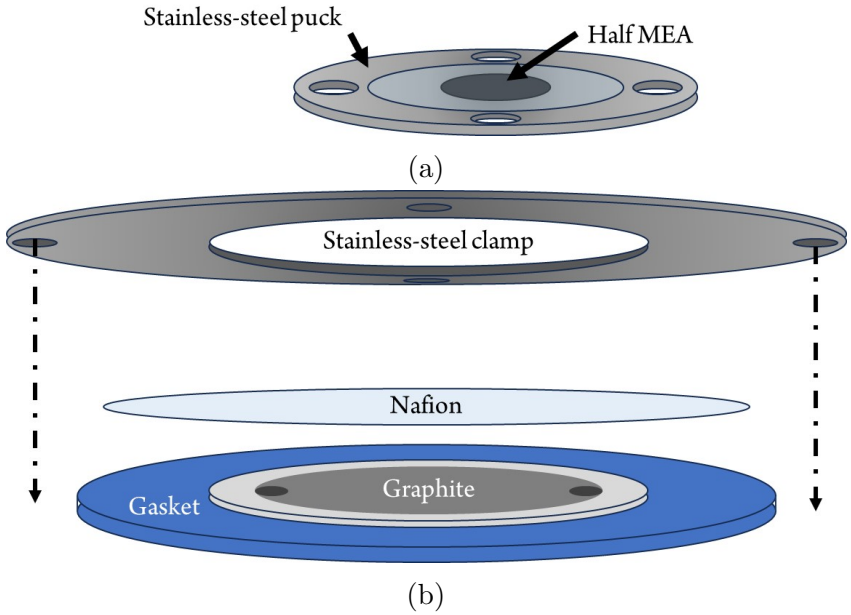

Figure 2.5: (a) Steel sample puck used with the configurations in Figure 2.4a (b) New sample holding approach, showing how a stainless-steel clamp sandwiches a sample of Nafion onto a gasket.

To this end, the cell was designed so that an IEM sample could be placed on the top of the graphite electrode so that the edges of the IEM could be sealed using a clamp which would press the sample down against a rubber gasket, as seen in Figure 2.5b. In a VOFC, the IEM is not fixed to the electrode, but instead must be near it with space for the electrolyte. This would effectively seal the sample edges to prevent any electrolyte from leaking while still allowing plenty of room for the AFM cantilever to approach and scan the sample surface.

In the spirit of simulating a VRFB and to increase the volume of electrolyte between the IEM and graphite, we planned to include a small circle of 1mm thick carbon felt

electrode (Figure 2.6). This would be placed on top of the graphite before a membrane sample would be clamped down to the cell. We assumed that the clamping force holding the membrane down would be sufficient to compress the electrode and make sufficient electrical contact with the graphite in the cell, simulating the natural state of electrodes in a VRFB albeit at a smaller scale.

As to how to introduce the electrolyte to the sample, we needed a way to flow elec-

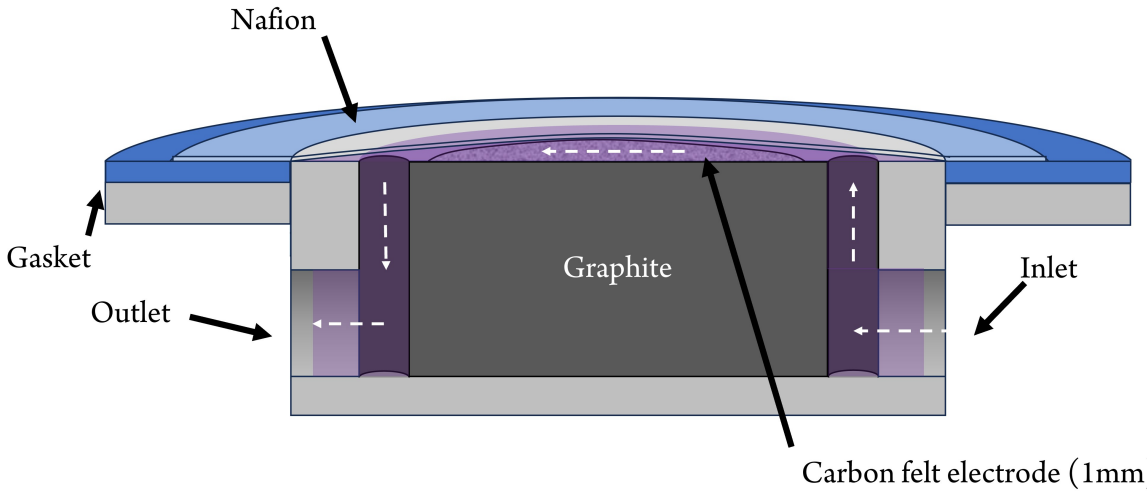

Figure 2.6: Block diagram showing the design of the internal plumbing of the imaging cell. Electrolyte is routed from the bottom of the graphite electrode, over the electrode, and back down to the outlet.

trolyte to the space between the sample and the graphite electrode without breaking the seal between the sample and the gasket. The electrolyte must not block access to the electrode for electrical connections. To this end we designed the cell such that the graphite electrode would have two channels cut along its length. To access these channels, threaded holes were included at the bottom of the cell which would connect to the bottom of the graphite channels. The holes and channels were placed on opposite sides.

Figure 2.6 depicts a cutaway view of the internal plumbing of the first iterations of the design, showing the pathway the electrolyte would take to flow between the sample and graphite while not breaking the seal. 1/16th inch NPT threaded hose barbs (see Figure 2.11)which would fit 1/16th inch ID tubing were chosen to interface with the cell.

To these hose barbs a length of 1/16th inch tubing would be attached and fed up to the surface of the AFM stage through gaps in the cell body. Thus, using Luer lock fittings, a pump could be used to push electrolyte into the cell through the tubing once an IEM sample was sealed onto the top.

Electrical Connections

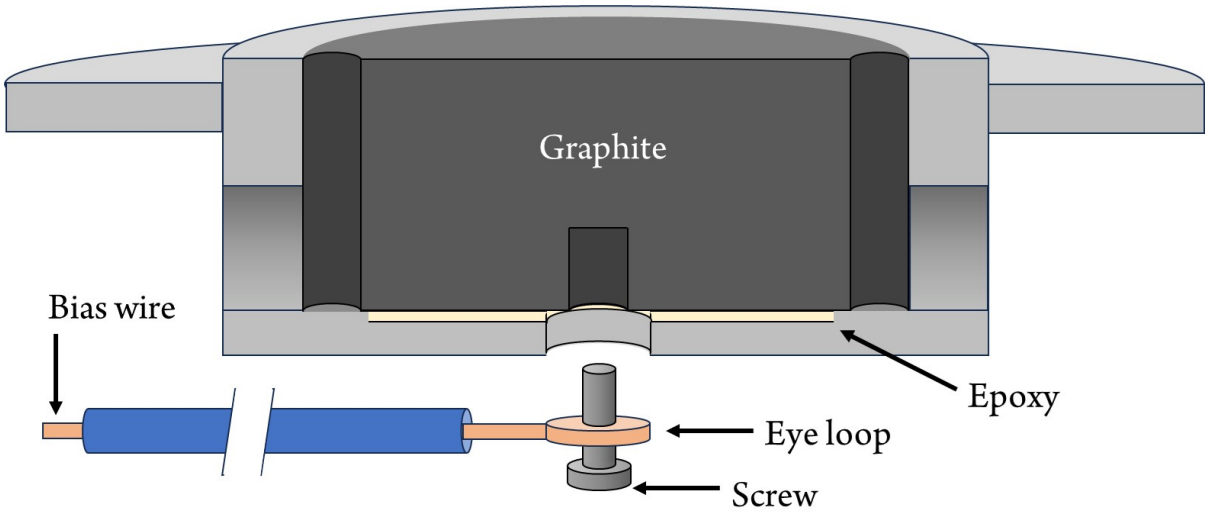

Figure 2.7: Block diagram showing how electrical contact is made from the graphite electrode to the bias wire using a screw.

In the original polyheater cell (see Figure 2.4), electrical contact to the half-MEA

electrode was made by attaching the looped end of a stripped wire to one of the screws used to fix the stainless-steel puck in place as seen in Figure 2.4. This wire terminated in a male 2.54mm pitch pin connector. The ORCA cantilever holder contains a screw terminal to attach a bias wire, as seen in Figure 2.8. To access the graphite electrode in the cell without affecting the gasket seal or the internal plumbing, we chose to drill a hole in the bottom of the cell and insert a screw into the graphite, with a copper eye loop around said screw connected to an insulated bias wire, as seen in Figure 2.7. To prevent electrolyte from leaking beneath the graphite into the electrical connection, we sealed the graphite in place with epoxy and drill the access hole after it was dry.

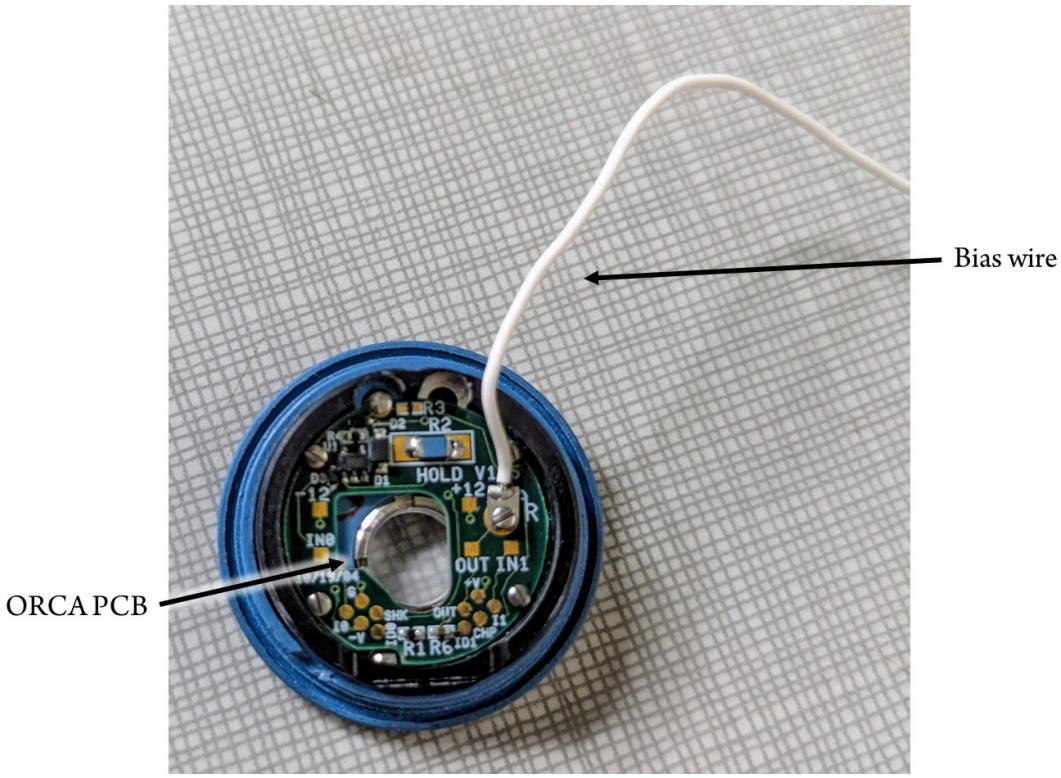

Figure 2.8: Picture of the AFM scan head, showing the ORCA current sensing printed circuit board (PCB), as well as the bias wire connection.

Once we had found what we deemed to be the best approaches to stay within the design constraints, we began to model the first iterations in Fusion 360. For the first CAD design, many of the outer dimensions were taken directly from the modified polyheater cell (Figure 2.4). For future reference in this document, the X and Y axes are in plane with the sample surface (and the imaging plane) and the Z axis perpendicular to the sample.

2.4 AFM Imaging Cell Prototype Fabrication

2.4.1 CNC Machining

The cell body CAD design was approached from the standpoint of needing to CNC machine the entire cell body out of a single piece of stock material. The design was not symmetric about the Z axis, so turning it on a lathe was not feasible. Once a suitable CAD model had been developed in Fusion 360, we used the in-software features to create the tool paths that would cut the design from a solid block of HDPE using a CNC. The impetus behind this was from a materials perspective- thermoplastics such as HDPE, polyether ether ketone (PEEK), and polypropylene (PP) had the desired material properties such as high corrosion resistance and machinability but could not be 3D printed as the resulting part would be naturally porous- thus the cell body would need to be made from a block of solid starting material.

Figure 2.9: Three of the early machining tests, staring from wood (left, center) to HDPE (right).

We went through several iterations of CAD models which were machined first out of wood to test out dimensions, then finally out of HDPE in the case of the first working prototype. Figure 2.9 depicts a few of the first attempts at machining these models. Using wood allowed us to dial in the settings of the CNC machine. The CNC we used was a Genmistu 3018 desktop model equipped with a 500W spindle at 10000 RPM. The machine was controlled via a GRBL controller, which uses G-code files to move the X, Y, and Z axes of the CNC during milling. We used the Universal G-code Sender, an open source GRBL-specific software on a PC connected to the controller via a USB cable to control the machine. The CNC controller included a set of alligator clips which would close a circuit when touching, allowing for finding the origin of the stock being machined. The prototypes that were machined out of wood and HDPE all began as a roughly 75x75x25mm block of material. The blocks were fastened to the CNC Y stage

with the provided fasteners and the origin set using a piece of conductive tape on the corner of the stock material connected to one of the alligator clips and the other connected to the milling bit. The prototypes were machined in stages, with the stock needing to be flipped over to machine both sides. The need to flip the stock over proved to be a large hurdle in the fabrication process, as it was very difficult to get the stock to exactly align with where it needed to be after flipping. This resulted in several failed attempts using wood which helped to refine the fabrication process.

2.4.2 The First Working Prototype

Figure 2.10 showcases the CAD model of the first working prototype design. It incorporates all the design features previously mentioned; clamped-down sample holding, internal plumbing, and screw electrical connection. By this point, we had gone through several different designs which had been machined out of wood.

Having learned the easiest way to fabricate the prototypes using the CNC machine, we machined the first working prototype out of a block of HDPE. Once the block had been machined into the cell body, a series of holes needed to be drilled. To clamp a sample down, holes for 1/16th inch bolts were drilled through the Z direction of the cell body. In the earlier prototypes four holes were used. A central hole was drilled to allow for a screw to make electrical contact with the graphite electrode. Holes were then drilled

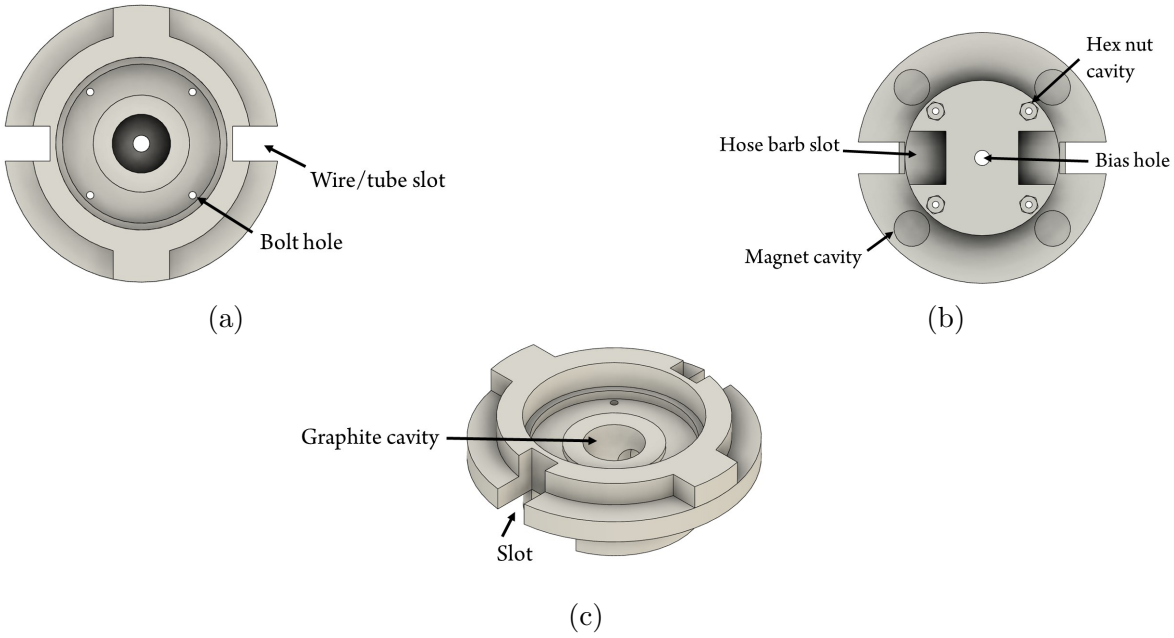

Figure 2.10: (a) Top-down view of the first prototype cell CAD model, showing the slots for tubing and the bias wire and the holes for clamp bolts. (b) Bottom-up view of the CAD model, showing magnet and hex nut cavities, as well as the slots for the threaded hose barbs. (c) Orthographic view of the CAD model, showing the central graphite cavity.

through the XY axis in the bottom section and then tapped using a 1/8th inch NPT tap. Two 1/16th inch hose barbs with 1/8th inch NPT threads were then screwed into the holes with Teflon thread tape. Small neodymium magnets were press-fit into holes that had been machined into the plastic to hold it in place on the AFM stage, as seen in Figure 2.10.

For the graphite electrode in the early machined prototypes, grooves were cut into two opposite sides of a graphite electrode rod using a Dremel tool before being cut to length. These grooves were aligned with the threaded hose barbs before the graphite was pressed into the central machined cavity (see Figure 2.10) and glued in place with epoxy.

The grooves connected the inlet hose barb to the outlet hose barb through the opening of the grooves at the graphite surface, forcing electrolyte up and over the electrode and under the sample, as seen in Figure 2.6. Electrical connection to the graphite was made through a pre-drilled hole at the bottom of the HDPE body using a length of insulated copper with one end wrapped around a 1/16th inch screw which was carefully screwed into the graphite. The wire terminated in a Molex pin connector.

Once the electrolyte plumbing was completed on the prototype, a clamp and gasket were needed to seal a sample. We engaged the services of an on-campus machine shop with a wire EDM machine to procure a 316 stainless steel clamp with a thickness of 0.5mm and with 4 holes for the fasteners. For a gasket, we cut a circle out of a sheet of 1mm thick tin-cured silicone using a utility knife. Figure 2.11 shows the first fully assembled HDPE prototype complete with clamp, gasket, hose barbs, and graphite electrode. 1/16th inch hex nuts were embedded into the cell body for the clamp bolts. Also pictured in Figure 2.11a is a cutaway diagram of the internal structure of the first working prototype, showing the electrical connection, internal plumbing, and sample clamping system.

2.4.3 External Fluid Pumping System

As mentioned previously, we wanted to simulate the fluid pumping seen in a full-scale VRFB cell for our system. Our first attempt to do this entailed setting up a fluid reservoir

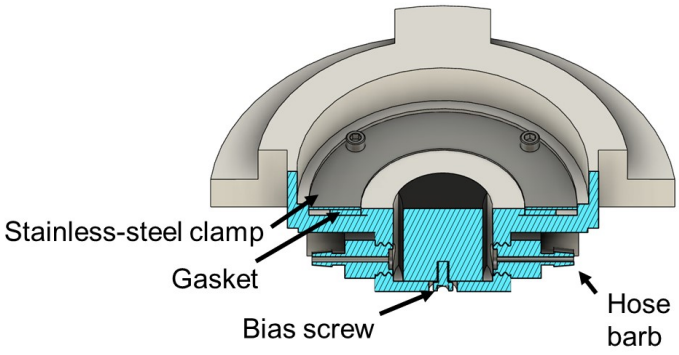

(a)

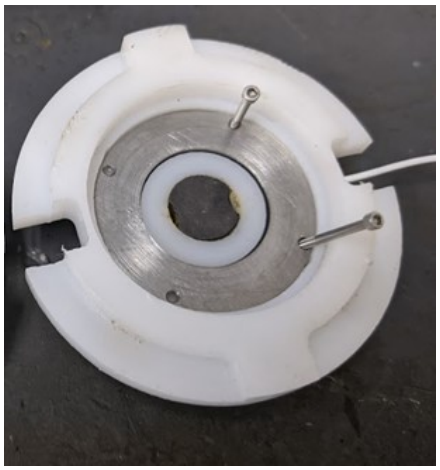

(b)

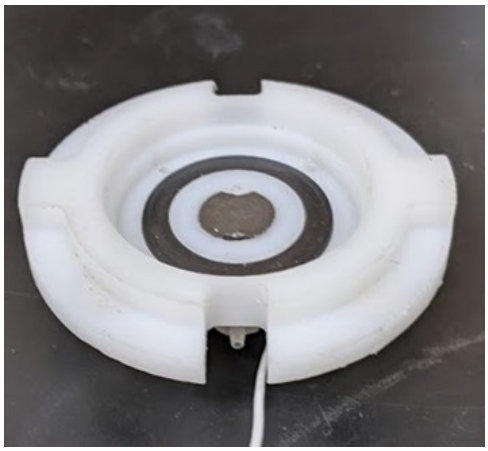

(c)

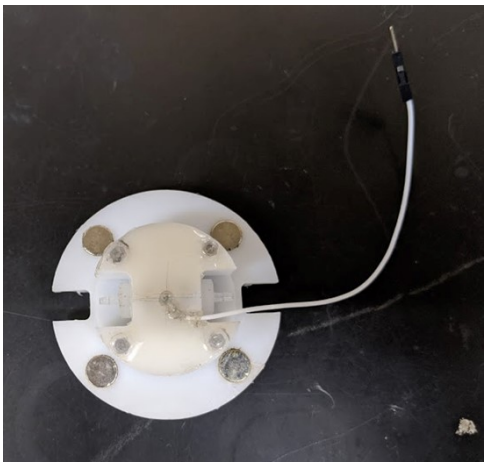

(d)

Figure 2.11: (a) Orthographic cutaway view of the first fully assembled imaging cell. (b) Top view picture of the assembled cell with stainless-steel clamp and bolts. (c) Side view of the cell showing the gasket, slots, and hose barb. (d) Bottom view of the cell, showing magnets, bias wire, and the embedded hex nuts.

which fed into the imaging cell via gravity, with the fluid which flowed out of the cell being collected into a separate reservoir. The upper reservoir was replenished via a MasterFlex peristaltic pump, as seen in the diagram in Figure 2.12. Due to space constraints and to prevent water ingress into any part of the AFM, the fluid delivery systems were located outside of the AFM vibration isolation chamber.

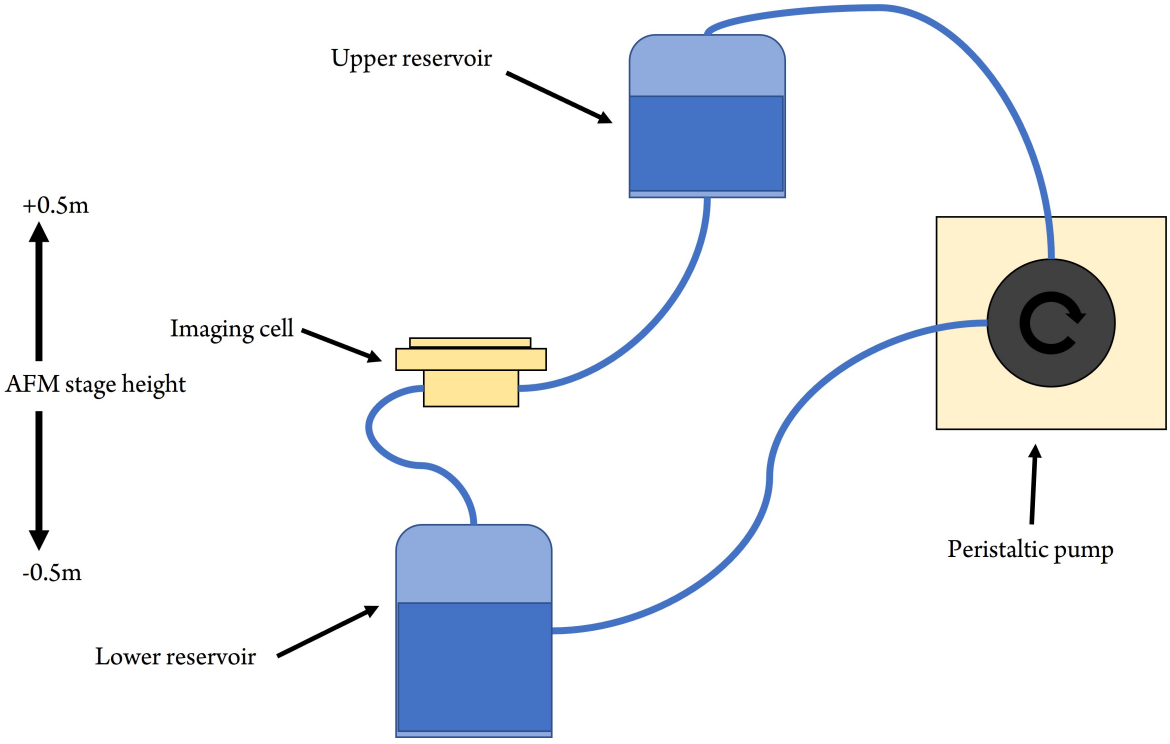

Figure 2.12: Diagram of the fluid movement system for the imaging cell, showing how fluid was gravity fed through the cell from an upper reservoir to a lower reservoir, with the upper being refilled via a peristaltic pump. The distance of each reserviour relative to the AFM stage was 0.5m.

To test this system, we filled the upper reservoir with DI water and clamped the outlet tube to prevent flow before the imaging cell was in place. A 25mm diameter circular sample of Nafion 212 from the Fuel Cell Store (Texas, USA) was cut and boiled in 5% per-

oxide, DI water, 1M sulfuric acid, and DI water again for 1 hour each. A 4mm diameter circle of 1mm thick carbon felt electrode was placed down before the Nafion sample was clamped to the imaging cell gasket using the stainless-steel clamp and 1/16th inch bolts. Once the tubing was connected to the imaging cell according to Figure 2.12, the assembled cell was placed in the AFM imaging stage and the scanning head was carefully lowered and positioned over the IEM sample. A Pt-coated cantilever (HQ:SC11, Mikromasch, USA) with a resonant frequency of 300 kHz and a spring constant of 42 N/m was used to image the sample. This cantilever type was used for all subsequent tapping mode images.

Figure 2.13 shows the first height images obtained of Nafion 212 using the first working prototype. No current data was collected as we were only interested in testing the fluid delivery system at this point. As seen in Figures 2.13a-2.13c, many imaging artifacts are present due to the pulses and vibrations generated by the movement of water through the cell, with the difference between them being the pumping rate. Figure 2.13d was taken with the entire fluid delivery system detached from the cell as a point of comparison.

There is a clear correlation between the size and shape of the artifacts and the pumping rate. On top of the large pulse artifacts there are higher frequency vibrational noise artifacts which we suspected came through the fluid hoses from the outside environment. Having had no success in eliminating the pulsing artifacts using the gravity-fed/peristaltic pumping system, we explored using a syringe pump to deliver fluid to the cell in a more

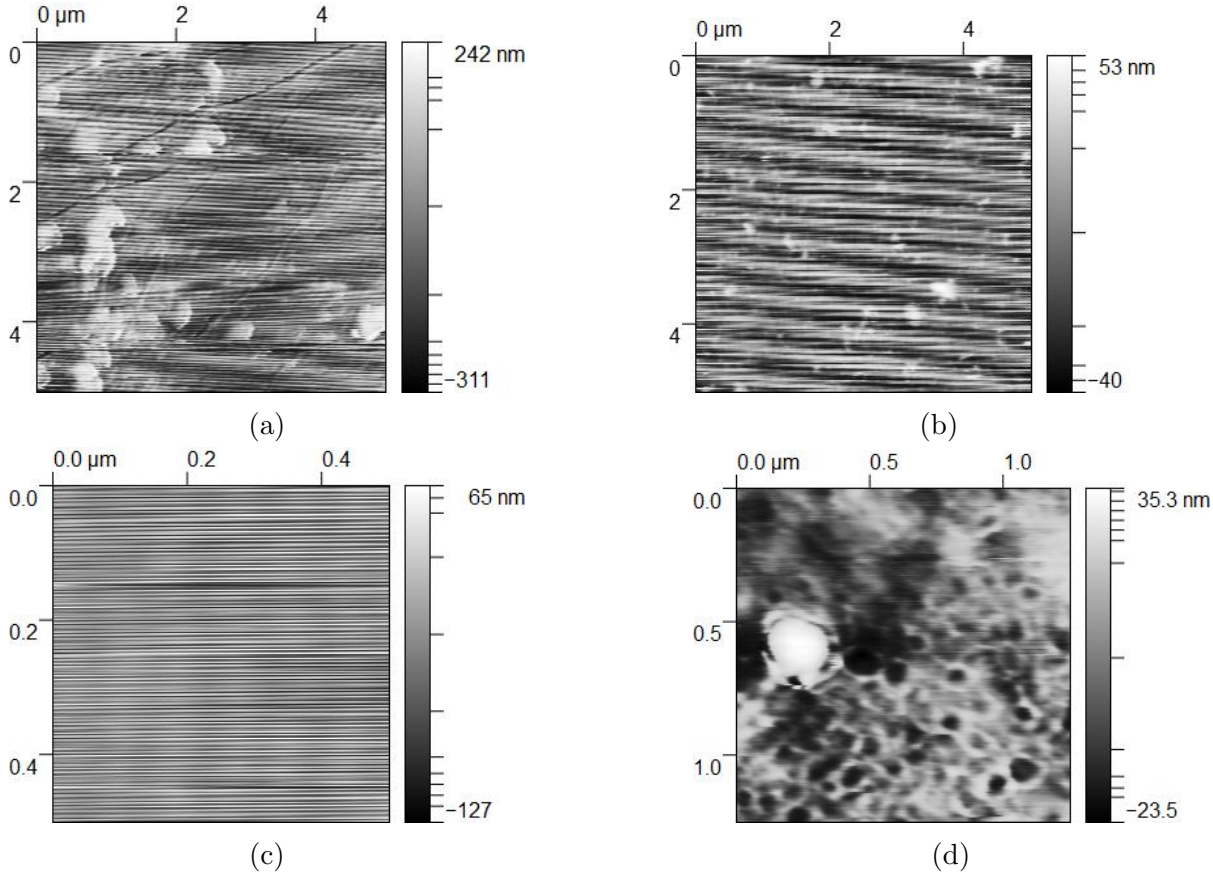

Figure 2.13: Height images of Nafion 212 acquired in tapping mode, with 0.1 mL min^{-1} (a), 0.5 mL min^{-1} (b), and 2 mL min^{-1} water pumping rates. (c) Height image obtained with the fluid movement system completely detached.

controlled and reproducible manner.

Custom-built Syringe Pump

As previously stated in the project constraints, we needed to stay within the budget for this project and thus purchasing a new syringe pump was not feasible at this point. Thus, using inexpensive components and 3D printed parts, we constructed a custom syringe pump which used a stepper motor coupled to a linear actuator to depress a syringe

plunger. We began by first designing the system in CAD using Fusion 360 modeling software, basing the measurements around an inexpensive stepper-motor-driven linear actuator that we purchased online (Befenybay, China). The parts we designed were then 3D printed out of polylactic acid (PLA) plastic filament using a Neptune 2 3D printer (Elegoo, China). The pump was assembled and fitted with a 5 mL syringe, as seen in Figure 2.14. The stepper motor was controlled via an A4988 driver connected to an Arduino Nano microcontroller (Adafruit, USA). A custom Windows application waswritten in C# using the community edition of Microsoft Visual Studio to interface with the microcontroller and control the fluid delivery to the imaging cell precisely and in real time. Figure 2.14b is a screenshot of the application running on a PC. The application allowed a user to control the position of the linear actuator, set a volume of fluid to be dispensed over a set period, or dispense a set volume of fluid at a set rate. The commands were sent via a serial interface with a baud rate of 9600 bytes per second.

The syringe pump was calibrated by dispensing water into a beaker on an analytical balance, weighing the water after each addition. These measurements produced a corrective calibration factor which allowed us to dispense fluid using the pump in a reproducible way Figure 2.15 depicts the data used to create the calibration factor.

To test the pump with the AFM, we followed the same procedures previously used to prepare a sample of Nafion 212 and loaded it onto the prototype imaging cell. A 5 mL syringe was filled with DI water and loaded on the stepper-driven pump. A Luer connec-

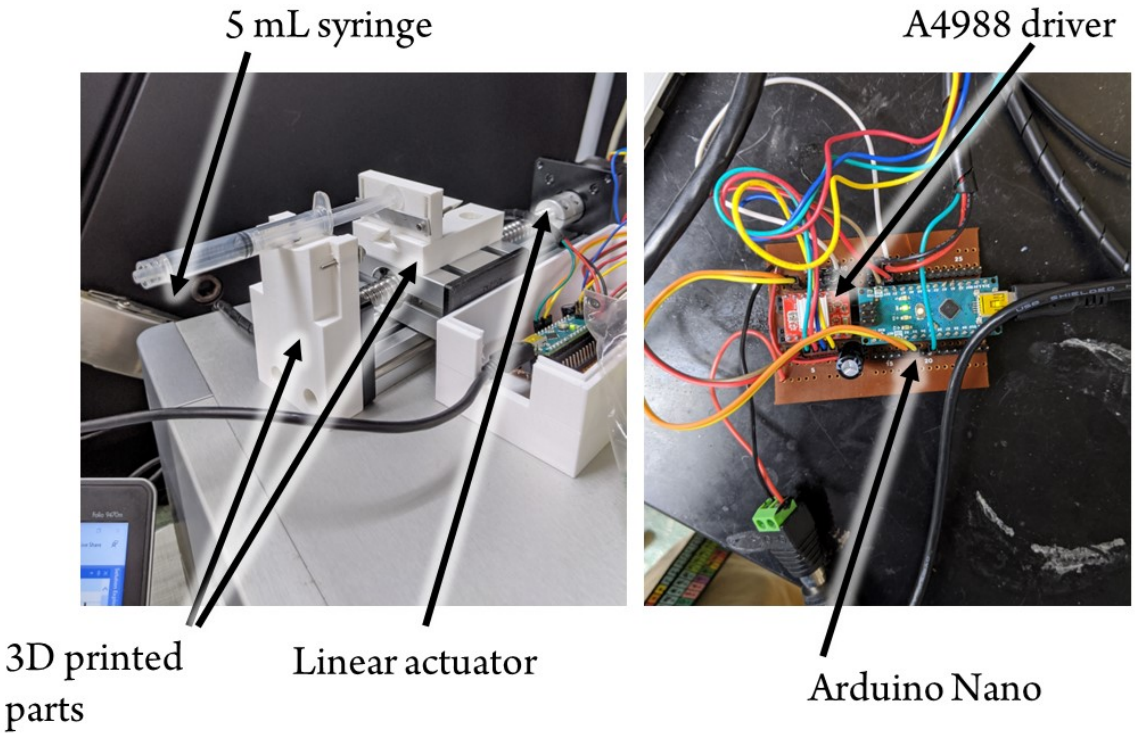

(a)

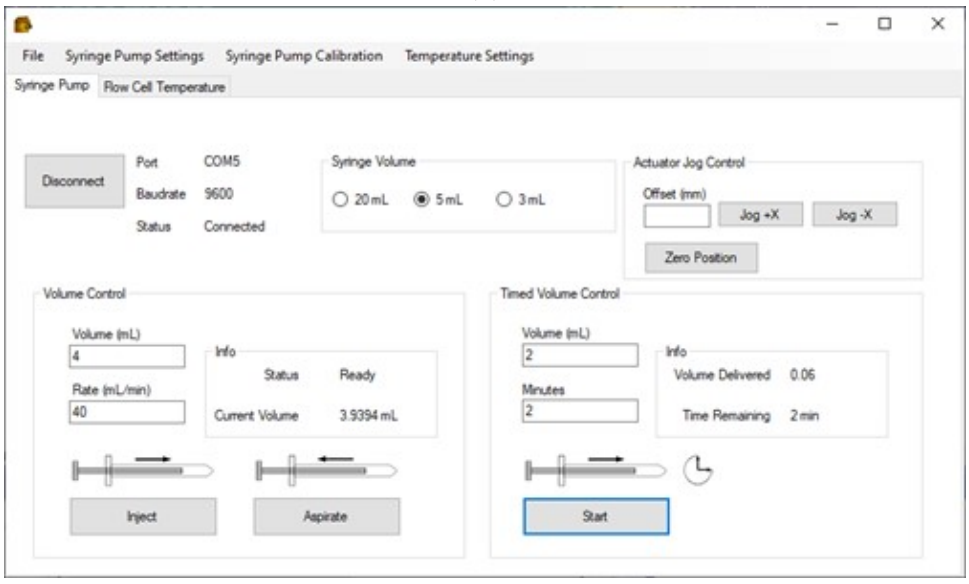

(b)

Figure 2.14: Picture of the custom syringe pump. (b) Picture of the syringe pump controller. (c) Screen capture of the custom syringe pump control program graphical user interface.

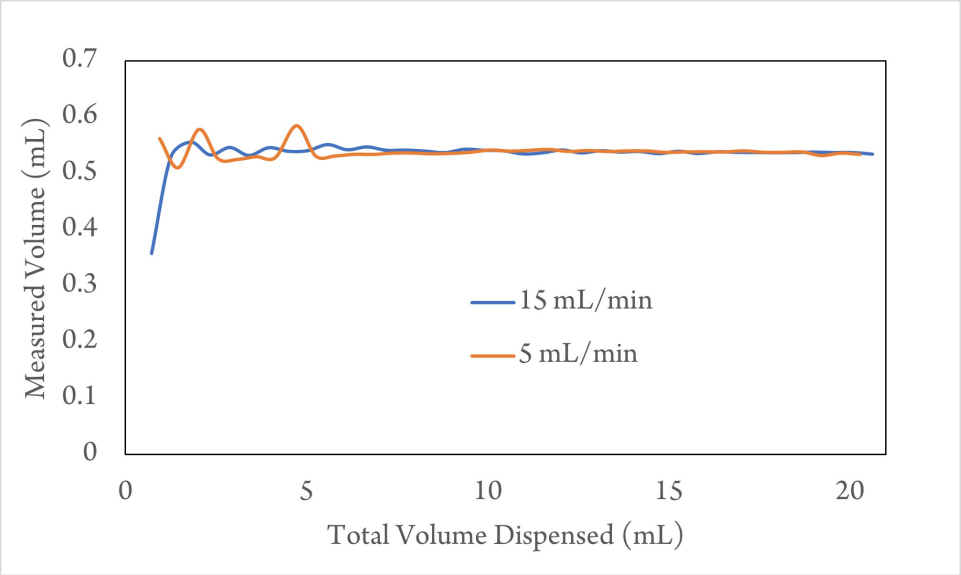

Figure 2.15: Syringe pump calibration data for two separate flow rates, 5 mL min^{-1} (orange) and 15 mL min^{-1} (blue), dispensing 0.5 mL 40 times consecutively into a weighed beaker and recording the weight of each addition.

tor was used to connect the syringe to the imaging cell with a length of 1/16th inch ID tubing. The same AFM settings and cantilever were used as with previous images taken using the peristaltic pumping system.

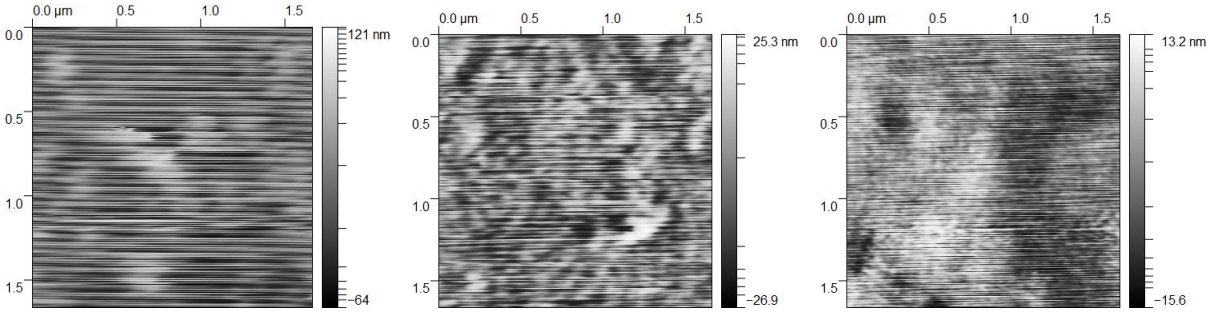

(a) (b) (c)

Figure 2.16: Height images of Nafion 212 taken with the syringe pump set to (a) 0.5 mL min^{-1}, (b) 0.1 mL min^{-1}, and (c) 0.05 mL min^{-1}.

Figure 2.16 shows the effect of pumping rate from the syringe pump on the imaging

artifacts seen in the AFM height images of Nafion 212. At higher rates, there are severe imaging artifacts due to the pressure waves generated from the syringe plunger movement. Decreasing the flow rate to a very slow 0.05 mL min^{-1} results in smaller artifacts spaced closer together. Figure 2.17 contains normalized profiles of each of the height images taken at different pumping rates, with the profiles taken perpendicular to the artifact lines. The periodicity of the artifacts is evident in the profiles, with lower speeds showing more of the vibrational artifacts and higher speeds showing pressure wave artifacts. At this point, we began to determine if an external electrolyte system is necessary to collect the data that would provide valuable insights into IEMs under VRFB conditions.

2.4.4 Key Takeaways from the First Prototypes

External Reservoirs and Pumps

From the perspective of a full-scale VRFB, the external tanks and pumps are necessary due to the low volumetric energy density of the electrolytes and the grid-scale sizes of typical VRFB installations. The pumps are needed to supply fresh, unreacted vanadium ions to the cell stacks of the installation during cycling, as the internal volume of a cell is much smaller than the volume needed to maintain the required current densities. For a typical VRFB cell, the maximum current density depends on the cell electrode area, the IEM proton conductivity, and the concentration of vanadium ions available[86]. Thus, electrolyte consumption is proportional to the electrode area of the cell.

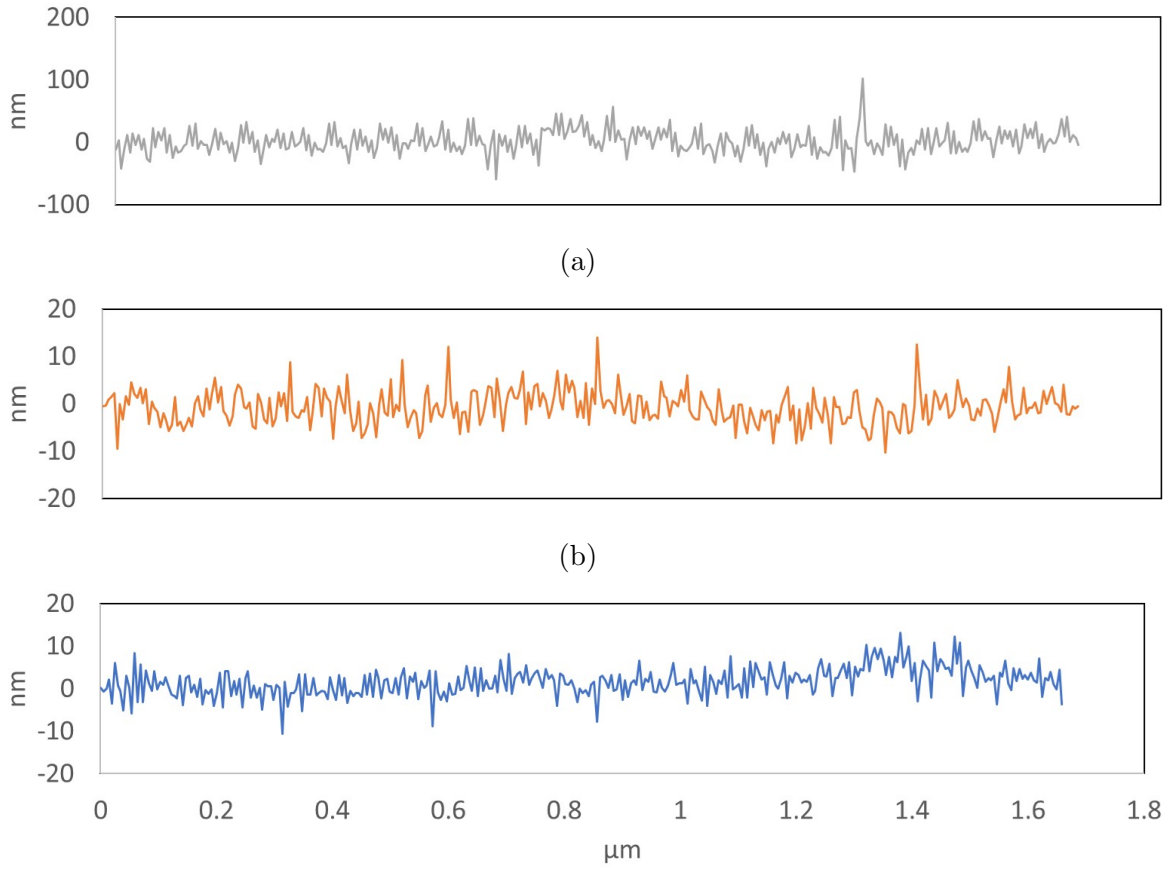

Figure 2.17: Profiles along taken along the center of the height images from top to bottom in Figure 2.16, with (a) corresponding to 0.5 mL min^{-1}, (b) to 0.1 mL min^{-1}, and (c) to 0.05 mL min^{-1} syringe pump flow rates, respectively.

To justify keeping the external electrolyte reservoirs and pumps to our system, the current density during data collection would need to be high enough so that the volume of electrolyte inside the imaging cell would be consumed to a degree that would have a deleterious effect on data collection due to concentration gradients forming. Conversely, no external electrolyte is needed if the volume of electrolyte inside the cell is large enough so that no concentration gradients emerge during cp-AFM data collection. The amount of current that can flow from the tip to the sample is metered through the ORCA current sensing circuitry such that the maximum current is set at 20 nanoamperes (nA) at any given time during data collection. The MFP 3D AFM rasters the cantilever tip over a surface line by line at a set rate. If the tip is scanning the surface at a rate of 1.5 µm s^{-1} with a tip radius of 30 nm, the tip covers a total area of:

$$1.5\mu m\ s^{-1} \times 30nm = 0.045\mu m^2\ s^{-1} \tag{2.1}$$

If, over one second, the faradaic current between the tip and the surface is at the maximum of 20 nA, then the moles of vanadium ions oxidized over 0.045 µm^2 would be:

$$20nA \times 1s = 20nC \tag{2.2}$$

$$\frac{20nC}{F} \times \frac{mol\ V}{mol\ e} = 2.07 \times 10^{-13} mol\ V \tag{2.3}$$

Where F is Faraday's constant. Thus, 2.07 x 10^{-13} mol of vanadium ions would be oxidized per second over an area of 0.045 µm^2. However, previous work using cp-AFM on IEMs where hydrogen was oxidized at a counter electrode and oxygen reduced to water at a Pt-coated cantilever resulted in a faradaic current range of 0-30 pA due to

overpotentials at each electrode and ohmic resistance, with resistance dominating[19]. Thus, assuming a V^{2+} concentration of 1.5M, a 1.5 x 1.5 µm area scanned over 512 seconds of raster time, and at 30 pA of constant current, the theoretical maximum volume of electrolyte needed per scan is:

$$30pA \times 512s = 15.36nC \tag{2.4}$$

$$\frac{15.36nC}{F} \times \frac{mol\ V}{mol\ e} = 1.59 \times 10^{-13} mol\ V \tag{2.5}$$

$$\frac{1.59 \times 10^{-13} mol\ V}{1.5M\ V} = 106.1fL \tag{2.6}$$

Thus, the volume between the membrane and the graphite needs to be at least 106 fL. Since the area scanned is a square, the distance between the membrane and the graphite is:

$$106.1fL = 106.1\mu m^3 \tag{2.7}$$

$$\frac{106.1\mu m^3}{1.5\mu m \times 1.5\mu m} = 47.2\mu m \tag{2.8}$$

Thus, the electrolyte volume would require a spacing of at least 47 µm between the IEM and the graphite electrode. If the 30 pA of current is an underestimation, it can be determined if the rate of vanadium ion diffusion is fast enough to negate the possibility of a concentration gradient forming during a scan. Using Fick's Second Law of Diffusion:

$$\frac{\delta c}{\delta t} = D_{\text{eff}} \frac{\delta^2 c}{\delta x^2} \tag{2.9}$$

Where x is the spatial dimension (m), t is the temporal dimension (seconds), D_{eff} is the effective ion diffusivity($m^2\ s^{-1}$), and c is the concentration (mol L^{-1}). D_{eff} can be calculated using:

$$D_{\text{eff}} = D_{\text{i}} \frac{\mu^0}{\mu} \tag{2.10}$$

Where D_{i} is the ion diffusivity (2.4 x10^{-10} m^2 s^{-1} for V^{2+} or V^{3+}), μ is the acid electrolyte viscosity (1 mPa s) and μ^0 is the viscosity of the V^{2+} electrolyte (3.2 mPa s). Due to the nanometer scale, the effective diffusivity is scaled to 7.68 x 10^8 nm^2 s^{-1}. Using numerical methods in Mathematica, the solution to the differential equation was found and plotted.

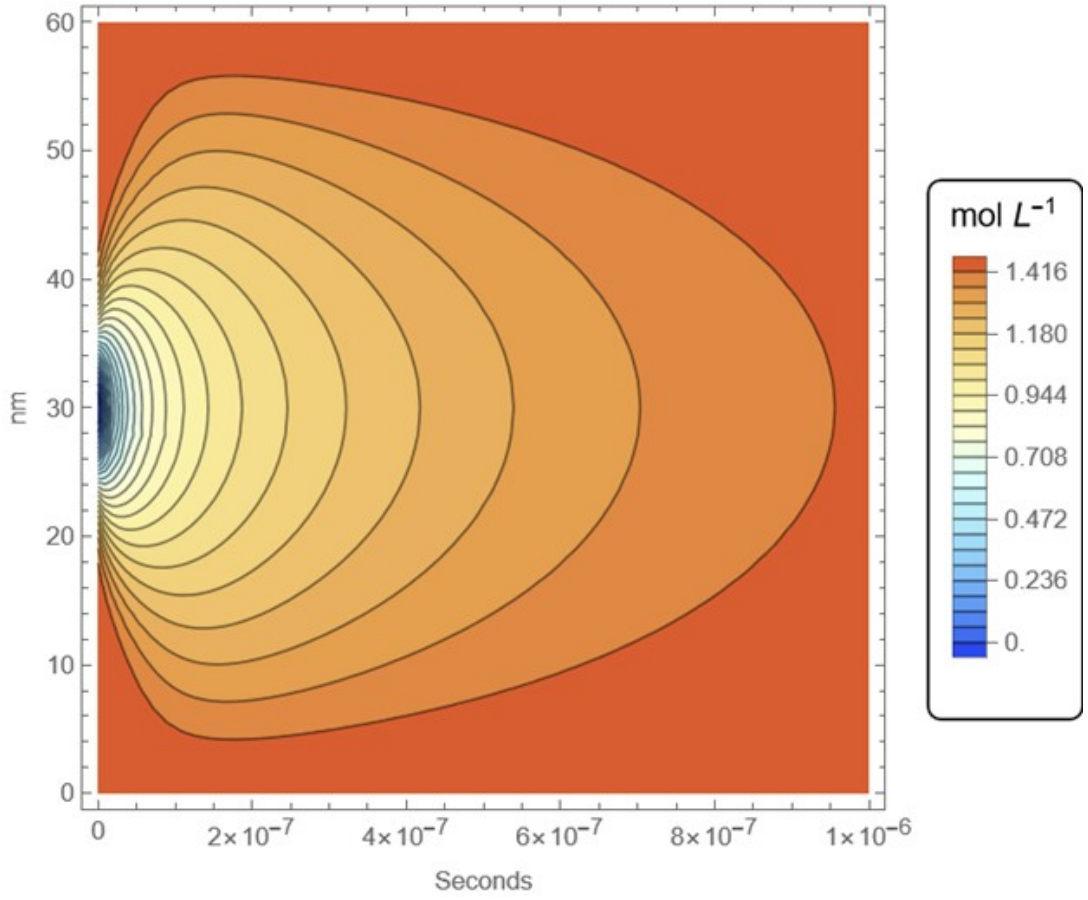

Figure 2.18: Contour plot showing the concentration of V^{2+} ions over a 1-dimensional area vs time. Blue indicates low ion concentration, and orange indicates high ion concentration.

Figure 2.18 displays a contour plot of the one-dimensional spatial concentration of V^{2+} vs time in solution from a starting point at t=0 where the concentration in the center of the position axis contains a normal distribution of low V^{2+} concentration due to localized oxidation from the cantilever tip passing overhead at $t = 0$. Previous models on mass transport in VRFBs have shown that the redox reactions and current density are kinetically controlled[29], and that concentration gradients tend to develop between the IEM and the electrode interface due to the higher electrical conductivity of the graphite compared to the ionic conductivity of the IEM and electrolyte[25], as shown in Figure 2.19. The partial differential equation (PDE) solution obtained for the kinetic diffusion of V^{2+} ions from high (1.5M) to low (0M) concentrations on the nm scale shows that it would take approximately 1 µs for a 20nm diameter low concentration region to equalize with the surrounding electrolyte.

Knowing the AFM scan rate (1.5 µm s^{-1}) and tip radius (25-30 nm) gives a dwell time[99] of:

$$\frac{30nm}{1.5\mu m\ s^{-1}} = 20ms \tag{2.11}$$

If the dwell time (20 ms)>>diffusion time (1 µs), no concentration gradients should form during scanning from a kinetic standpoint. Thus, having a thin 47 µm layer of V^{2+} electrolyte between the IEM and the counter electrode would be sufficient for our purposes.

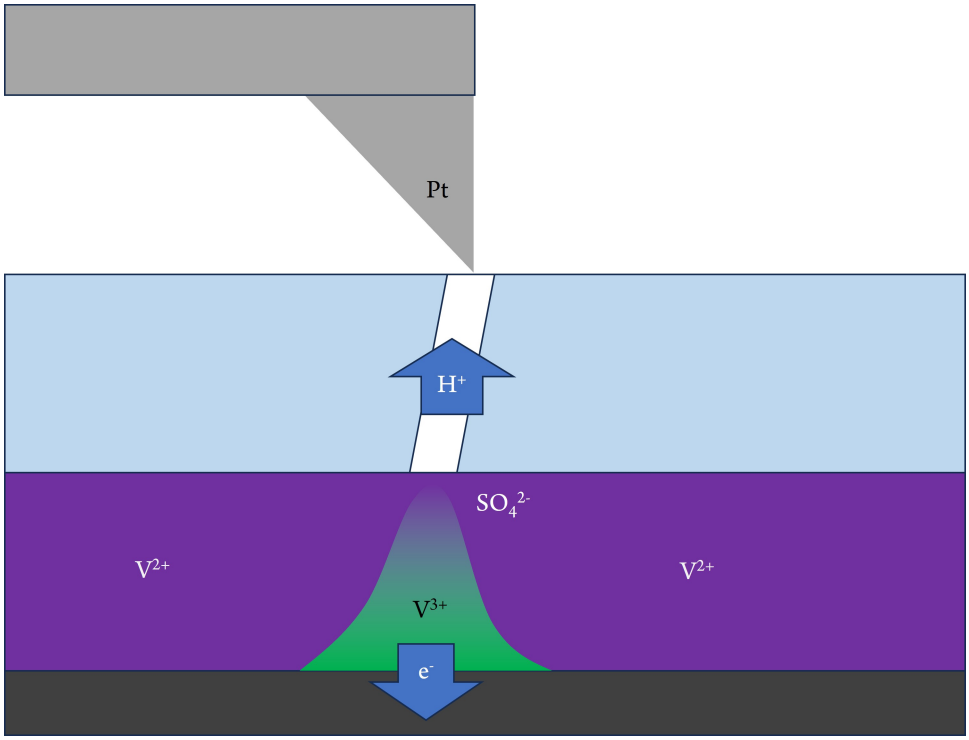

Figure 2.19: Diagram showing the localized oxidation of V^{2+} ions, with a gradient formed between the membrane and graphite due to the difference in resistance.

As seen from the height images acquired of Nafion using the early prototypes with external reservoirs and pumps (Figures 2.13 and 2.16), the small changes in pressure inside the cell from the fluid movement system causes the membrane sample to flex during imaging. These pressure waves introduce significant artifacts to the resulting images. This, combined with the analysis of the amount of electrolyte actually needed to collect useful data, lead us to conclude that the pumps and external reservoirs were not needed and should be removed from the system for all future designs.

Carbon Felt Electrodes

The next consideration was whether a carbon felt counter electrode was necessary. Here again we considered the purpose of the electrodes in a full VRFB stack: to provide a high surface area for charge transfer of vanadium ions during cycling, with the aim of increasing current density and coulombic efficiency. The same argument against needing external electrolyte reservoirs worked against the need for carbon felt electrodes- the 1 to 10 μm^2 area being imaged only needs to transfer $\sim$30 pC of charge per second, which can be facilitated by a simple conductive graphite surface situated beneath the IEM. Removing the carbon felt saves space and cost for the system and removes the variable of electrode contact resistance. We theorized that electrolyte will naturally diffuse between an IEM and a graphite surface through capillary action, as untreated solid graphite is not naturally hydrophobic, and the IEM is hydrophilic. Leaving a rough polish on a graphite electrode would allow for a few tens of micrometers of average space between it and the IEM- exactly what is needed.

To summarize, through trial and error we determined that the base system only needs to simulate a VRFB cell using an IEM, a conductive graphite surface, and enough electrolyte to wick between the graphite and the IEM. We also determined that no pumps, external reservoirs, or carbon felt electrodes are needed to accurately simulate the VRFB environment for an IEM at the nm scale we were working in.

2.5 Fully 3D Printed AFM Imaging Cell

While the first working prototype fulfilled many of the requirements for the completed system, it had several flaws. The time and resources that were required to produce it meant that iterating on the design was slow and costly, mostly due to needing to machine the cell body out of a single block of plastic. Not only did it need to be machined, but many steps were required from the machined part to a functional cell; holes needed to be drilled in precise locations, a length of graphite rod needed to be carefully machined on both sides, threads needed to be cut into drilled holes, and epoxy used to seal critical areas. After several uses the HDPE prototype began to crack at the bottom, which if not fixed would allow liquid to leak from the cell during data collection. We attempted to seal the cracks with epoxy but due to the hydrophobic nature of HDPE the epoxy would eventually fall off. Furthermore, the threaded 1/16th inch hose barbs were prone to breaking due to their small size. A new approach was needed to design and fabricate the next iteration of the imaging cell which considered the need for as few connections as possible and as few assembly steps as possible.

We explored the use of photo-sensitive 3D printed thermoset resin as an alternative to machined thermoplastic to fabricate the cell body. The main reason we had not explored this route yet was not knowing if a 3D printed resin could withstand the VRFB electrolyte. The first step taken was to 3D print a 1x1x1 cm cube of TR250LV high temperature resin (Phrozen, Taiwan) using a Mars 2 Pro mono-stereolithographic ap-

paratus (MSLA) (Elegoo, China) and place it in a beaker containing 1.4M $VOSO_4$ and 2.5M H_2SO_4 (See Appendix A) for 24 hours. We measured the dimensions of the cube with calipers before and after soaking. No change in the size of the cube was measured after soaking, and the surface of the cube appeared unchanged. From this result, we began to design a new cell which could take advantage of the unique capabilities of mono stereolithographic (MSLA) 3D printing.

2.5.1 MSLA 3D Printed Design

MSLA offers several advantages over CNC machining including:

- **Internal voids.** MSLA parts can contain voids and internal structure that would be impossible to make using subtractive CNC manufacturing.
- **High resolution.** Compared to the inexpensive desktop CNC machine which had a resolution of 0.2mm, a typical MSLA printer has a resolution of 0.05mm.
- **Rapid fabrication.** MSLA can produce a complicated part in a matter of hours which might take much longer to machine due to needing tool changes and stock flips.

Having verified the corrosion resistance of the photo-sensitive resin previously, we completely redesigned the imaging cell to take advantage of the unique advantages offered by MSLA 3D printing. The most significant change was the addition of internal plumbing

to the cell body. Instead of drilling holes in sides of the bottom of the cell which would connect to the machined grooves in a graphite rod, we opted to have 3D printed hose barbs extend from the top of the cell to internal tubes which connected to the center of the cell, as seen in the cutaway view of the redesigned CAD model in Figure 2.20. In place of having electrolyte being stored in a carbon felt electrode between the graphite and IEM, we opted to have a central cavity which surrounds a smaller inner cavity where electrolyte could fill once a membrane sample was clamped down.

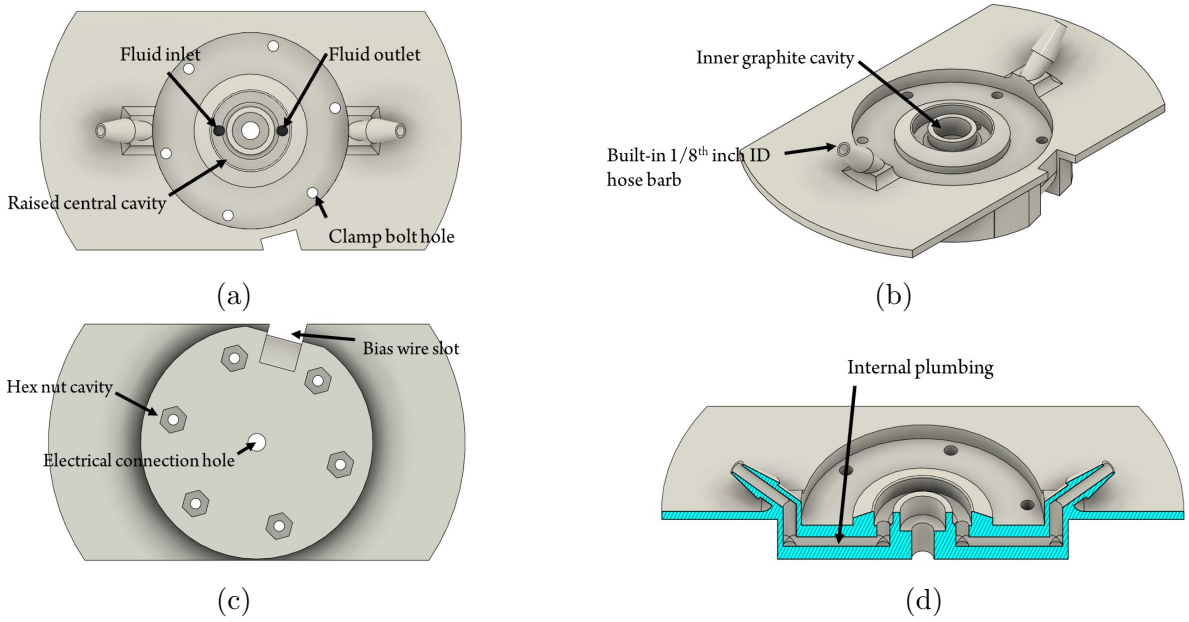

Figure 2.20: (a) Top-down view of the MSLA CAD model. (b) Orthographic view of (a). (c) Bottom-up view of (a). (d) Cut-away view of the internal plumbing of (a).

The redesign includes six clamping screws instead of four. We opted to 3D print the clamp for the new design, as it would allow for greater flexibility and feature addition, and it would save on costs of machining a new stainless-steel clamp. We changed the graphite

electrode diameter from 10mm to 6mm as this size is very inexpensive and easy to cut with a Dremel tool. We raised and sloped the central cavity walls with respect to the clamping gasket to slightly increase the tympanic tension of a membrane sample which would ensure good electrical contact between it and the graphite. The outer "wings" of the cell serve to sit flush with the top of the AFM stage and form a surface to place strong magnets on, keeping it firmly in place during imaging. The hose barbs are angled 45 degrees away from the center to ensure that any tubing attached to the cell would not interfere with the AFM during scanning. We kept the same system to seal the samples in place; a silicone gasket surrounding the central cavity which membrane samples are clamped down onto.

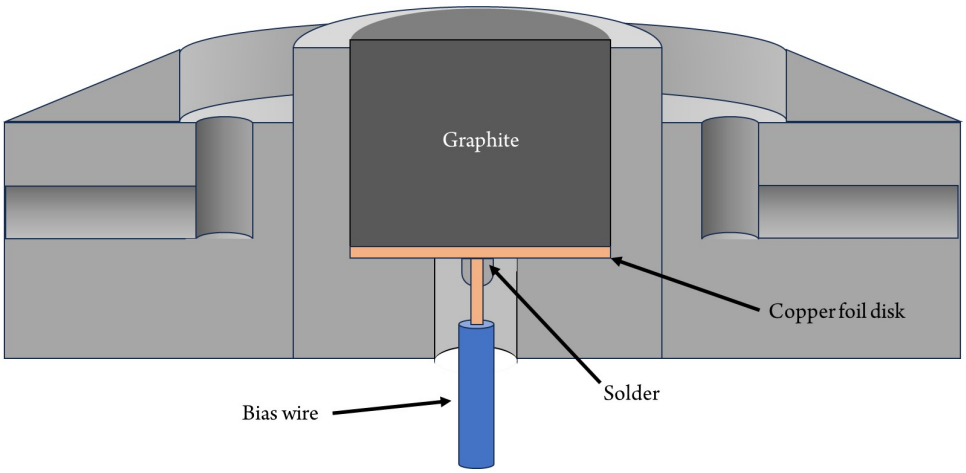

Figure 2.21: Diagram showing the electrical connection between the graphite and bias wire, accomplished using a thin copper disk.

Previously, to attach the bias wire a screw would be inserted directly into the graphite(see Figure 2.11)- but this approach had drawbacks; the graphite could crack during instal-

lation or afterwards from external forces, it was difficult to make sure that any wire wrapped around the screw stayed in place when handling the cell, and the screw would often work loose from the hole during normal use. For the new cell, we opted to have a wire soldered directly to a small circle of thin copper foil which could be punched out of a length of copper foil tape. This wire/copper assembly would be fed through the cell before the graphite was press-fit into place (see Figure 2.21), with the copper coming to rest at the bottom of the inner central cavity. Thus, when the graphite electrode was press-fit into the cavity, it would be in electrical contact with the copper foil. This setup avoids needing to drill directly into the graphite which simplified assembly and reduced contact resistance.

For the clamp, we designed it with small hose barbs incorporated into the outer edges for gas addition to the sample. Figure 2.22 shows the fully assembled cell CAD model complete with clamp, electrode, and gasket. Once the design was finalized, we 3D printed the cell body out of the TR250LV high temperature resin and began to assemble the cell. A 4mm length of 6mm diameter graphite electrode rod was cut using a Dremel tool. A 6mm diameter punch was used to punch a disk of copper from a small length of copper foil. A length of insulated 24-gauge copper wire was stripped at both ends, with one end terminating in a 2.54mm pitch male pin connector and the other was soldered to the copper disk using silver solder. This assembly was fed through the top of the cell body until the copper disk was sitting flush with the bottom of the graphite cavity, after which

the cut graphite electrode was wrapped in a layer of PTFE thread tape and press-fit inside the cell. The continuity between the top of the graphite and the wire connector was confirmed using a multimeter.

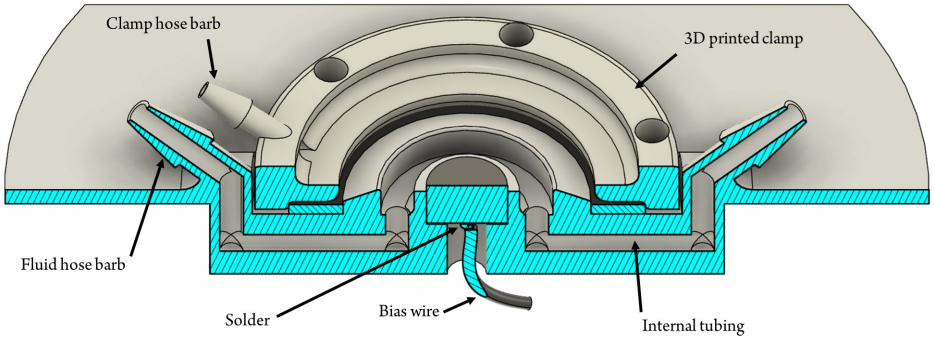

Figure 2.22: Diagram showing the fully assembled CAD model of the MSLA cell, including the internal plumbing, electrical connections, and clamp.

A new silicone gasket was cut from a 1mm thick silicone sheet and placed on the cell. Six 1/16th inch hex nuts were press-fit into the bottom of the cell body. With the clamp 3D printed out of the same resin and 1/16th inch 80-20 threaded stainless-steel bolts, the cell was fully assembled. The entire fabrication and assembly process took less than 6 hours, including the 3D printing time. The cost of the newly designed cell was much less than the original designs, needing only resin, a 6mm diameter graphite rod, copper foil tape, silicone sheet, and small fasteners. Figure 2.23 depicts the fully assembled imaging cell with a Nafion sample loaded on the AFM imaging stage, along with a gas tube connected to the 3D printed clamp. The cell in this figure has been filled with DI water for testing, with the fluid tubes securely attached to the printed hose barbs. This configuration was used to collect the first test images, minus the gas tubing connected

to the clamp.

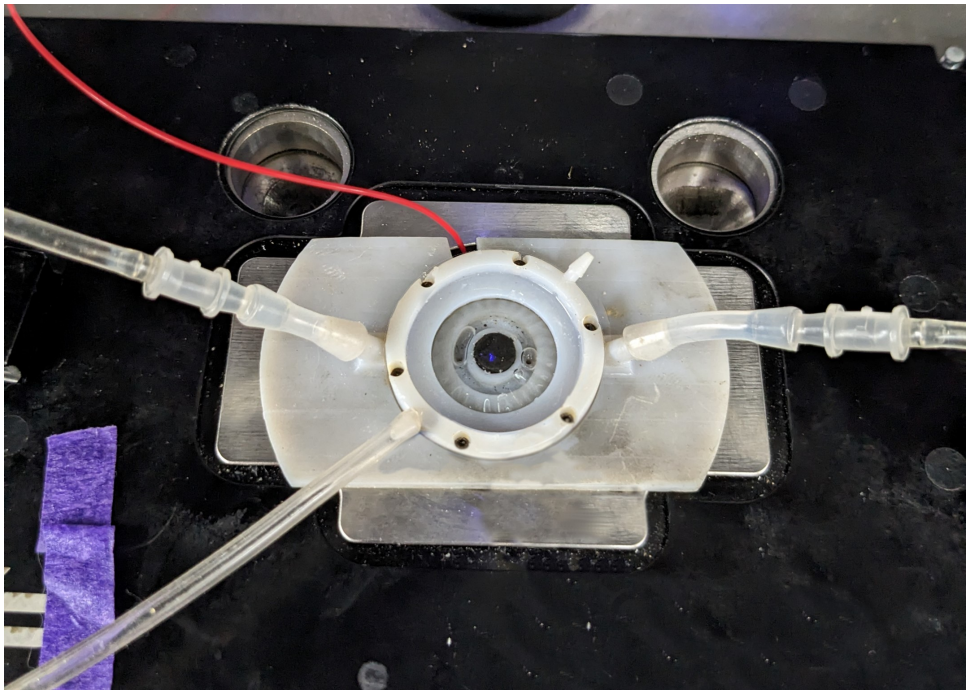

Figure 2.23: Photograph of the fully assembled MSLA-printed cell in the AFM, complete with Nafion sample, tubing, and bias wire.

Figure 2.24 depicts the first AFM attractive regime tapping mode height and phase images acquired of Nafion 212 using the redesigned imaging cell, with the cell cavity filled with DI water. The same settings and cantilevers were used as in the previous test images. No vibrational artifacts are present, which helped to validate the removal of the external pumps and reservoirs of the previous prototypes.

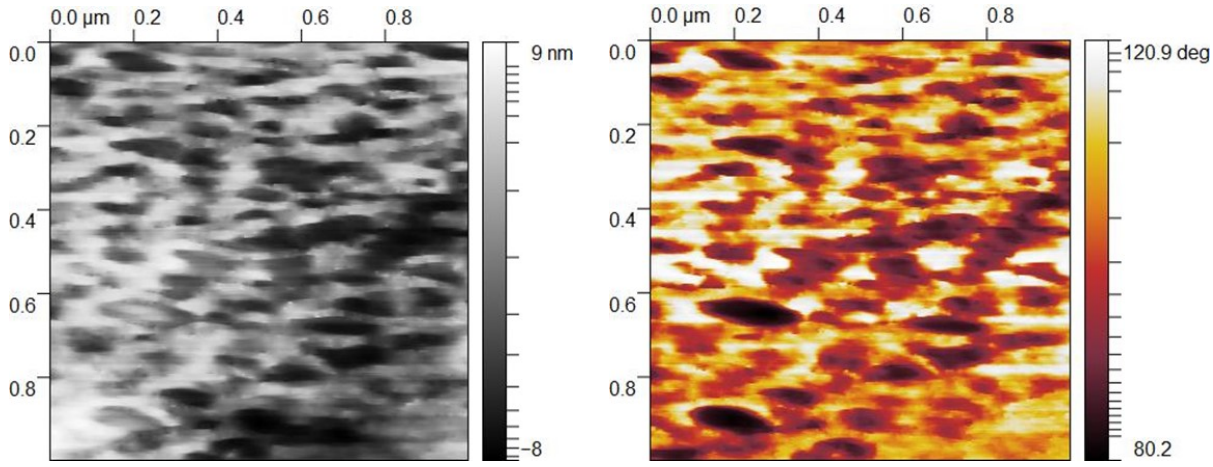

(a) (b)

Figure 2.24: 1x1 µm attractive tapping mode (a) height and (b) phase images of Nafion 212 taken using the newly design MSLA-printed cell. The cell cavity was filled with DI water.

2.5.2 Measuring Nafion Proton Conductivity Using the 3D Printed Cell

To collect valuable data on the proton conductivity of IEMs under electrochemical device operating conditions, we needed to validate the cell's ability to conduct electrons from the graphite anode, through the AFM current sensor, and finally to the Pt-coated tip where those electrons could combine with oxygen and protons conducting through the IEM to form water. Our first test consisted of imaging Nafion 212 with the cell filled with DI water in contact mode. We used a Pt-coated SiN cantilever with a spring constant of 0.2 N m^{-1} (Mikromasch, USA). As seen in Figure 2.25, this showed very little proton conductivity, ranging only a few pA over the entire surface, which was to be expected using only water and no electro-active redox species or bias voltage.

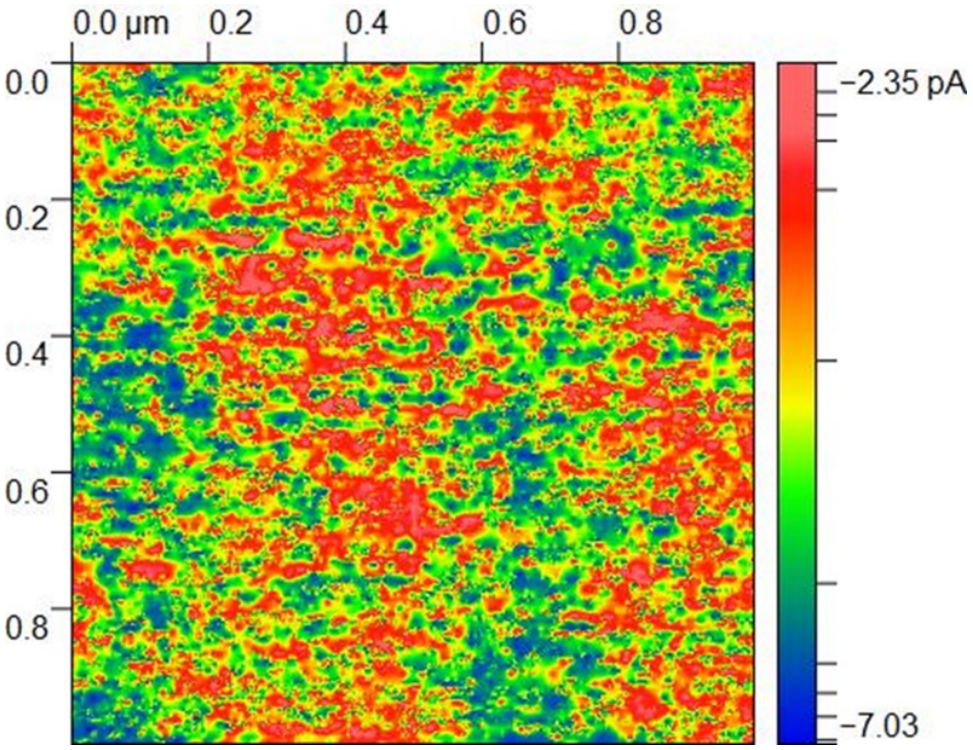

Figure 2.25: 1x1 µm contact mode current image of Nafion 212 taken using the MSLA-printed cell and with only DI water inside the cell.

From this first test there was a clear distinction between high and low conducting areas on the surface. Using Gwyddion, a scanning microscopy image processing software package, grain analysis was performed on the data from Figure 2.25, with the grain boundary threshold determined by Otsu's method[76]. The specifics of this method are discussed in Chapter 3. The software was used to extract the equivalent disc radius of each grain boundary, with the results plotted in Figure 2.26. This chart shows that most ionic domains have an equivalent disc radius below 10 nm. This would correspond to ionic domains averaging 20-30nm in diameter, which agrees with previous findings of Nafion under hydrated conditions using conductive AFM[35], where the resolution is limited by the cantilever tip radius (∼25nm).

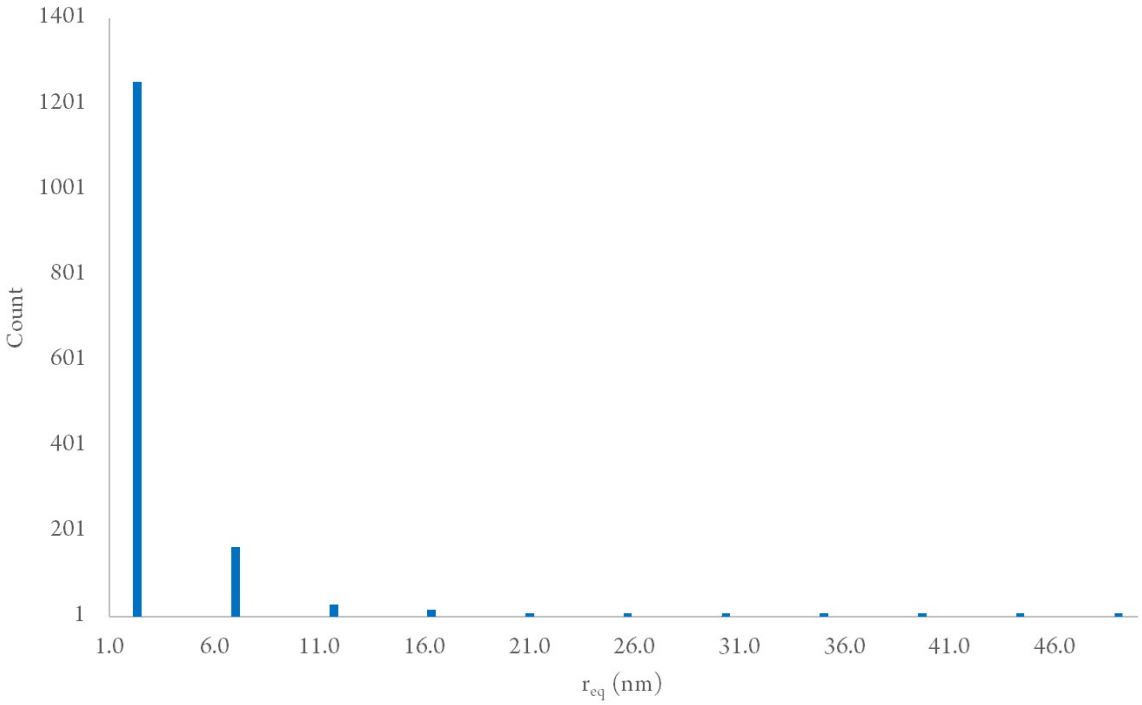

Figure 2.26: Plot of grain equivalent circle radius vs total grain count per grain equivalent radius for the AFM image in Figure 2.25.

Since there was no electrochemical or bias potential to drive faradaic proton conduction through the membrane, the current observed in Figure 2.25 is most likely due to capacitance[50] between the tip and the water-filled anionic domains. To validate the cell as a tool to measure faradaic proton conductivity driven by an electrochemical potential, we performed contact-mode AFM imaging of the same sample in Figure 2.25, but with the cell filled with 1.4M V^{2+} in 2.5M H_2SO_4 electrolyte in place of DI water.

Figure 2.27 depicts the current map obtained using this configuration, which shows an order of magnitude higher current range (1.5-2 nA). While this configuration clearly

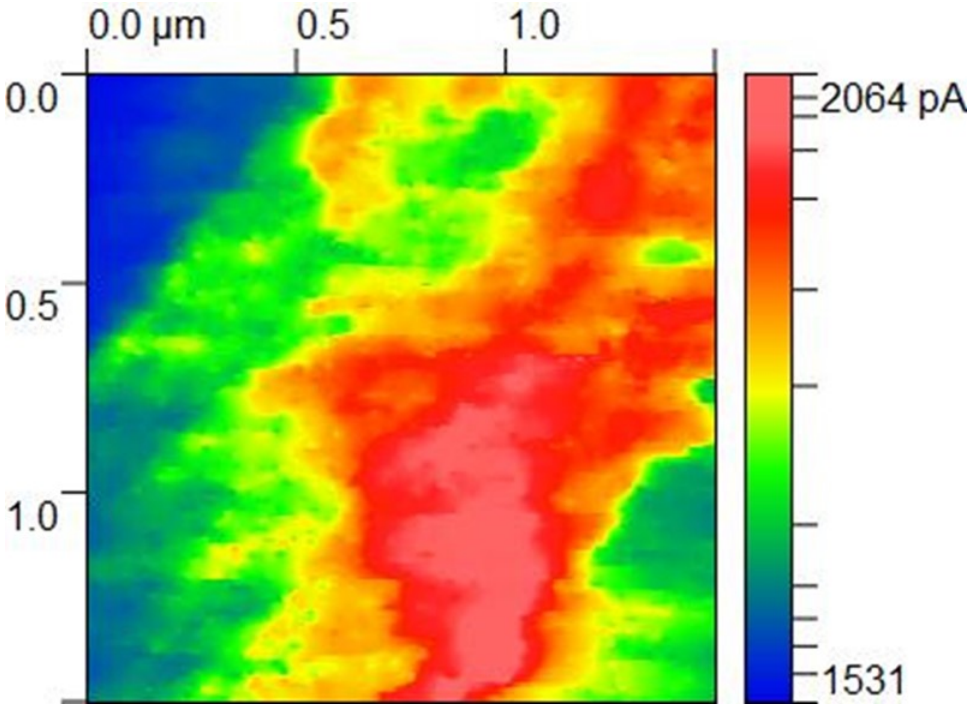

Figure 2.27: 1.5x1.5 µm contact mode current image of Nafion 212 taken with V^{2+} electrolyte inside the cell and with 0V bias applied.

demonstrates faradaic current as compared to purely capacitive current in Figure 2.25, the magnitude of the current appears to smear out the individual domains that were seen in the former DI water data. To counter this, the cell was reset with fresh electrolyte and imaged again in contact mode, with the addition of -700 mV bias applied to the sample. Figure 2.28 shows the result of this adjustment, with the ionic domains clearly visible on the surface, albeit larger than in the case of having DI water inside the cell.

Figure 2.29 contains a chart of the equivalent radius of the individual grains for Figures 2.25 and 2.28, with both having grain boundary thresholds determined using Otsu's method. This shows that for the image obtained with DI water, the grains are

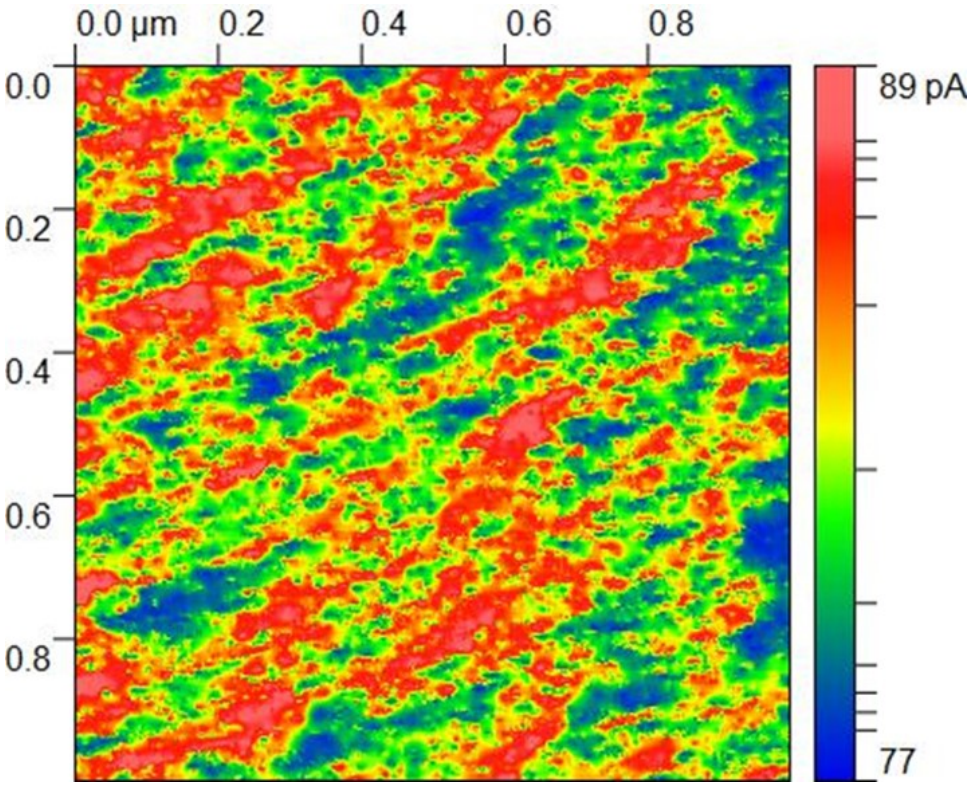

Figure 2.28: 1x1 µm contact mode current image of Nafion 212 taken with V^{2+} electrolyte inside the cell and with a -700 mV sample bias applied.

both smaller on average and are more numerous, compared to the image obtained with vanadium electrolyte with a negative bias, where the grain sizes are larger and are fewer in number. This appears to be less related to actual individual ionic domain size and more to the relatively high number of conducting sites on the surface which are unresolved due to having similar proton conductivity. This hypothesis is supported by Figure 2.27, which shows high conductivity over a large area with no voltage bias applied, which implies that large areas are conducting and become unresolvable due to tiny differences between individual domains.

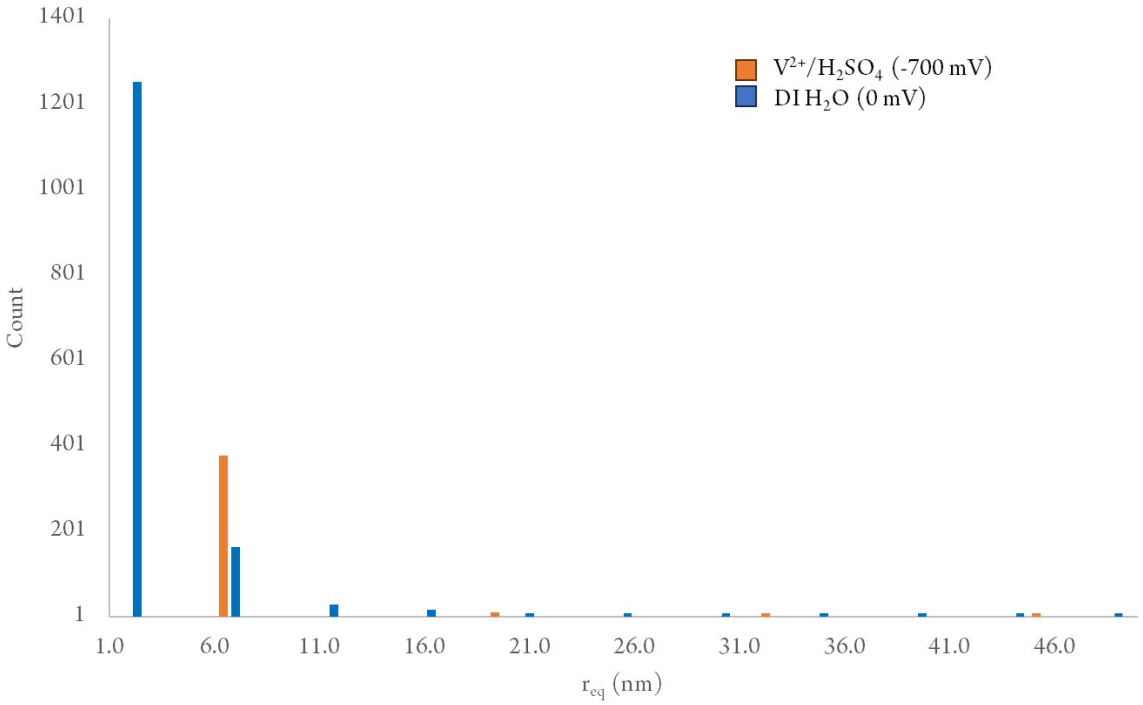

Figure 2.29: Overlaid plots of grain equivalent circle radius vs total grain count per grain equivalent radius for the AFM images in Figures 2.25 (Blue) and 2.28 (Orange).

Thus, we were able to validate the imaging cell's capability to resolve the faradaic proton conductivity of Nafion, driven by the oxidation of V^{2+} ions at the graphite electrode inside the cell. The nanoampere currents seen in contact mode with the cell filled with vanadium electrolyte show that there are few sources of ohmic losses in the system, compared to previous investigations using the modified polyheater cell, where current was restricted to the picoampere range due to ohmic losses[19].

Electrolyte Diffusion through Membrane Samples

Two issues that became apparent while collecting data were: first, that after about 30 minutes, there were visible droplets of vanadium electrolyte that had diffused through the

Nafion membrane to the surface as seen in Figure 2.30, and second, that the electrolyte inside the cell would change color from violet to green after the same amount of time while exposed air.

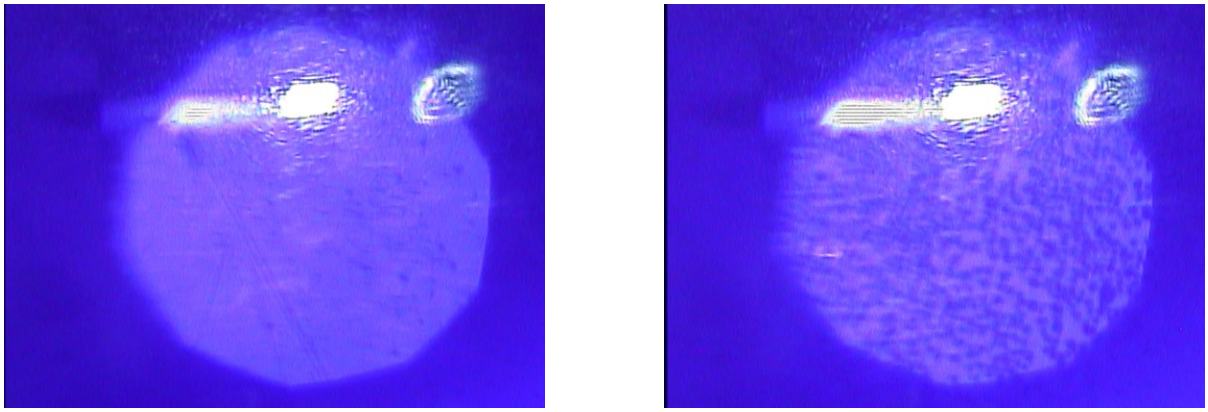

(a) (b)

Figure 2.30: Screenshots of the microscope objective inside the AFM used to align the laser with the cantilever, taken with the filled with V^{2+} electrolyte at (a) 0 minutes after loading the sample and (b) at 30 minutes after loading the sample.

Both issues are caused by ions diffusing through the membrane, with the droplets being due to osmotic pressure pulling electrolyte through the membrane to the surface where there is less water[113], while the color change was due to oxygen diffusing through the membrane from the air[87]. While these issues could affect AFM data collection, they occur over time and are slow enough such that at least one image can be obtained before either issue becomes a problem. Thus, in between separate images, we opted to wipe the Nafion with a Kimwipe^{TM} to remove the droplets and simply replace the electrolyte inside the cell. While the droplets could affect the tip-sample power dissipation while imaging in tapping mode, they would not compete for electrons from the cantilever tip,

as any V^{2+} or V^{3+} ions on the surface will react with atmospheric oxygen:

$$4VSO_4 + 2H_2SO_4 + O_2 \rightarrow V_2(SO_4)_3 + 2H_2O \ (V^{2+} \rightarrow V^{3+}, +1.49V) \tag{2.12}$$

$$2V_2(SO_4)_3 + O_2 + 2H_2O \rightarrow 4VOSO_4 + 2H_2SO_4 \ (V^{3+} \rightarrow V^{4+}, +0.89V) \tag{2.13}$$

$$2VSO_4 + O_2 \rightarrow 2VOSO_4 \ (\text{Total}) \tag{2.14}$$

The total reaction is spontaneous and involves only oxygen and vanadium, with no net increase or decrease in water or proton availability. Thus, while the surface oxidation of diffused V^{2+} ions might compete with the ORR at the cantilever tip for oxygen, no electrons should transfer between the tip and any V^{2+} or V^{3+} ions on the surface. The droplets would still be good proton conductors and would thus not limit surface conductivity.

2.6 AFM Imaging Cell Temperature Control

IEM temperature and relative humidity are important metrics in HFC operation as combined they determine the degree of swelling of the membrane[114][16], the water management of the triple-phase boundaries at each electrode[13], and the ion conducting channel size distribution[35]. There has been little need to investigate the effects of temperature or relative humidity on IEMs in the context of VRFBs as the narrow temperature solubility window of the dissolved VO_2^+ constrains their operation to room temperature[100].

VOFC cells have a wider temperature operating window since they do not rely on VO_2^+, and thus could benefit from temperature-dependent IEM conductivity studies. Ex-situ measurements of IEMs for VRFBs must take into account relative humidity, with most opting to make measurements at 100% relative humidity[123], which can approximate the fully hydrated conditions an IEM will be under while in contact with dilute sulfuric acid electrolytes. It was apparent at this point in the development that this imaging cell could be used not just for flow battery IEM research but for any electrochemical device which employs and IEM, including small organic molecule fuel cells (SOMFCs), hydrogen fuel cells (HFCs), metal-air batteries, and electrolyzers. Many of these devices are highly sensitive to IEM relative humidity and temperature[94][114], thus, to allow for investigations into IEMs under a wide range of electrochemical device simulations, we opted to add in cell temperature control and a way to monitor relative humidity of a gas flowing to the cell.

To accomplish this, the cell that had been designed for MSLA 3D printing was re-designed to incorporate a heating element and temperature sensor. A 4mm diameter ceramic heating cartridge was chosen as the heating element (Ultimaker BV, Netherlands) and a 100KΩ NTC thermistor (Creality, Shenzhen, China) was chosen as the temperature sensor. As depicted in Figure 2.31, two holes in the cell CAD model were hollowed out in Fusion 360 to provide space for both the heating element and thermistor. The newly designed cell was 3D printed out of the same resin used previously and using

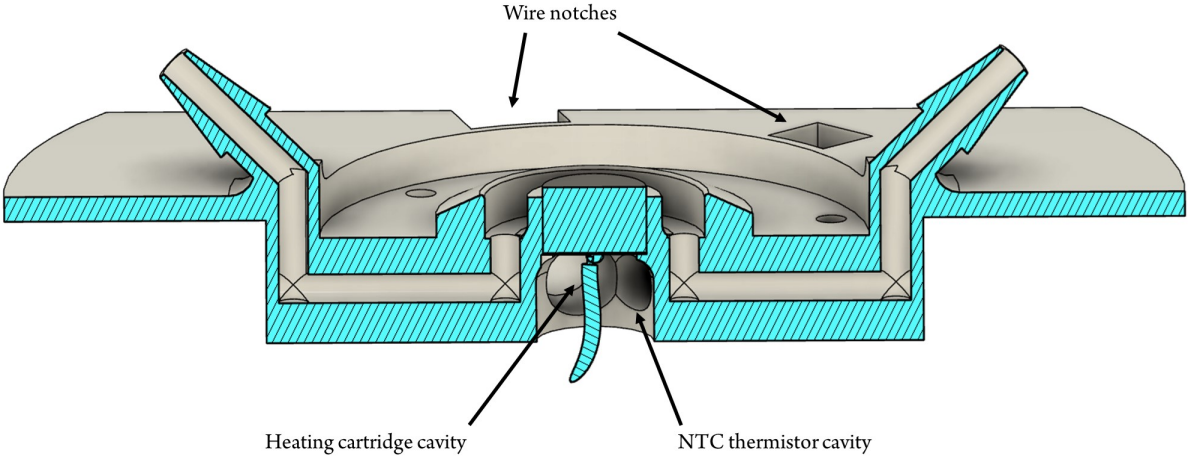

Figure 2.31: Cutaway view of the internal structure of the redesigned MSLA imaging cell, showing the internal cavities added to house the heating element and temperature sensor.

the same settings. The cell assembly was identical to the original MSLA-printed cell with the heating element and thermistor being inserted into the newly designed cavities as an additional step. The temperature controlling hardware wires (heating element and thermistor) were fed through notches in the printed cell and terminated in 2.54mm pitch pin connectors. Figure 2.32 depicts the completed cell with temperature control wires and connectors.

To control and monitor the temperature of the cell in real time, an Arduino Uno microcontroller (Adafruit, USA) was chosen along with a 20W DC power supply to power the heating element. Figure 2.33 depicts the circuit diagram of the temperature control hardware. An NPN MOSFET was chosen to control the current flowing through the heating element using an analog signal ranging from 0-255 from the microcontroller to the MOSFET gate.

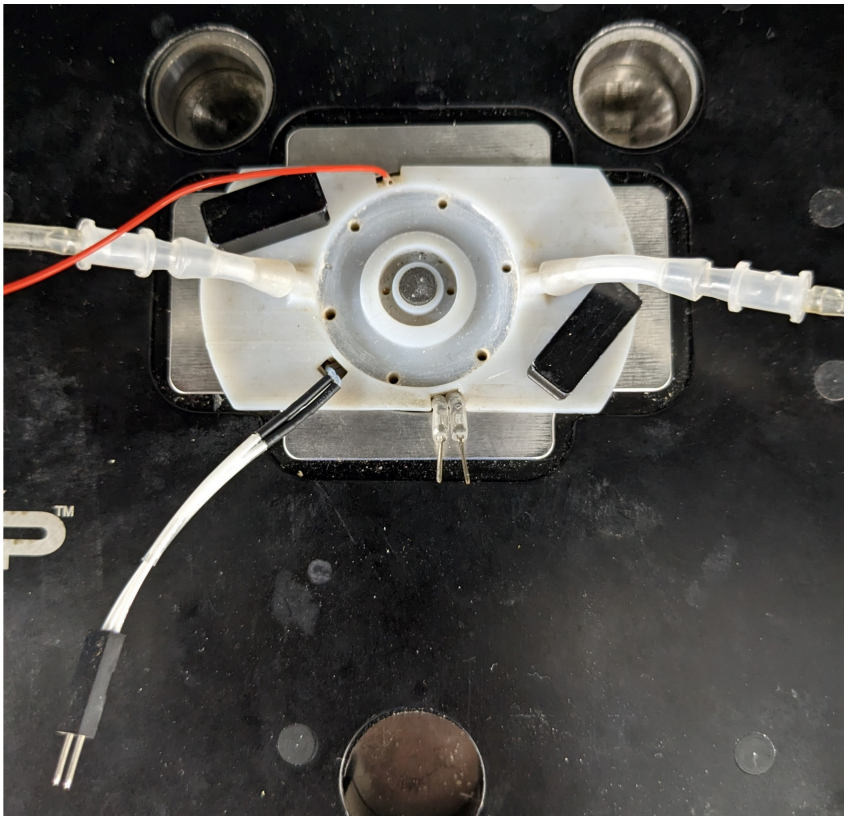

Figure 2.32: Photograph of the fully assembled MSLA-printed cell with temperature control inside the AFM stage.

In the first iteration of the temperature control scheme, firmware was written for the microcontroller which would follow a simple "on/off" temperature control; every second the temperature would be measured using the thermistor and if it fell below a set point temperature, the analog signal to the MOSFET would be set high to turn on the resistive heating element. At the first measurement cycle when the temperature was above the set point, the heating element would be turned off. This system was tested outside of the AFM, and it was found to produce a highly oscillating temperature profile, with the temperature of the cell overshooting the set point by several degrees Celsius before

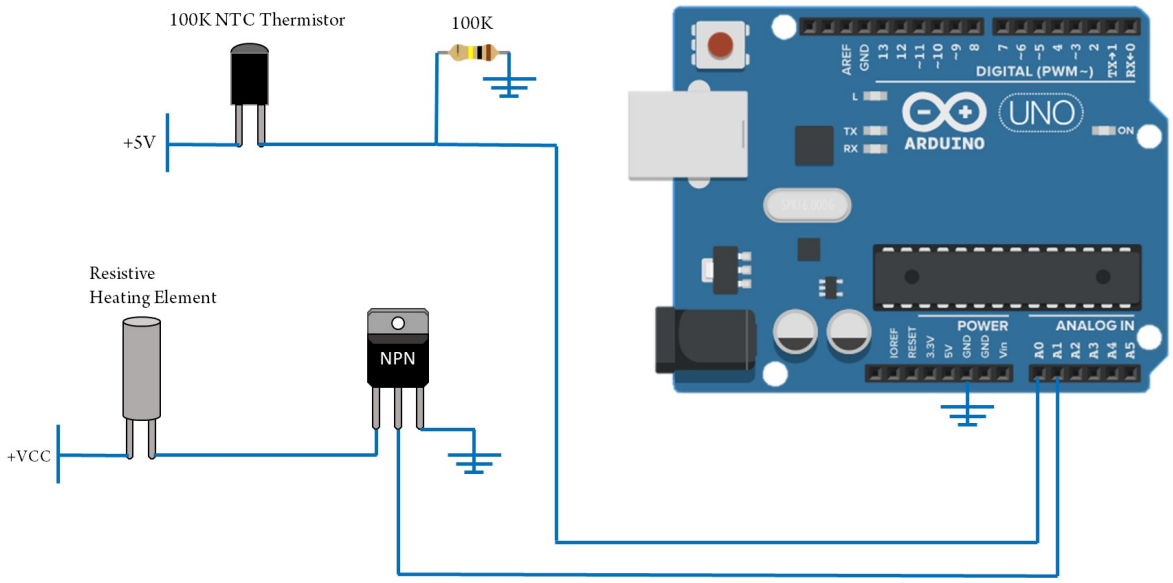

Figure 2.33: Electronic schematic of the cell temperature control system.

dropping below several degrees of the set point every few seconds. To mitigate this, a PID (Proportional Integral Derivative) control algorithm was implemented in the microcontroller firmware.

Briefly, PID algorithms take a set point and a measurement as input variables and return an output which can, if properly tuned, reduce the difference between the set point and measurement over time. The three components: proportional, integral, and derivative gains, define algorithmic operations that determine the magnitude of the output. Tuning these parameters can be accomplished by following the Ziegler-Nichols method[126], where the proportional gain term is increased until the temperature begins oscillating, at which point the magnitude of the proportional term and the period of the oscillation are used to set the magnitudes of the other two terms. Following the

Ziegler-Nichols method, the PID algorithm in the Arduino firmware was tuned until the cell could maintain a temperature to within $\pm$ 1 °C (see Figure 2.39).

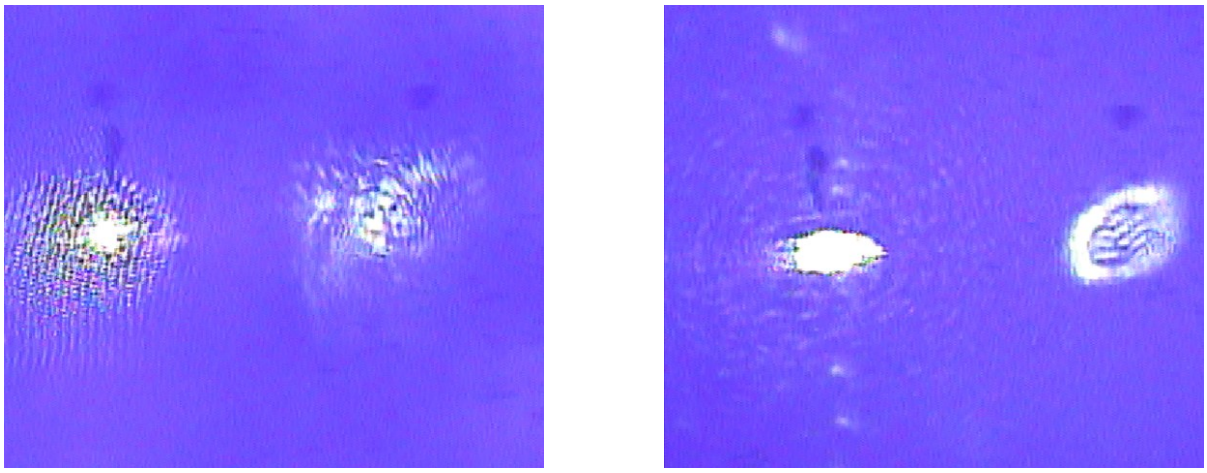

(a) (b)

Figure 2.34: Screenshots from the AFM optical microscope objective used for laser alignment showing the cantilever above the heated imaging cell loaded with Nafion (a) before adding air flow and (b) after adding air flow to the optics. In (a), the outgassed water vapor has collected on the cantilever and optics, causing distortions.

To test the imaging capability of the cell while at an elevated temperature, a sample of Nafion 212 was loaded onto the cell and the cell was filled with DI water. For comparison, a height image was first acquired with the heating element turned off (see Figure 2.35a). The images were acquired in tapping mode using the same cantilevers and settings as previous cell imaging validation tests. Cell temperature was monitored on a PC using a USB universal asynchronous receiver/transmitter (UART) interface with the Arduino microcontroller. The firmware of the microcontroller was updated with a setpoint at 40 °C to initiate the test. Once the cell temperature was consistently $\pm$ 1 °C of the setpoint, the cantilever was lowered onto the Nafion sample to begin data acquisition.

An immediate issue became apparent before data could be collected: water vapor began to condense on both the cantilever and the optics of the AFM. After turning off the heating element, the water evaporated over the course of several minutes while the cell cooled to room temperature. Benziger et al measured a water vapor flux of 10-2 g min^{-1} through Nafion at 30 °C when one side is exposed to liquid water[13], which is more than enough to coat the cantilever and optics within seconds. To combat this, air was routed to the AFM stage from a 30 L compressed air cylinder fitted with a regulator. A mechanical flow meter was used to control the air flow rate and compression fittings were used to reduce the tubing diameter to 1/16th inches so that it could be attached to the 3D printed hose barb on the cell clamp. It was found that above 5 cc min^{-1} flow rate the condensation on the cantilever would rapidly evaporate and the reflected laser would come back into focus inside the AFM. Figure 2.34 depicts the camera view of the AFM cantilever with and without air flow when near the heated sample. To monitor the actual relative humidity of the air flowing to the cell, a DHT22 sensor was installed inline between the flow meter and the imaging cell. The sensor was connected to the Arduino microcontroller used to maintain the cell temperature, and new firmware was written so that the readings from the DHT22 sensor would be displayed alongside the cell temperature over the UART serial connection to the PC.

The imaging setup was performed routinely, with the temperature ramping to a set point of 40 °C and air flowing to the clamp at 5 cc min^{-1}. Once the cantilever was

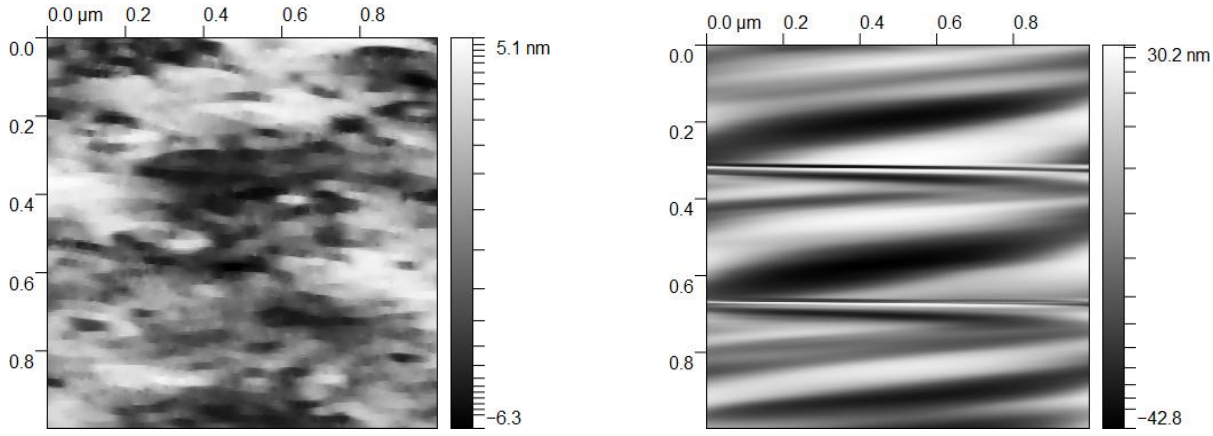

(a) (b)

Figure 2.35: 1x1 µm tapping mode height images of Nafion 212 acquired at (a) 23 °C with no air flow and (b) 40 °C with an air flow rate of 5 cc min^{-1}.

engaged with the Nafion surface, the flow of air prevented condensation from forming. Figure 2.35b depicts the first image acquired of Nafion with a cell temperature at 40 °C using air flow, which shows severe artifacts compared to the baseline image acquired at room temperature.

It was unknown at the time whether the artifacts were due to the elevated temperature or the air flow, thus four separate images were acquired while varying air flow and temperature separately to determine the root cause. Figure 2.36 depicts the 2x2 matrix of images acquired under different conditions, which shows that increasing the air flow from the baseline 5 cc min^{-1} up to the maximum of 10 cc min^{-1} has far less of an effect compared to increasing the temperature from 23 °C to 40 °C.

Having identified the issue as relating to the higher temperature of the sample, the

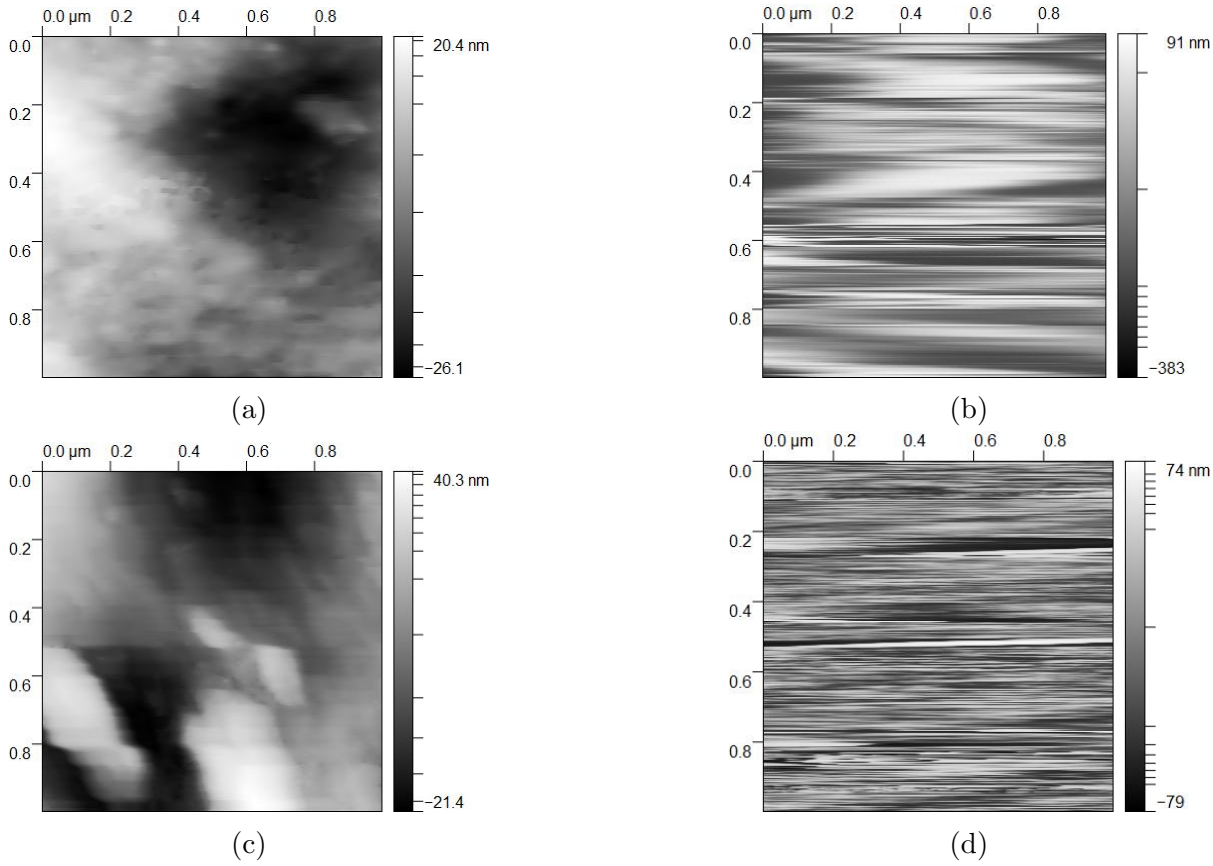

Figure 2.36: 1x1 µm tapping mode height images of Nafion 212 under different heating and air flow conditions. (a) 23 °C and 5 cc min^{-1} air flow. (b) 40 °C and 5 cc min^{-1} air flow. (c) 23 °C and 10 cc min^{-1} air flow. (d) 40 °C and 10 cc min^{-1} air flow.

first thing that became apparent was the similarity between the high temperature images and those obtained using an external electrolyte pump: both exhibit similar wave-like artifacts. This pointed to the thermal expansion and contraction of the sample due to temperature fluctuations during data capture as the most probable cause. To verify this, an image was acquired at 5 cc min^{-1} air flow and 40 °C while recording the cell temperature over the UART connection to the microcontroller. Figure 2.37 shows the plot of the temperature overlaid on the height profile of the image. This shows a clear correlation between temperature fluctuation and image height fluctuation. Thus, to

mitigate this problem, the temperature of the cell needed to be maintained within a narrower window to minimize the change in sample expansion and contraction during data capture.

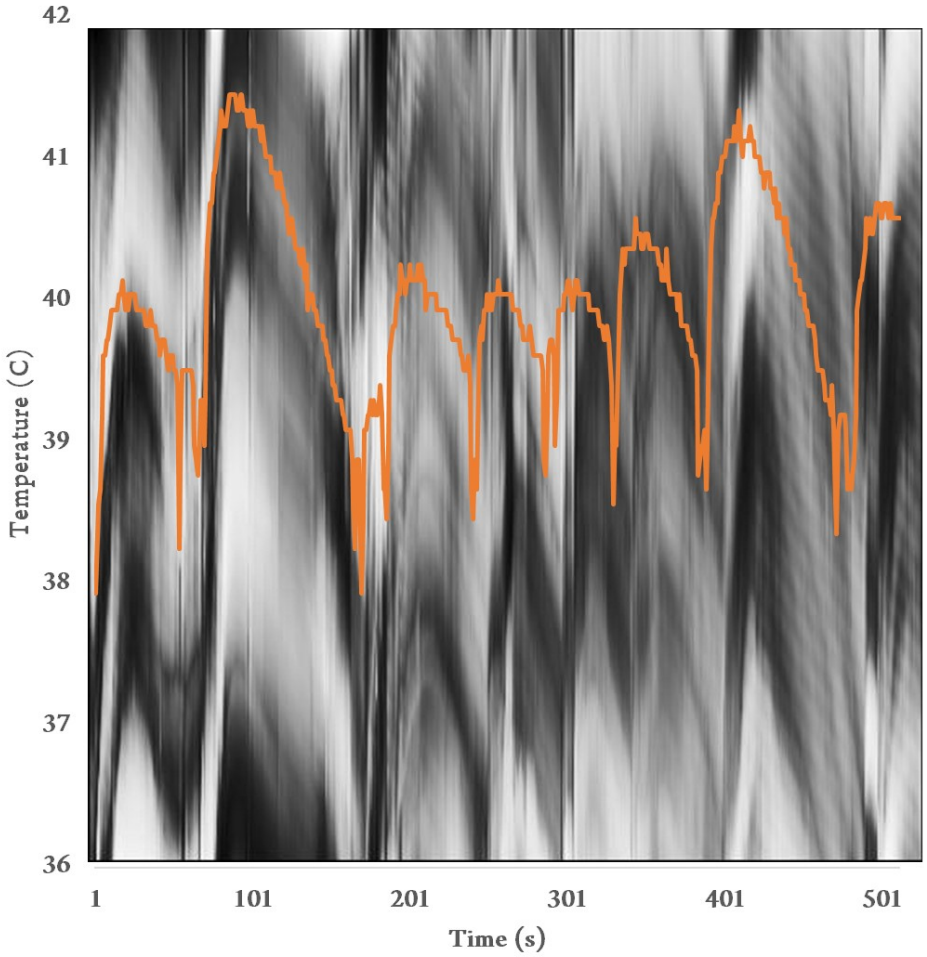

Figure 2.37: 1.5x1.5 µm height image of Nafion 212 collected in tapping mode at a cell temperature of 40 °C without proper PID tuning. The temperature profile vs time is overlaid onto the image to correlate the temperature fluctuations with the image artifacts.

While the Ziegler-Nichols method of PID tuning can lead to reliable temperature accuracy, a better tuning approach was needed. To this end, a self-tuning PID algorithm

was implemented in the microcontroller firmware. This software comprises an open loop tuning algorithm which utilizes an inflection point to mark the end point of a testing regime for a process variable (PV) which when reached, is used to calculate the PID components K_p, K_i, and K_d: those being the proportional, integral, and derivative gain constants. To initiate parameter tuning, variables such as initial manual PID components (K_p, K_i, K_d) and sample number (S) are input into the self-tuning open loop algorithm which measures the time response of PV over S until an inflection point is reached. Figure 2.38 depicts a chart of the PV and PID output vs time and highlights the calculated quantities τ, t_d, ΔPV, and $\Delta output$.

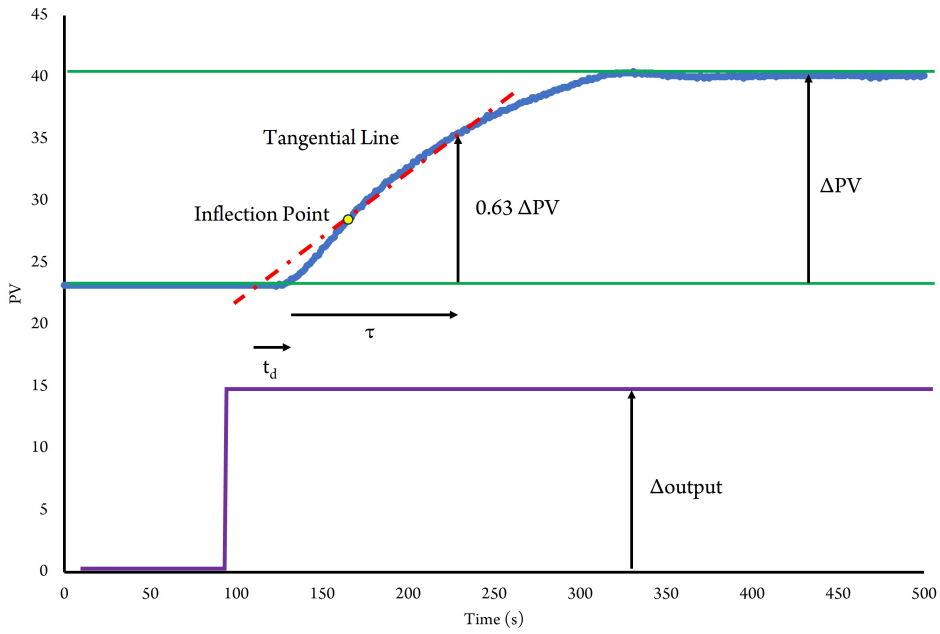

Figure 2.38: Chart depicting the process of automatic PID tuning in reference to the various quantities used.

During self-tuning, these quantities are used to calculate the appropriate PID com-

ponents. First, the process gain (pg) is calculated:

$$pg = \frac{\Delta PV}{\Delta output} \tag{2.15}$$

Once the inflection point is known, a tangential line is drawn through the inflection point to an intersection with the PV curve. The difference between the time at this point and the time when the PV began to change is the dead time (t_d). τ is found as the time difference between t_d and the time where the PV curve reaches 63% of the total ΔPV. The PID components are then calculated as:

$$K_p = \frac{0.9\ \tau}{2\ pg\ t_d} \tag{2.16}$$

$$K_i = \frac{1}{2\ t_d} \tag{2.17}$$

$$K_d = \frac{1}{0.5\ t_d} \tag{2.18}$$

These proportional, integral, and derivative gain values are then used to automatically tune the PID algorithm and ensure a non-oscillating PV with as small a difference as possible to the set point. Figure **??** depicts a chart of a manually tuned PID algorithm and a self-tuning PID algorithm implementation in the cell heating control microcontroller. The self-tuning PID algorithm reaches the set point without overshooting it and maintains the set point to within $\pm$ 0.1 °C.

The cell was set up with the heating hardware and air flow as in previous tests. The cell was allowed to reach the set point of 40 °C and air flow was set at 5 cc min^{-1}. Figure 2.40 depicts two height images obtained of Nafion 212 at 40 °C, showing minimal artifacts in the self-tuning PID control compared to the image of the same sample obtained using

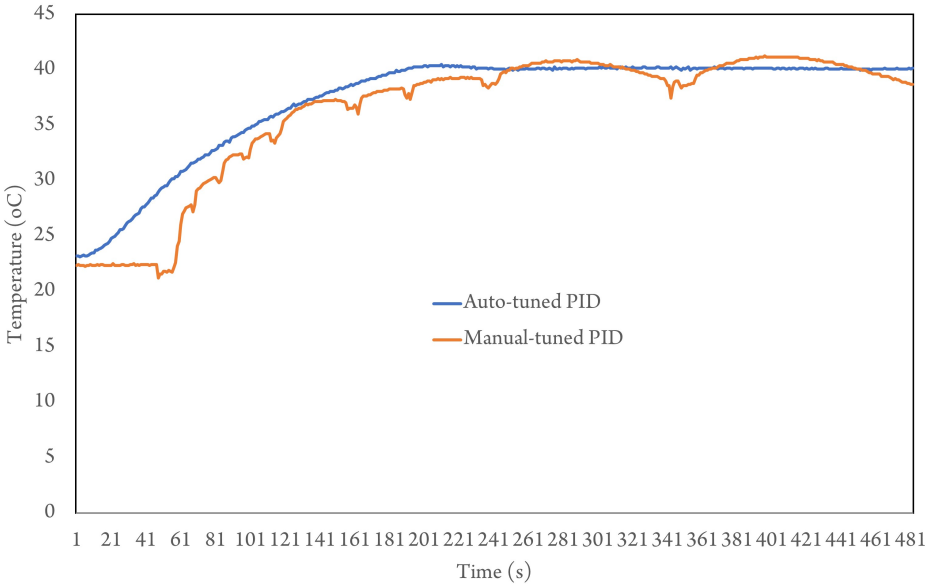

Figure 2.39: Chart depicting cell temperature versus time for the manually tuned (orange) and automatically tuned (blue) PID algorithms.

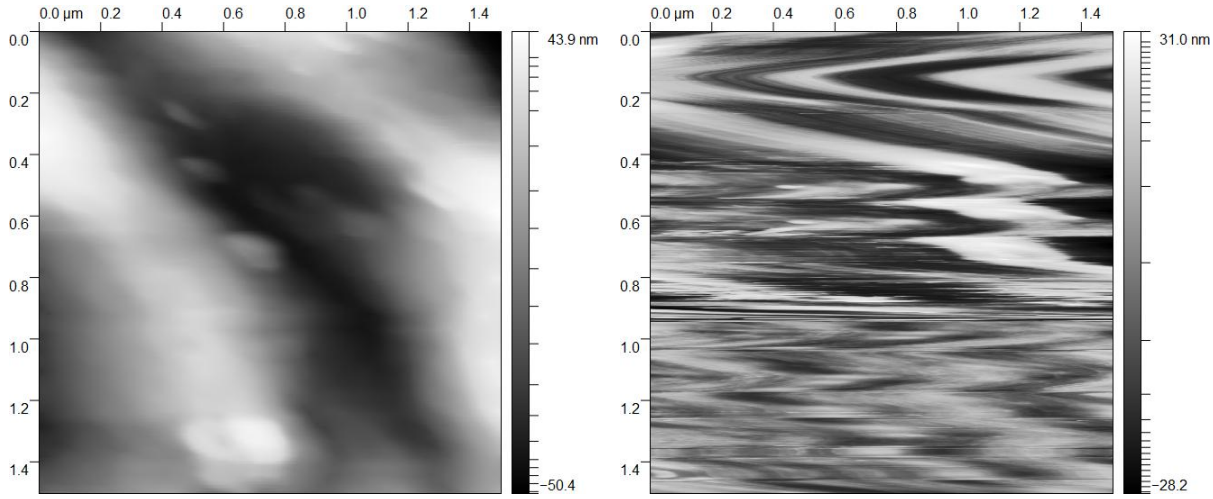

(a) (b)

Figure 2.40: 1.5x1.5 µm tapping mode height images of Nafion 212 acquired at 40 °C cell temperature and 5 cc min^{-1} air flow using (a) the automatically tuned PID algorithm and (b) the manually tuned PID algorithm.

the manually tuned PID control.

2.7 AFM Imaging Cell with Relative Humidity

To test the response to relative humidity in the cell, a sample of Nafion 212 was loaded onto the cell and no liquid was added to the cell cavity. Instead, the air tubing that had been previously used to remove condensation from the AFM optics during high temperature testing was attached to one of the cell inlets, allowing air to flow underneath the Nafion sample. Two separate images were acquired: one with low relative humidity air flow and another with high humidity air flow. To increase the humidity of the air, a water bubbler was placed between the DHT22 sensor and the flow meter.

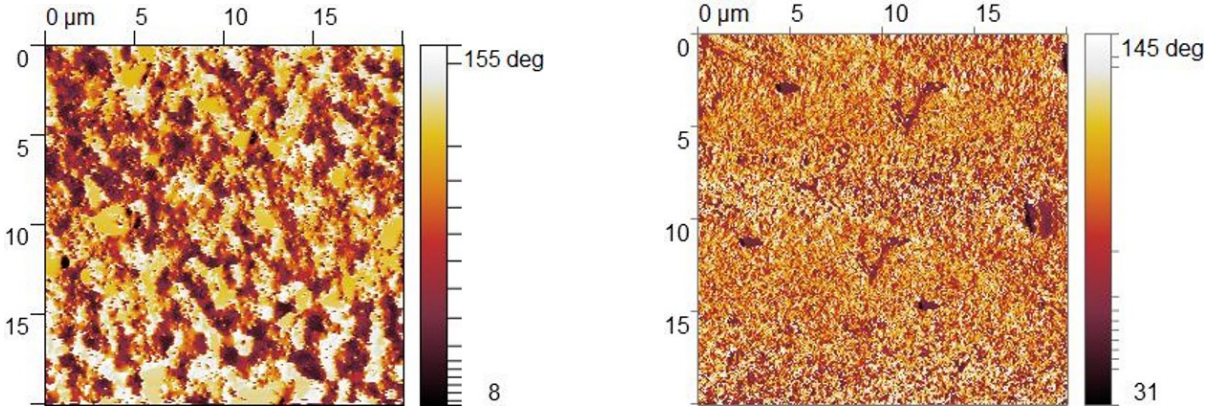

(a) (b)

Figure 2.41: 20x20 µm attractive force regime tapping mode phase images of Nafion 212 acquired at 23 °C cell temperature and 5 cc min^{-1} air flow inside the cell, with the measured relative humidity of the air being (a) 90% and (b) 14%, respectively.

The images seen in Figure 2.41 reaffirm the well-known humidity response of Nafion from previous studies, that being a large decrease in the ionic domain size distribution with decrease in relative humidity, which confirms the cell's ability to collect data with relative humidity as one of the process control variables, in addition to temperature.

2.8 Conclusion

In summary, we have developed a novel AFM imaging cell through the process of successive iteration on an initial prototype, while adding additional functionality to widen our capabilities to study ion conducting polymer membranes under real device operating conditions. We iterated on the physical shape, the manufacturing process, and the electrical connections until we had an imaging cell that was inexpensive, versatile, and capable of producing high quality AFM images of Nafion in the spatial, phase, and current domains. We validated that the cell can be used to detect faradaic proton conductivity in Nafion in conductive contact mode AFM. Finally, we added temperature control as an additional level of device simulation, with a self-tuning PID algorithm maintaining a set cell temperature, controlled via a microcontroller.

The final iteration of the device can simulate the conditions of most electrochemical devices which use an ORR cathode, and which use an IEM separator. Furthermore, the bill of materials is below $100, including the cost of the photo-sensitive resin and electronic components for temperature control and monitoring. We hope that the low cost and ease of fabrication allows for wide dissemination throughout the scientific community utilizing AFM to study electrochemical devices. In the next chapters, we detail the use of this cell in studying Nafion under VOFC conditions as well as methanol fuel cell

conditions and compare our findings to those of Nafion found under HFC conditions.

Chapter 3

Nanoscale Conductive AFM of Nafion under VOFC Conditions

3.1 Introduction

Having designed, fabricated, and demonstrated a working electrochemical AFM imaging cell that can simulate the conditions of a wide range of electrochemical energy devices, we began our investigation to collect AFM data on the structure-function relationship of Nafion under real device conditions using a vanadium oxygen fuel cell (VOFC) configuration. As discussed in Chapter 2, VOFC simulations are an excellent starting point in terms of needing limited hardware modification and having low cost, while offering valuable insights into the nanoscale behavior of Nafion in the context of a promising electrochemical energy device architecture. Furthermore, the data collected could be

compared with both past and future investigations into the nanoscale behavior of Nafion membranes to glean insights into how the operating environment affects its performance.

The main goal of this investigation was to collect images of Nafion using AFM with the Nafion acting as the proton exchange membrane for a VOFC cell. Figure 3.1 depicts the block diagram of the experimental setup. Previous studies on the structure-function relationship of Nafion using AFM were performed in the context of HFCs, using a mixture of both contact and tapping mode techniques[19][35]. It has been shown that tapping mode phase AFM can spatially resolve the ionic domains of Nafion, due to the tip-surface power dissipation which induces an amplitude frequency (phase) shift in the cantilever oscillations[85][92][56]. The presence or absence of surface water determines the phase shift, thus water-rich ionic domains can be easily distinguished from the hydrophobic fluorine-rich domains. Previously our group, led by O'dea[92][90], explored the role of tapping mode AFM as a tool to measure Nafion surface ionic domain size distribution depending on whether the AFM cantilever was operating in non-contact attractive mode or in intermittent contact repulsive mode[92]. They found that the ionic domain size correlates with the true morphology more closely in attractive mode, and that in repulsive mode the ionic domain sizes were larger than what would be expected, due to a strong coupling between the topography and phase images.

Previous conductive AFM studies on Nafion have mostly been performed in con-

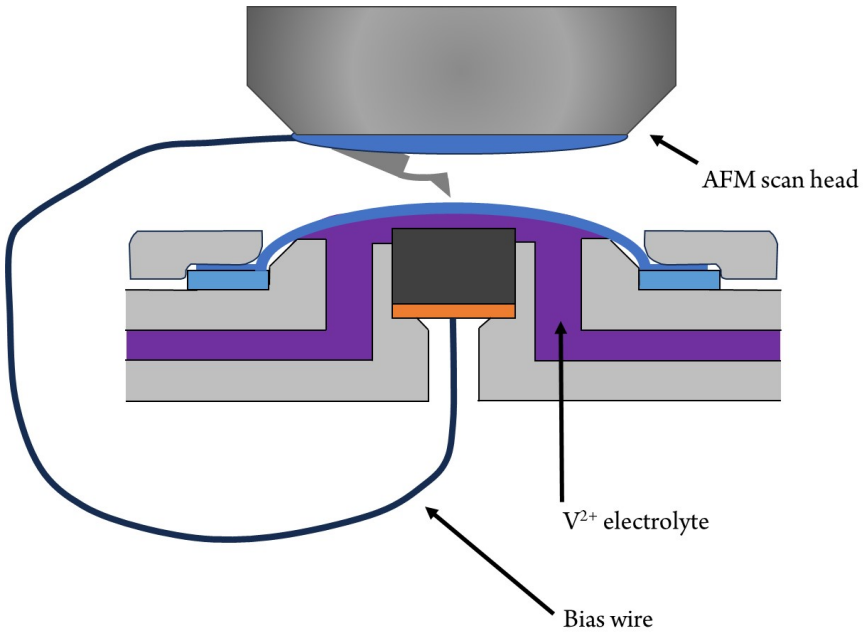

Figure 3.1: Block diagram of the experimental setup, showing the AFM scan head/cantilever holder, V^{2+} electrolyte held inside the imaging cell, and the bias wire connected to the scan head.

tact mode, as this offers the lowest tip-sample ohmic resistance[19][35][120][109]. In our group's previous investigations, to correlate the conductivity to the ionic domains, a separate phase image was acquired using tapping mode[19][35]. Due to the dynamic nature of Nafion, the surface morphology and ionic domain distribution can change between images, making correlation difficult. The approach taken previously to circumvent this problem has been to image a small area in tapping mode and then image a larger area in contact mode, with the smaller tapping mode image used to find a correlated area on the larger contact mode image[19].

In the previous chapter, we validated our novel imaging cell's ability to allow for

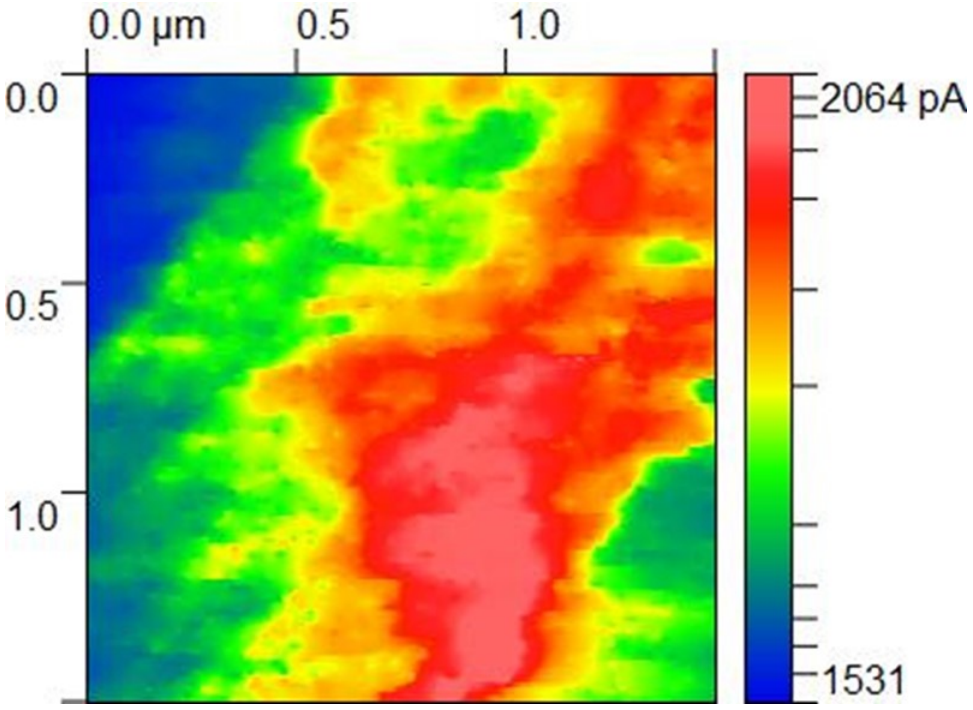

Figure 3.2: Contact mode current image of N212 under VOFC conditions, acquired during the imaging cell validation. Under 0V bias, large areas are highly conducting.

faradaic proton detection in Nafion using conductive AFM in contact mode. We showed that for the VOFC configuration, nanoampere currents were measured over a 1x1 µm area (see Figure 3.2), which is an order of magnitude higher than previous current images of Nafion in HFC configurations[19][35]. Furthermore, these currents were seen with no bias voltage applied, where HFC configured investigations needed 0.5 to 1 V to see picoampere current levels. This can be attributed to a few factors:

- **Lower Cell Resistance.** The newly developed cell used graphite as the conductive surface, whereas previous studies used metals that are prone to passivation[19][35].

- **Higher electrochemical cell potential.** The VOFC has a theoretical potential of 1.49 V, whereas the HFC only has 1.23 V.

- **Fully hydrated conditions.** The Nafion samples were exposed to dilute sulfuric acid during data collection, ensuring that they were fully hydrated.

We theorized that due to the nanoampere currents seen in contact mode, we might see picoampere currents in intermittent contact mode, also known as repulsive tapping mode. As mentioned above, repulsive tapping mode can overestimate the size of ionic domains, so there is some trade-off in spatial resolution[92]. In this chapter we demonstrate simultaneous phase-current mapping of Nafion using repulsive tapping mode AFM, with our imaging cell simulating a VOFC. With this data we accurately correlate surface ionic domains with high current areas. This technique allowed us to map the spatial proton conductivity of Nafion at the nm scale under VOFC conditions without any bias voltage. Figure 3.3 is a graphical representation of the different tapping mode force modes overlaid onto a Lennard-jones potential[40], which accurately models the attractive and repulsive forces acting on the AFM cantilever tip as a function of tip-sample distance.

To measure the effect of vanadium electrolyte on the nanoscale pore morphology of Nafion, we used attractive tapping mode phase images with the cell filled with aqueous solutions of acids and electrolytes. We compared this data to the phase images acquired in repulsive tapping mode to quantify the loss of spatial resolution and to determine what percentage of the surface is ionically active under VOFC conditions. As Nafion is sold in different thicknesses and equivalent weights, we studied both Nafion 212 and Nafion 117 membranes (see Table 1.1).

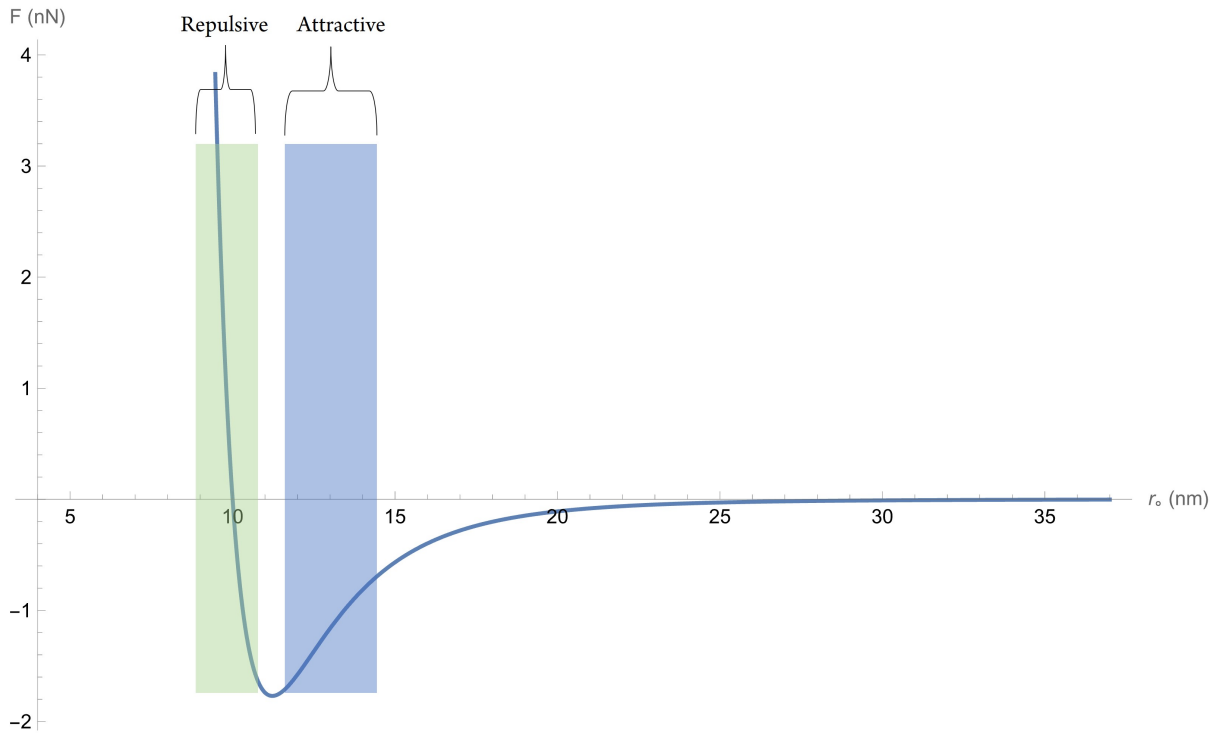

Figure 3.3: Chart depicting a plotted Lennard-jones potential of force (nN) versus distance (nm) of a typical AFM cantilever in non-contact mode, with the green area representing the repulsive force mode and the blue representing the attractive force mode.

We explored the relationship between surface pore morphology and the concentration of both sulfuric and hydrochloric acids inside the imaging cell using attractive tapping mode AFM, with DI water as our baseline comparison point. We collected this data to determine if the pore morphology of Nafion was affected by acid concentration, as this could help explain some of the discrepancies between its behavior under HFC conditions versus VOFC conditions. By using hydrochloric and sulfuric acids, we investigated what effects the counter anion had on Nafion morphology. We exposed Nafion to sodium sulfate solutions and imaged them to test whether ionic strength or pH alters the phase

domain morphology compared to a DI water baseline.

By following these lines of investigation, we hoped to draw conclusions about the surface morphology and conductivity of Nafion under VOFC conditions and compare these findings to previous AFM findings on Nafion under HFC conditions.

3.2 Methods

The imaging cell described in a previous chapter was used to simulate a VOFC cell inside an MFP-3D AFM from Oxford Instruments (Santa Barbara, USA). Nafion 212 (N212) and 117 (N117) membrane samples (The Fuel Cell Store, Texas) were prepared by boiling them in 5% hydrogen peroxide for 1 hour, followed by boiling in de-ionized (DI) water for 1 hour, then boiling in 1M sulfuric acid for 1 hour, and finally by boiling in DI water again for 1 hour. The boiled Nafion samples were cut into circles with a diameter of 25mm using a utility knife and stored in DI water until use. To prepare for imaging, a Nafion sample was first clamped down onto the cell gasket using 1/16th inch bolts. Next, the seal was checked by flowing DI water through the cell using a luer-lock fitted syringe attached to the 3mm ID tubing on the cell connections. Once this was complete, the cell, 50 mL of 1.4M V^{2+} in 2.5M H_2SO_4 (see Appendix 1) stored in a sealed polypropylene bottle, a luer-lock fitted syringe, and various containers for waste and DI water were placed inside of a glove bag. Nitrogen gas was then allowed to flow through the glove bag

for 20 minutes before it was sealed and filled with nitrogen. The cell was then filled with the V^{2+} electrolyte using the syringe and the cell fluid connections were closed off using attached valves. For samples which were studied as a function of cell fluid composition, prepared Nafion samples were simply loaded onto the cell and the fluid injected using a Luer lock fitted syringe.

Once fully assembled, the cell was removed from the N_2-filled glove bag and placed into the AFM imaging stage and the bias wire was connected to the ORCA current sensor. Tapping mode images were collected using a Pt-coated cantilever with a resonant frequency of 350 kHz and a spring constant of 42 N m^{-1} (MikroMasch, USA). Contact mode images were collected using a Pt-coated cantilever with a spring constant of 0.2 N m^{-1} (MikroMasch, USA). Each cantilever had a tip radius of 25 nm. Image processing and statistical analysis were performed in Gwyddion, an open-source scanning microscope image analysis software. Ionic domain coverage and average size were analyzed using grain segmentation, with Otsu's method used for thresholding on the phase images acquired[76]. Briefly, Otsu's method is a thresholding technique which uses an image grayscale intensity histogram to find an optimal threshold to separate "foreground" pixels from "background" pixels. Due to the known correlation between the phase-contrast and spontaneous surface segregation of hydrophobic and hydrophilic domains in Nafion, Otsu's method can be used to find the optimum thresholding value to separate the domains according to the pixel values in each image. This method is preferred to manual

thresholding because it can be applied to any image regardless of the range of pixel grayscale intensities, which can vary significantly between different AFM images of the same sample.

Due to the Nafion samples being exposed to air during data collection, oxygen would readily diffuse into the cell through the membrane and oxidize the V^{2+} to V^{3+} after about 30 minutes, which was the window of time used to collect each image, with images typically taking 8-12 minutes to collect. The cell was "reset" with fresh V^{2+} electrolyte between separate images, using the same steps described.

3.3 Imaging Nafion Proton Conductivity and Phase Simultaneously under VOFC Conditions

Figure 3.4 depicts the images of N212 obtained in repulsive tapping mode, showing simultaneous height (3.4a), phase (3.4b), and current (3.4c) images. As predicted, the high faradaic currents seen in contact mode allowed us to image picoampere current in intermittent contact mode. Figure 3.5 depicts 3 images, with Figure 3.5a and 3.5b being extracted masks of Figures 3.4b and 3.4c, respectively. For 3.4c, we chose to select only the highly conducting areas, thus the grain threshold was set at 25 pA. Figure 3.5c is the result of the addition of 3.5a and 3.5b, showing where the phase and current positively

(green) and negatively (blue) overlap, as well as where the water-rich phase areas (yellow) and current (purple) do not overlap.

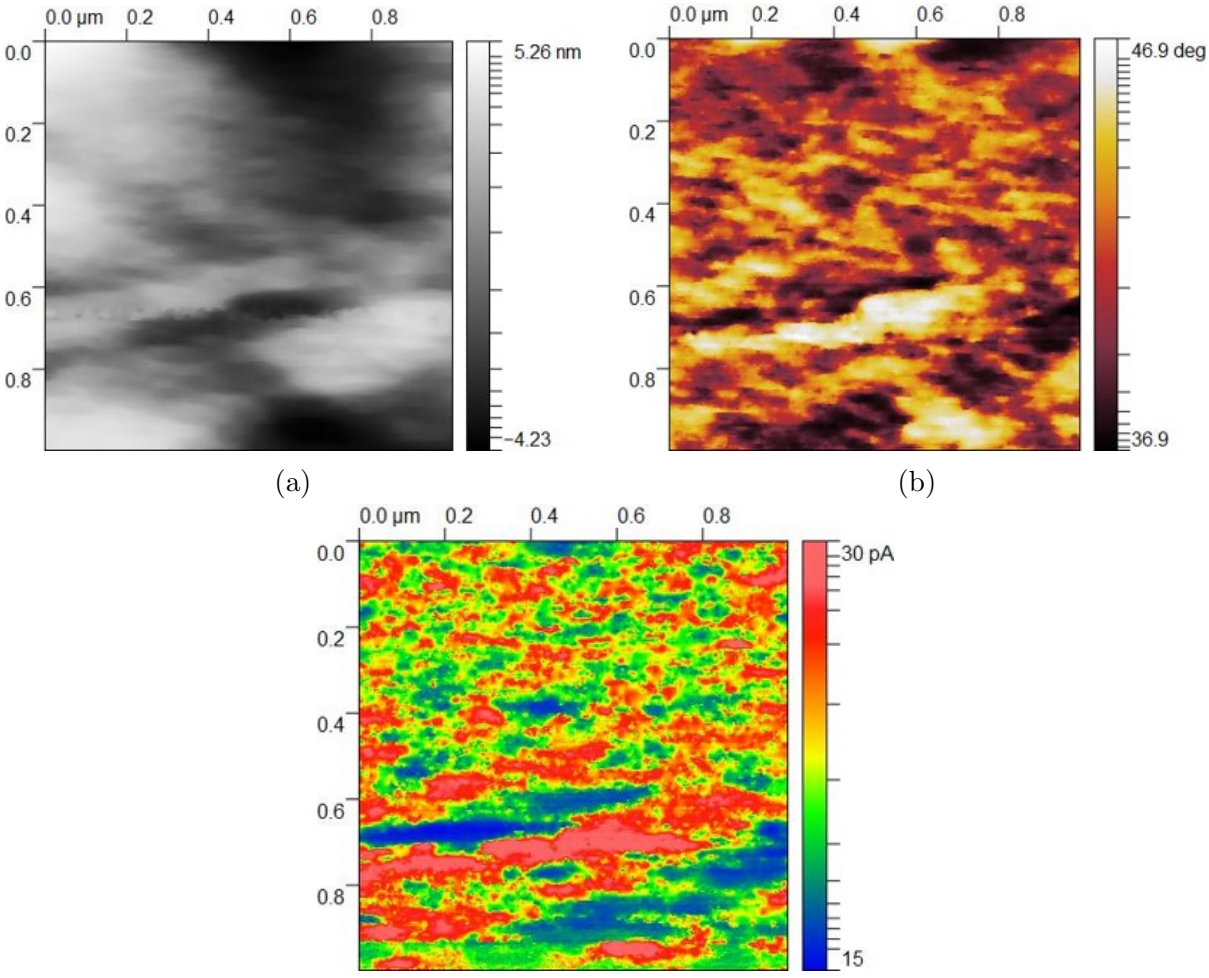

Figure 3.4: 1x1 µm AFM images of N212 under VOFC conditions in repulsive tapping mode. (a) Height image. (b) Phase image. (c) Current image.

Figure 3.6 is a subset of the phase and current data of the same sample from Figure 3.4, with a plot of extracted line profiles from the phase and current which shows a positive correlation. This is expected; in repulsive mode, higher tip-sample power dissipation

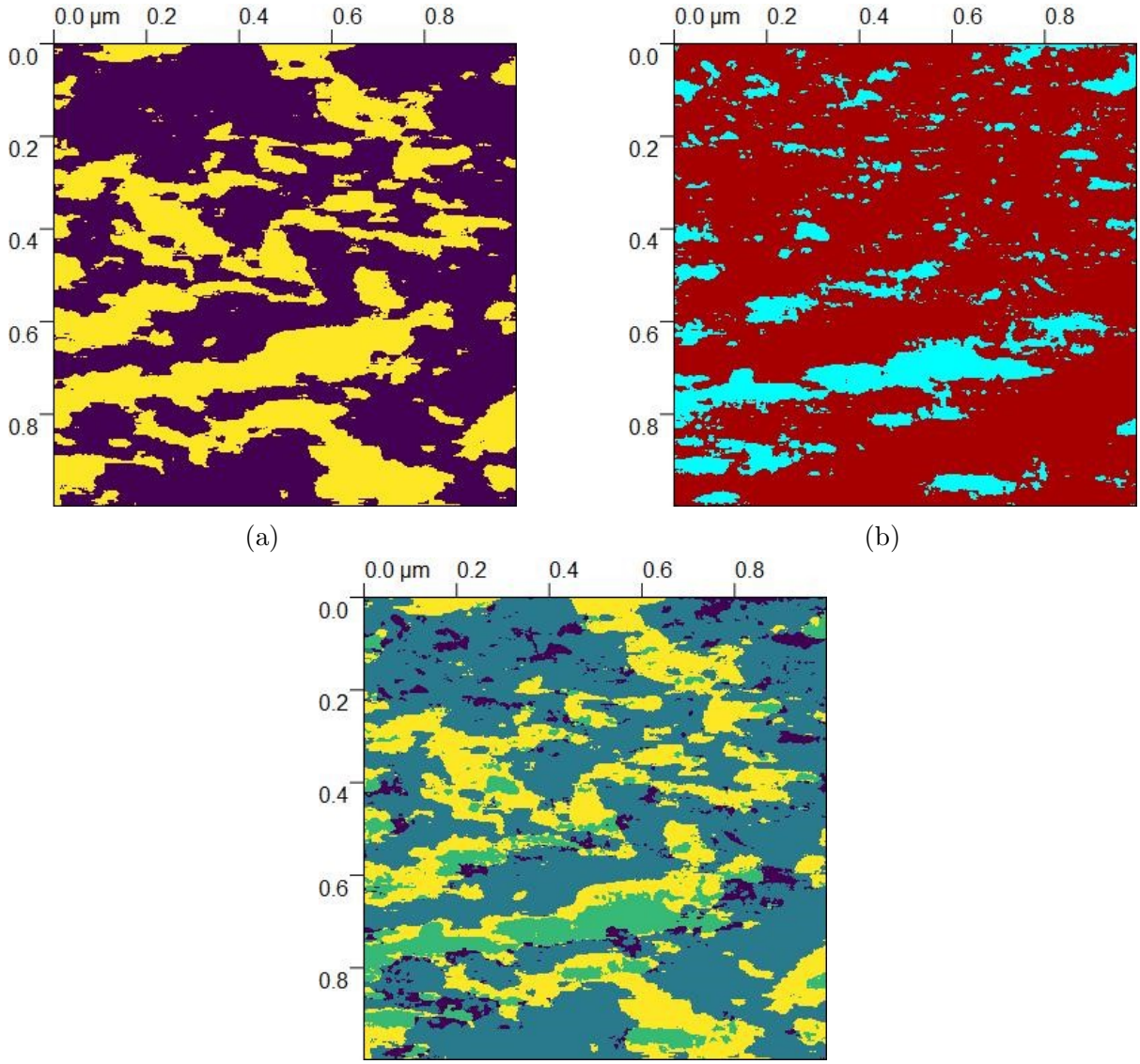

(a) (b)

(c)

Figure 3.5: (a) Extracted ionic domain area of 3.4b using thresholding. (b) Extracted highly conducting areas of 3.4c using a threshold of 25 pA. (c) Combined pixel image of (a) and (b), showing positive overlap between the ionic domains in 3.4b and high conducting domains in 3.4c as green, non-conducting ionic domains as yellow, non-ionic domains as blue, and non-overlapped conducting areas as purple.

should result in a positive frequency shift and vice versa[92]. While this validates our method of current data collection, due to the inherent drawbacks of repulsive tapping mode it is difficult to draw conclusions about the relative number of highly conducting

ionic domains under VOFC conditions. We opted to compare our current data collected in repulsive mode with phase data collected separately in attractive mode to determine what percentage of the surface should be conducting based on the number of visible domains. We could then measure the repulsive mode images to determine the ionic domain area with a correction factor, allowing us to make a more accurate estimation of the relative number of highly conducting ionic domains measured in Figure 3.4.

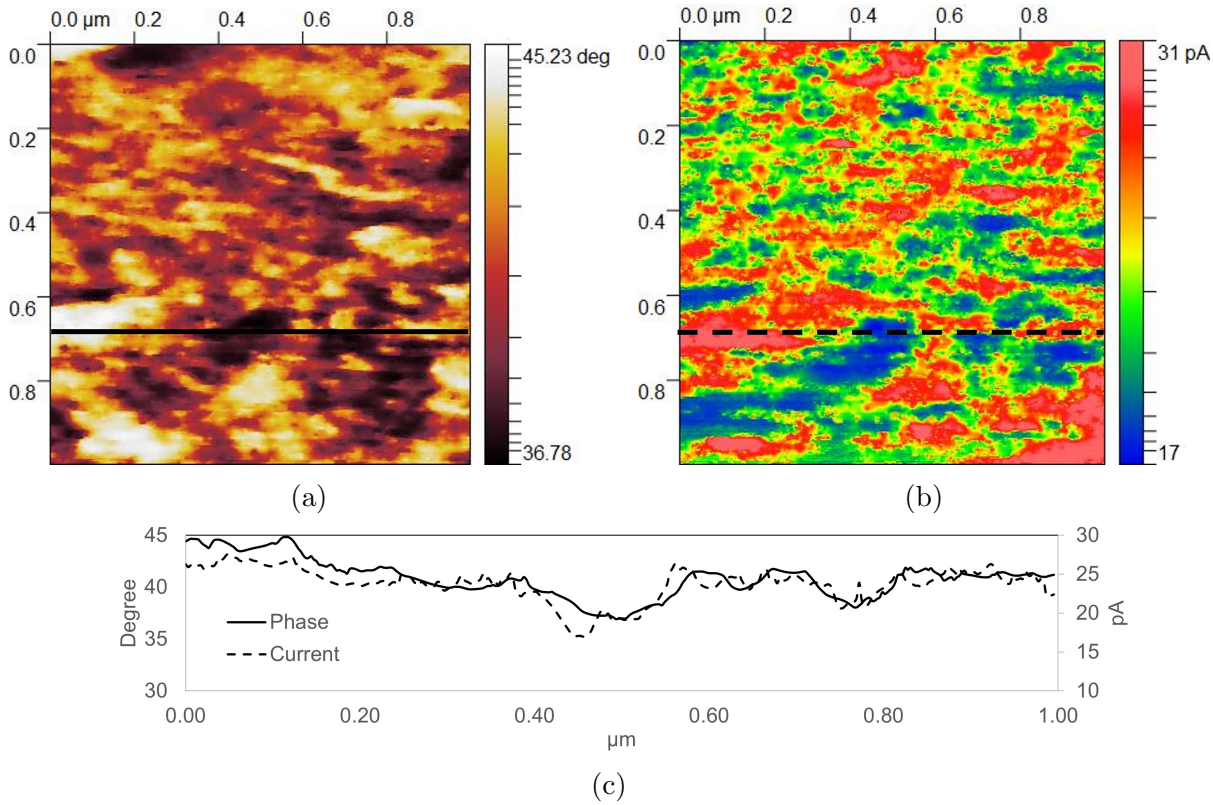

Figure 3.6: 1x1 µm (a) repulsive phase contrast image of N212 under VOFC conditions, (b) simultaneously acquired current image of (a), and (c) overlaid phase and current profiles, with the horizontal profile lines shown on (a) and (b).

As a point of comparison, we imaged N117 under VOFC conditions, which differs

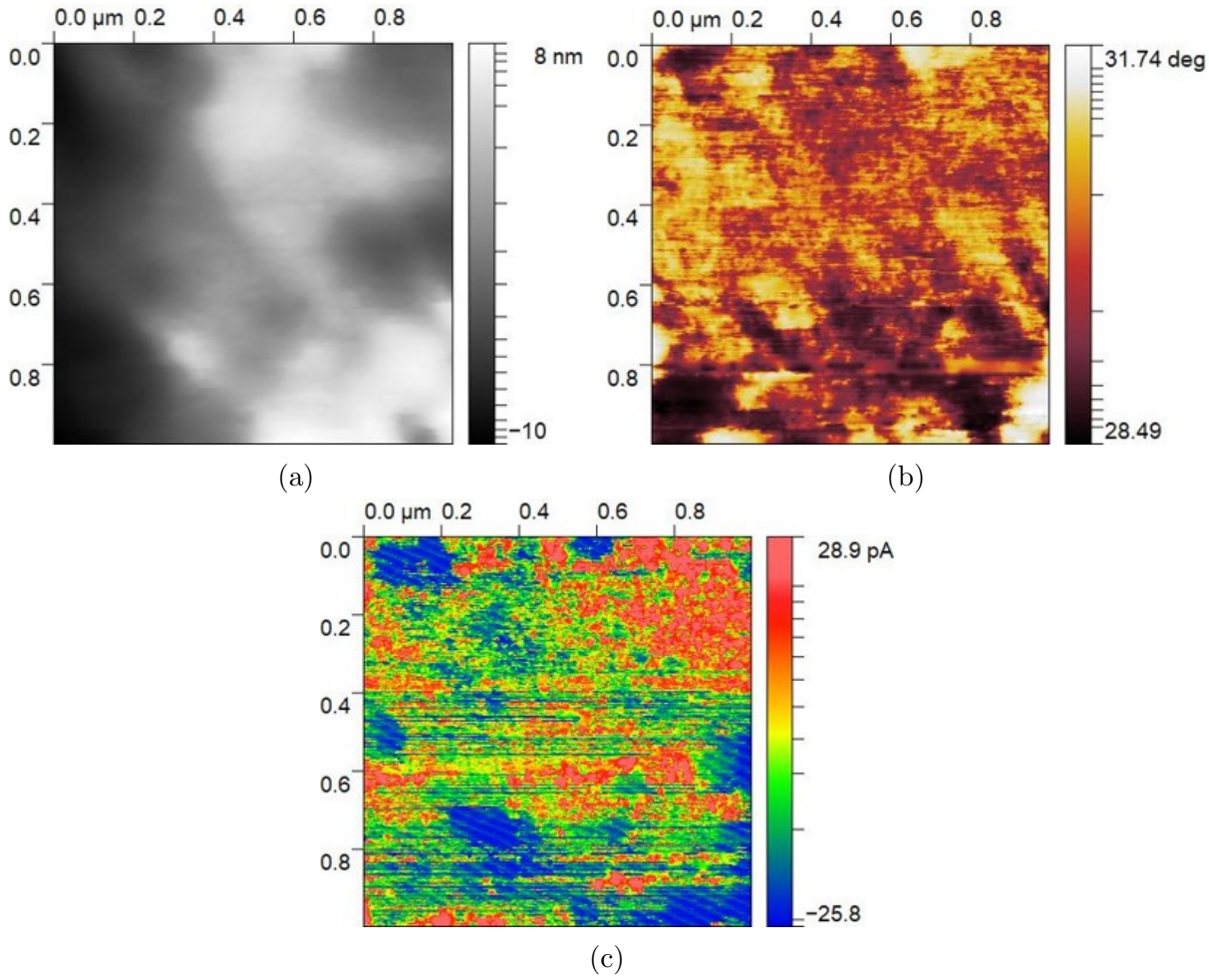

Figure 3.7: 1x1 µm AFM images of N117 under VOFC conditions in repulsive tapping mode. (a) Height image. (b) Phase image. (c) Current image.

from N212 in equivalent weight (1100 g mol^{-1} for N117 vs 990 g mol^{-1} for N212) and membrane thickness (180 µm for N117 and 50 µm for N212). Figure 3.7 depicts the repulsive tapping mode height, phase, and current AFM images acquired of N117 under VOFC conditions. For N117, the phase-current does not correlate as closely as seen in N212.

3.4 Phase Imaging Nafion Exposed to Different Fluids

Figure 3.8 depicts phase images of N212 and N117 exposed to V^{2+} electrolyte using attractive tapping mode (Figures 3.8b, and 3.8e) and repulsive tapping mode (Figures 3.8c and 3.8f), along with an attractive mode phase images with each sample exposed to only DI water (Figures 3.8a and 3.8d). Th average grain size of each image was determined, with the results shown in Table 3.1.

Cell Fluid	Membrane	Force Mode	Mean Grain Diameter (nm)
DI H_2O	N212	Attractive	40
V^{2+}/H_2SO_4	N212	Attractive	9
V^{2+}/H_2SO_4	N212	Repulsive	16
DI H_2O	N117	Attractive	51
V^{2+}/H_2SO_4	N117	Attractive	7
V^{2+}/H_2SO_4	N117	Repulsive	11

Table 3.1: Comparison of the mean grain diameters of the images in Figure 3.8, showing the differences between N212 and N117 as well as showing the disparity between attractive and repulsive force imaging modes.

Qualitatively, the N212 sample in Figure 3.8b shows a higher density of small "dark" ionic domains over the surface compared to Figure 3.8a, which has a lower density of larger "dark" ionic domains. Furthermore, the "bright" ionic domains seen in Figure 3.8c are larger on average than the "dark" ionic domains seen in Figure 3.8b, which aligns with the work of O'dea et al[92], being slightly less than 50% larger on average. Importantly, ionic domains cover ∼38% of the surface of Figure 3.8b, which we can compare to the percentage of highly conducting (>25 pA) areas from Figure 3.4c, with those

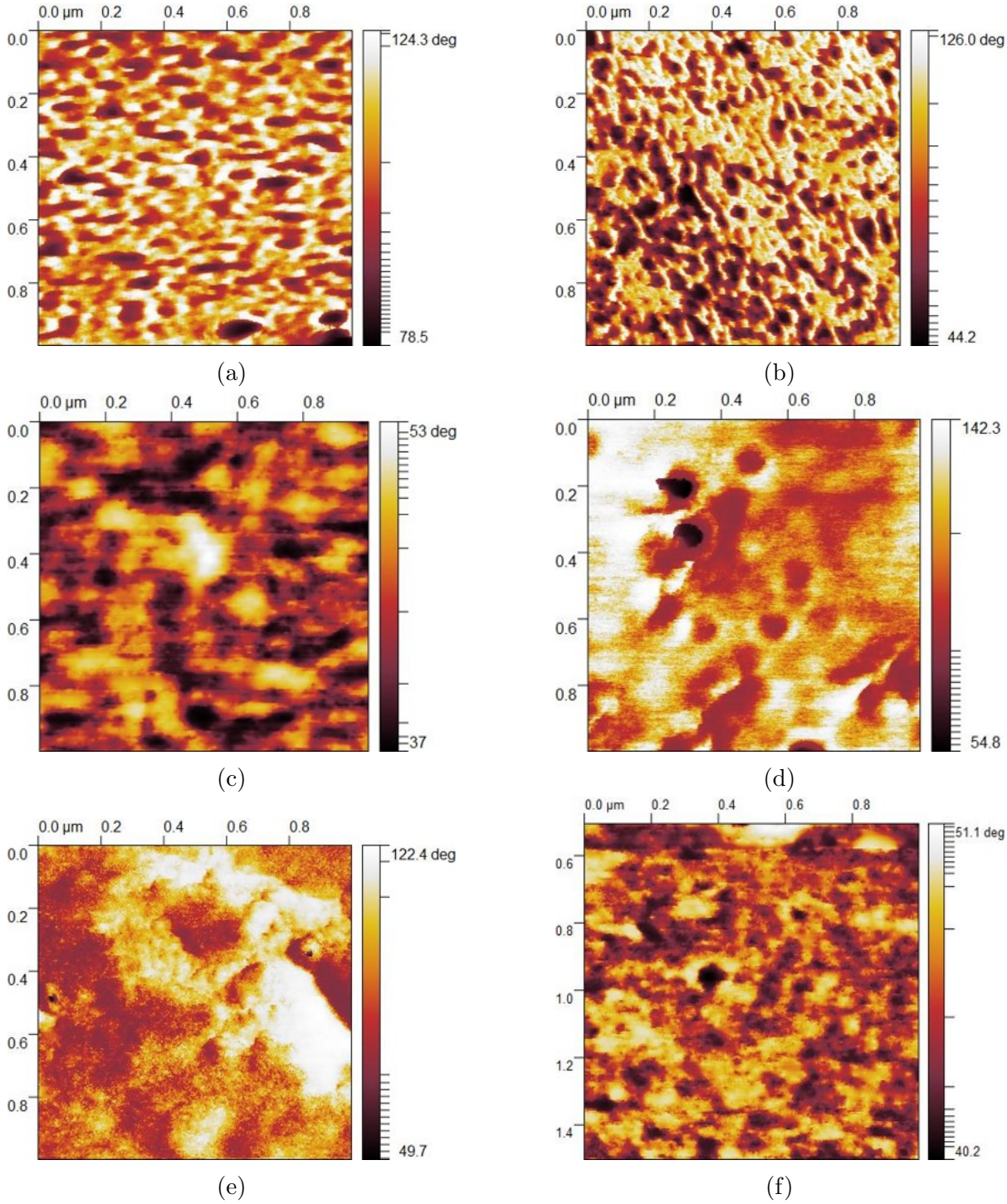

Figure 3.8: 1x1 µm phase images of Nafion. (a) N212 in attractive mode exposed to DI water. (b) N212 in attractive mode exposed to V^{2+} electrolyte. (c) N212 in repulsive mode exposed to V^{2+} electrolyte. (d) N117 in attractive mode exposed to DI water. (e) N117 in attractive mode exposed to V^{2+} electrolyte. (f) N117 in repulsive mode exposed to V^{2+} electrolyte.

accounting for ∼17% of the total area. Applying a correction to the repulsive mode phase image in 3.4b yields a total ionic area of ∼19%. This agrees with the ionic area in 3.8b at ∼21%. Thus, out of the total ionic domains available on the surface, we measured that ∼89% are highly conducting under VOFC conditions. We compare this to previous findings of Nafion under HFC conditions in later sections. This is supported by our contact mode current data in Figure 3.2 which shows that for N212, large portions of the surface are highly conductive.

Performing the same analysis on N117 using data from Figures 3.7 and 3.8, we can see that by applying the same high conductivity cutoff (>25 pA) on 3.7c shows that only 6% of the total area is highly conducting. We used the same >25 pA cutoff as N212 because the current ranges are very similar. Using the phase-correction factor from the N117 data in Figure 3.8 yields a total ionic area of ∼38% in 3.7b. Thus, only ∼16% of the available ionic domains in the N117 sample in Figure 3.7 are highly conducting.

3.4.1 Phase-Response of Nafion Exposed to Varying Concentrations of Acids

Due to the visible difference in ionic domain size and density between Figures 3.8a (DI water) and 3.8b (V^{2+} electrolyte), we sought to explore the relationship between acid concentration inside the imaging cell and the attractive mode phase images of Nafion

samples on the cell. From these figures, the N212 sample exposed to only DI water has larger ionic domains than the sample exposed to vanadium electrolyte. Figures 3.9b-3.9f are a set of phase images acquired of N212 with increasing concentrations of sulfuric acid inside the cell. The average ionic domain diameters are plotted versus sulfuric acid concentration in Figure 3.9a.

From the dataset in 3.9 there is a clear relationship between acid concentration and average ionic domain size, with the domains shrinking in diameter with increasing concentration (see Figure 3.9a. To see what effect the acid anion had on the nanoscale surface domain size we acquired a set of phase images of N212 under the same set of conditions as in Figure 3.9 except the acid species was changed from sulfuric to hydrochloric acid. These are shown in Figure 3.10b-3.10f, along with a plot of the average ionic domain diameter vs HCl concentration in Figure 3.10a.

Here again we see the same relationship between acid concentration and average ionic domain size as was seen with sulfuric acid. This data suggests that the acid anion has little effect on the domain size, but rather that the pH of the electrolyte is the main causal agent. Figure 3.11 contains attractive mode phase images of N117 when exposed to 0.5M, 1M, and 4M H_2SO_4. We captured these images to determine if the pH/domain relationship held for a thicker membrane. Grain segmentation analysis seen in Figure 3.11a shows average ionic domain radii which follow the same general trend seen in N212

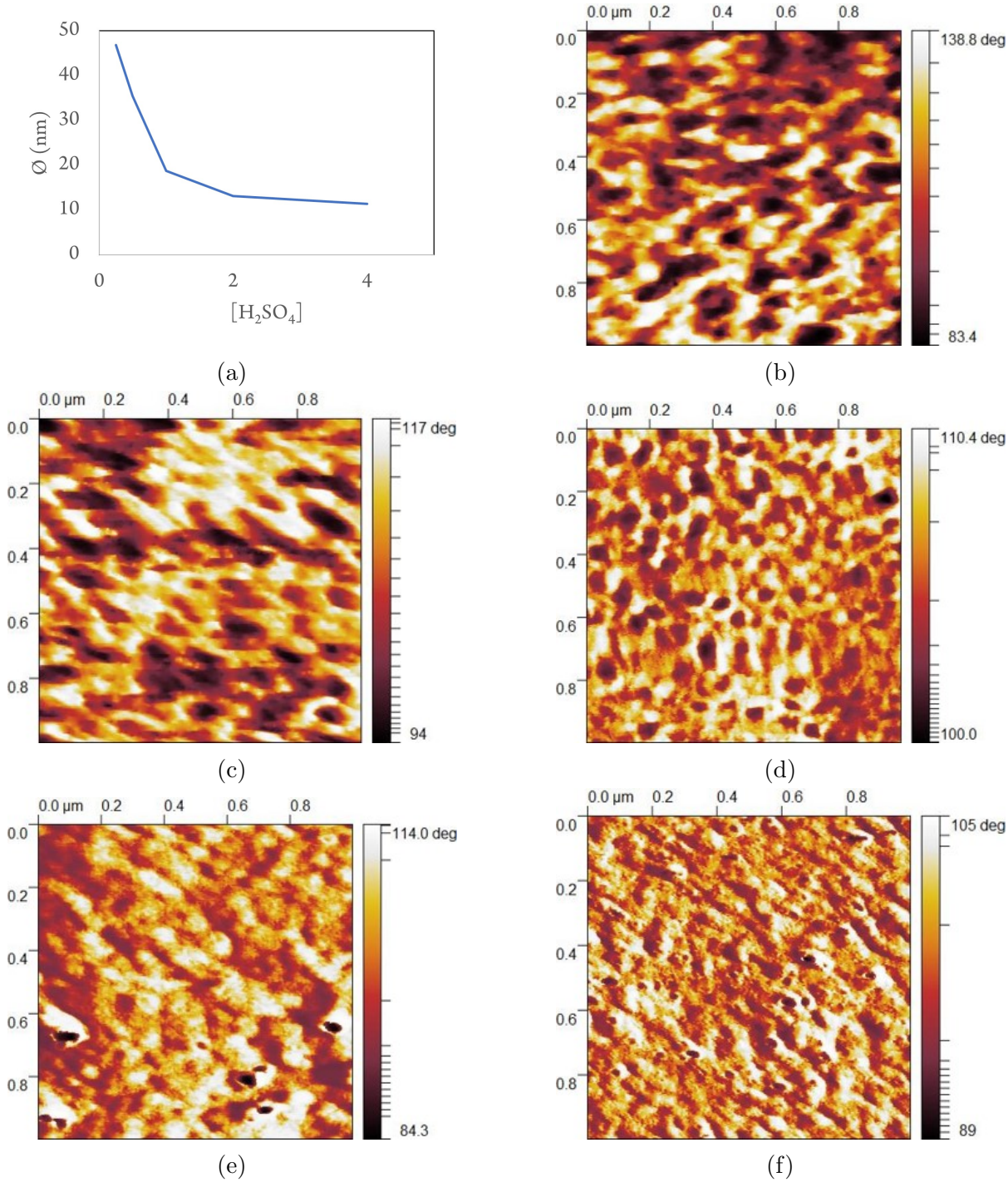

Figure 3.9: 1x1 µm attractive mode phase images of N212 exposed to increasing concentrations of H_2SO_4. (a) Plot of the average grain diameters of (b) (0.25M), (c) (0.5M), (d) (1M), (e) (2M), and (f) (4M) versus H_2SO_4 concentration.

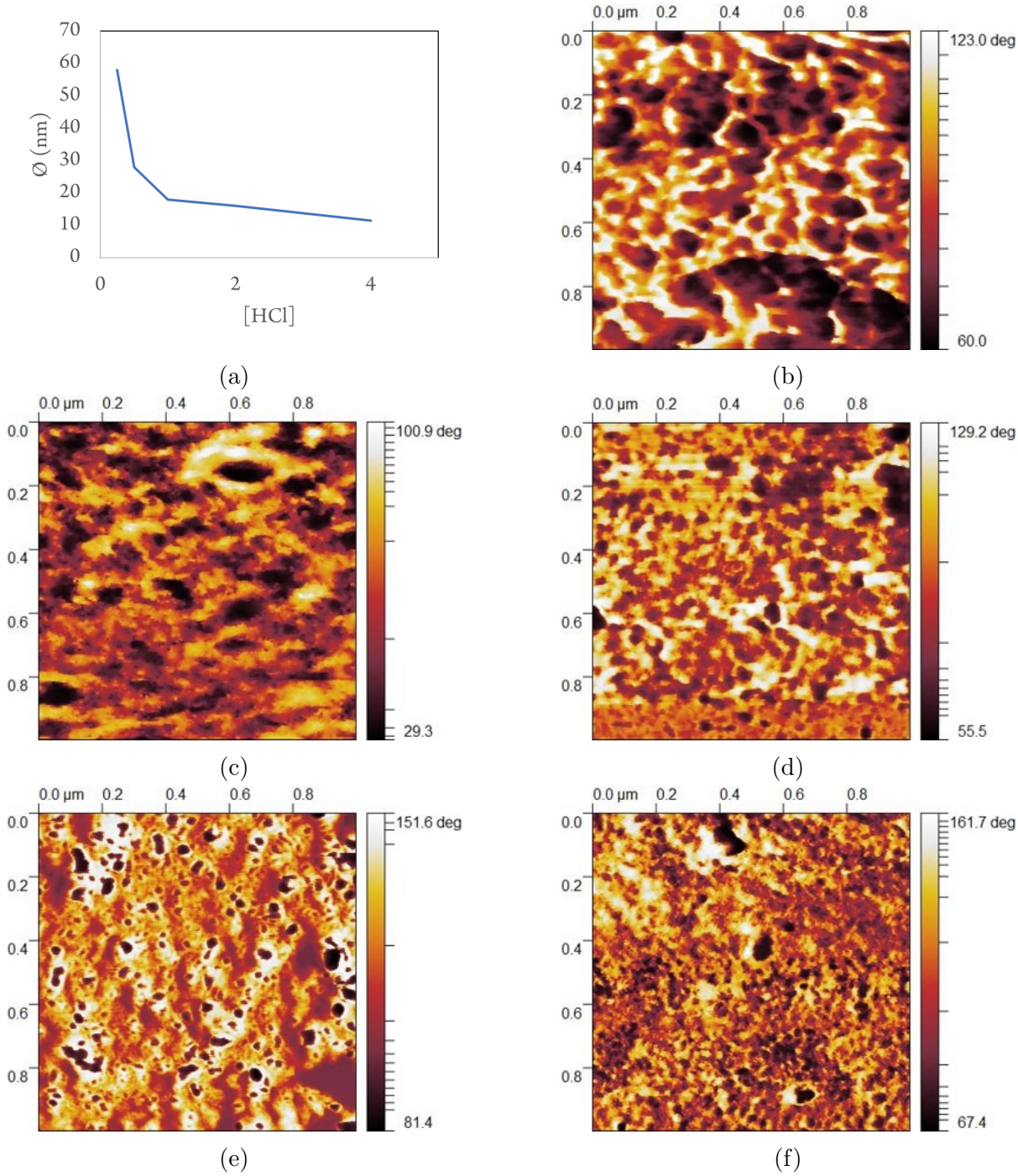

Figure 3.10: 1x1 µm attractive mode phase images of N212 exposed to increasing concentrations of HCl. (a) Plot of the average grain diameters of (b) (0.25M), (c) (0.5M), (d) (1M), (e) (2M), and (f) (4M) versus HCl concentration.

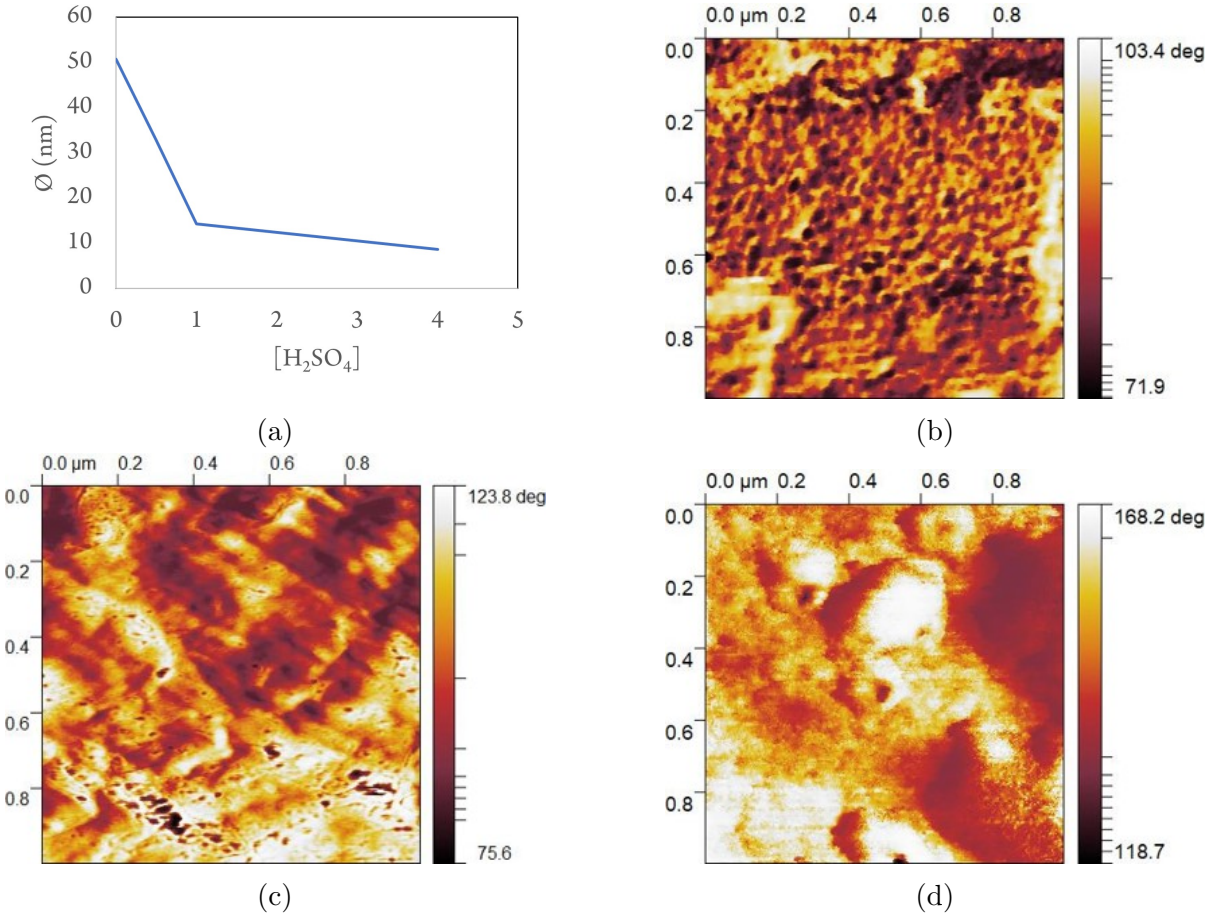

Figure 3.11: 1x1 µm attractive mode phase images of N117 exposed to increasing concentrations of H_2SO_4. (a) Plot of the average grain diameters of (b) (0.25M), (c) (1M), and (d) (4M), versus H_2SO_4 concentration.

(see Figure 3.9a).

3.4.2 Phase-Response of Nafion Exposed to Sodium Sulfate

To test whether the decrease in ionic domain size was due to the increase in the ionic strength of the acid solutions, we imaged N212 and N117 with the cell filled with 1M Na_2SO_4, which if true, would show similar morphology as those imaged while exposed to

1M H_2SO_4. Figure 3.12 shows the attractive mode phase images from this study. The samples exposed to 1M Na_2SO_4 show similar morphology to those exposed to 1M H_2SO_4, with ionic domain radii being smaller on average than those exposed to only DI water and larger than those exposed to 2-4M H_2SO_4. These average ionic domain radii obtained via grain segmentation analysis are compared in Table 3.2. This data supports the hypothesis that Nafion surface domain sizes shrink when exposed to liquids of increasing ionic strength as compared to those only exposed to DI water. The mean grain sizes are slightly smaller for those samples exposed to neutral sodium sulfate compared to the same concentration of sulfuric acid.

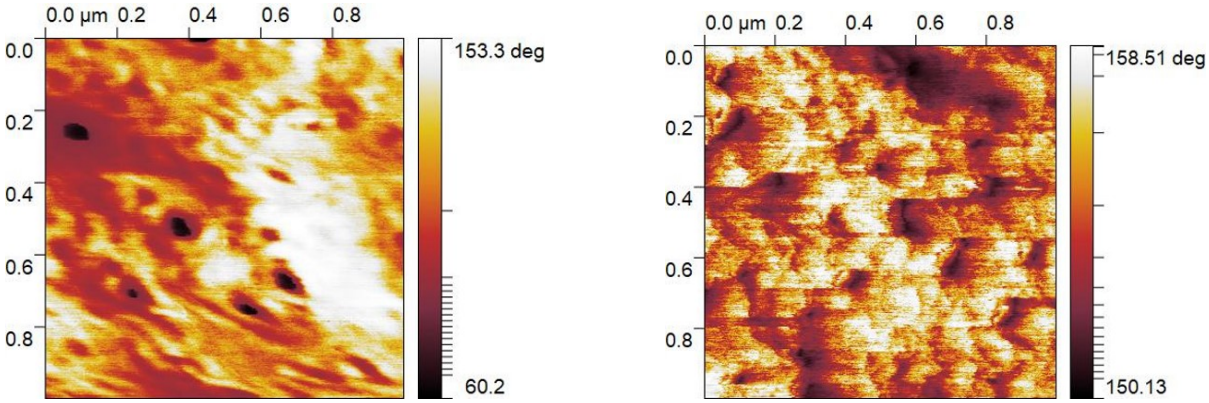

(a) (b)

Figure 3.12: 1x1 µm attractive mode phase images of (a) N212 and (b) N117 exposed to 1M Na_2SO_4 solution

Cell Fluid	Membrane	Mean Grain Diameter (nm)
1M H_2SO_4	N117	14
1M Na_2SO_4	N117	9
1M H_2SO_4	N212	19
1M Na_2SO_4	N212	16

Table 3.2: Comparison of the mean grain diameters of the images in Figures 3.9d (N212 with 1M H_2SO_4), 3.11c (N117 with 1M H_2SO_4), 3.12a (N212 with 1M Na_2SO_4), and 3.12b (N117 with 1M Na_2SO_4).

3.5 Discussion

From Figure 3.4, we can see that a large majority of the ionic domains in N212 are highly conducting under VOFC conditions. Skylass-Kazacos et al studied VOFCs using 2M V^{2+} electrolyte and found that the catalyst and conductive carbon electrode pretreatment were the main determining factors in the device power density[100] as opposed to membrane type. However, they also showed that replacing Nafion 115 with an anion exchange membrane (Fumasep FAP-450) resulted in a loss in theoretical energy capacity (80% to 65%), which they attributed to higher membrane resistance and a lower proton transfer rate. Charvát et al studied the effect of different membranes on VOFC performance and found that thinner, more conductive membranes (N212) had a large, positive impact on overall performance compared to thicker, more resistive membranes (N117), which had a negative impact[23]. They also found that vanadium ion permeation to the cathode did not negatively impact performance as much as would have been expected, especially for thinner membranes like N212. They determined that under normal operating conditions, the water formed during the ORR at the cathode can dilute any permeated vanadium ions such that they will not bind or alter the active catalyst sites. Our find-

ings corroborate their study, with N212 showing a high current density over a larger percentage of available ionic domains over the surface under VOFC conditions compared to N117, a thicker membrane. Any deleterious effects due to vanadium permeation in N212 were not present in our study, as we showed high current density despite obvious vanadium permeation during data collection, as discussed in the previous chapter.

While studying the attractive mode tapping AFM phase images of N212 and N117 exposed to varying concentrations of strong acids, it was clear that there were visible surface ionic domain changes in response to these liquids, with the trend showing a decrease in average ionic domain diameter with increasing acid concentration. We imaged Nafion while exposed to a neutral pH 1M sodium sulfate solution as a comparison with 1M sulfuric acid and found the phase images to be qualitatively similar, which implies that Nafion contracts when exposed to solutions of increasing ionic strength compared to exposure to only DI water.

In 1992, Cwirko et al studied the pore size of Nafion samples exposed to increasing concentrations of salt and found that pore radii shrink with increasing salt concentration based on the Bragg spacing of X-ray diffraction data[27]. Indeed, many researchers have studied Nafion's response to concentrated ionic/acidic solutions to better understand how Nafion performs as a ion exchange membrane in the chlor-alkali process[96][22][64][49]. Two prevailing models[112] have been used to predict experimental findings on the pore

size of Nafion versus ionic strength: the Donnan model[33] and Manning's counter-ion condensation theory[81]. Beers et al studied counter ion condensation in N117 and found that exposure to concentrations of over 0.06M HCl resulted in "deswelling" of domains as measured using SAXS Bragg spacing and by solution uptake[11]. They found that once an external electrolyte concentration passes a certain threshold, the electrolyte ions can enter the Nafion pore structure due to having a higher chemical potential than the uncondensed or free ions inside the membrane. As more ions enter the pores, the perodic structure of Nafion contracts. They postulate this contraction being due to electrostatic screening[32] of sulfonic acid charged groups.

Previous studies on the proton conductivity of Nafion under HFC conditions found that roughly 30% of the measured ionic area is highly conducting[19], which is much lower than the ∼90% of ionic area which is highly conducting that we measured under VOFC conditions in the case of the thinner (50 µm) N212 membrane, but better than the ∼16% of highly conducting areas in the thicker (178 µm) N117 membrane. For N212, this stark difference in conductivity can be attributed to a few reasons:

- **Access to catalyst sites.** Under HFC conditions, for an ionic domain in Nafion to conduct it must be directly connected to an active catalyst site at the anode where hydrogen is oxidized to protons[19][35]. For VOFCs no catalysts are needed to provide protons: the electrolyte provides them over the entire area of the membrane.

- **Ohmic losses.** As discussed in the previous chapter, we designed our imaging

cell around reducing ohmic losses during data collection, whereas previous studies under HFC conditions suffered from high ohmic losses and needed a bias voltage applied to see any current[19][35].

O'Dea et al measured the attractive-mode phase ionic domain coverage of Nafion under HFC conditions (70% relative humidity) using AFM and found that roughly 25% of the surface consisted of ionic domains[92]. This is higher than the ∼21% and coverage we measured under VOFC conditions, which, according to our findings, we can attribute to the shrinkage of the membrane in response to exposure to high ionic strength electrolyte. While the ionic domain coverage is smaller under VOFC conditions, the percentage that are highly conducting is much greater, which can be due to the reasons listed above. For N117, the poor VOFC performance can be attributed to at least one of the reasons identified by Charvát et al, namely higher ohmic resistance[23]. The other reason they identified was that N212 could more easily prevent cathode flooding during operation by removing water via osmosis compared to N117, which would not be contributing factor in our investigation due to using an ultra-microelectrode as a cathode.

3.6 Conclusions

In this study we investigated the nanoscale proton conductivity of Nafion membranes under VOFC conditions and found that N212 is highly conductive as compared to Nafion under HFC conditions while N117 is less so. Our study corroborates previous findings on

the performance of VOFCs using different thickness membranes. We also found through our investigation exposing Nafion to varying concentrations of acids and salts that it shrinks when exposed to solutions of increasing ionic strength, which corroborates previous experimental and theoretical work.

Chapter 4

Nanoscale Conductive AFM of Nafion under DMFC Conditions

4.1 Introduction

In previous chapters, we had focused our investigations into Nafion at the nanoscale in the context of VOFCs, which was a steppingstone towards nanoscale investigations of Nafion in the context of VRFBs. Having developed a novel imaging cell for these investigations, we wanted to use it to explore the structure-function response of Nafion under direct methanol (DMFC) conditions. These fall under the umbrella of small organic molecule fuel cells (SOMFCs), which oxidize a liquid fuel at the anode using a catalyst at relatively low temperatures, with the ions (protons or hydroxides) from the methanol oxidation reaction (MOR) migrating to the cathode through an ion exchange

membrane where they facilitate the ORR to form water. These can either operate under neutral or under strongly alkaline conditions[7], with the latter having shown the best performance[14]. Figure 4.1 depicts the block diagram for a typical DMFC utilizing a proton exchange membrane architecture. DMFCs have been heavily researched as viable energy conversion devices for portable applications[63][17], due to their high energy density, low cost, and ease of use compared to pressurized hydrogen gas[17]. Table 4.1 lists the various properties of methanol compared to hydrogen gas.

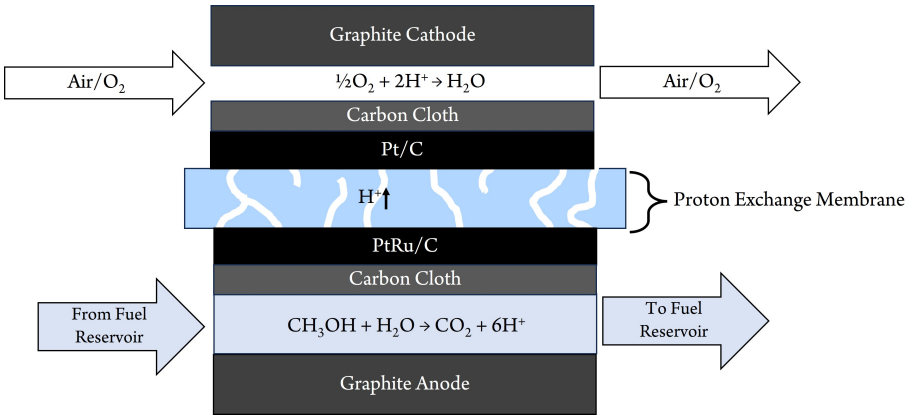

Figure 4.1: Block diagram of a typical DMFC using a Pt/C cathode and a PtRu/C anode to catalyze the ORR and MOR, respectively.

Unfortunately, using methanol directly in a fuel cell has drawbacks which have hindered its widespread adoption:

- Incomplete oxidation on Pt/PtRu catalysts to CO, resulting in catalyst deactivation due to CO irreversibly binding to active sites[9][43].
- High crossover flux through proton exchange membranes, resulting in fuel oxidation at the cathode[60] and low efficiency.

- Pure methanol is highly toxic and flammable[36].

Furthermore, due to the second point in the list, practical methanol concentrations are limited to below 5% w/w for use in DMFCs[60][78], which negates the high energy density advantage seen in Table 4.1. These drawbacks have spurred research into new catalysts tailored for the specific challenges of DMFCs[77], along with alternative membranes to mitigate fuel crossover[30].

Fuel	E_{cell} at pH=0	Volumetric Energy Density
Pressurized H_2	1.23V	2.75 MJ L^{-1} (360 atm)
Methanol	1.2V	15.9 MJ L^{-1}

Table 4.1: Theoretical open circuit voltages for the H_2/O_2 and the CH_3OH/O_2 reactions, as well as the volumetric energy densities of pressurized H2 and pure methanol.

Very little research has been conducted on the nanoscale structure-function relationship of Nafion, or any ion exchange membrane[71][44], under DMFC conditions. In our research group, Economou et al investigated the surface morphology of Nafion when exposed to methanol, with varying levels of success in performing such experiments using AFM[34]. They studied Nafion under DMFC conditions using the previously described modified polyheater cell, flowing a dilute methanol solution to a half-MEA sample using a peristaltic pump at very low flow rates. Using tapping (AC) mode conductive AFM, they measured a few hundred picoamperes of peak current on highly conducting domains[34]. Affoune et al used tapping mode AFM phase to study Nafion samples that had been exposed to methanol prior to imaging, finding that there was a significant degree of swelling[2].

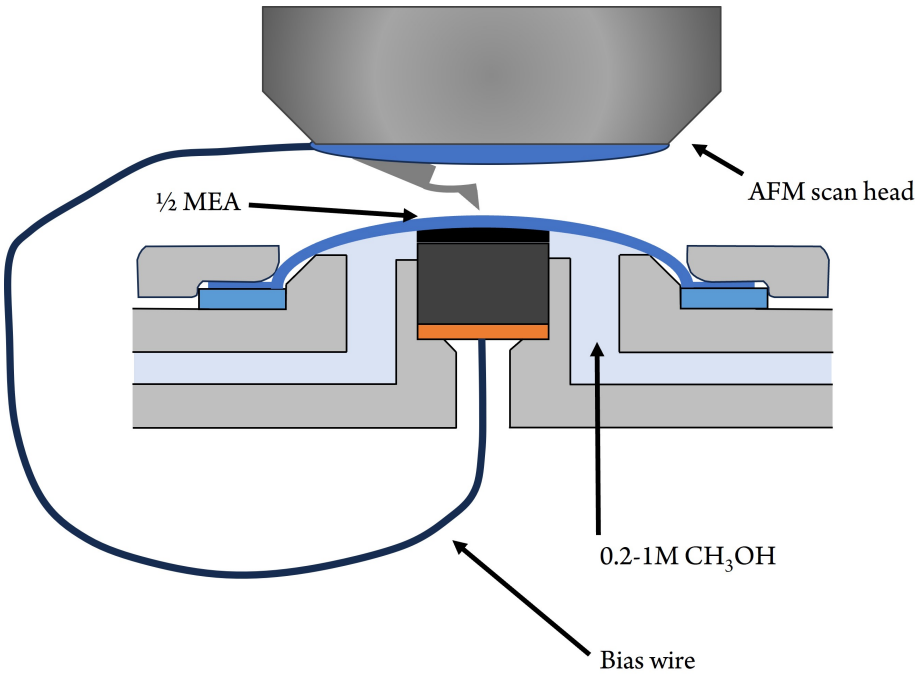

Figure 4.2: Block diagram of the experimental setup used for this investigation. To help drive the electrochemical reactions, a voltage bias was applied to the anode.

There is a need for a better understanding of how Nafion behaves at the nanoscale under simulated DMFC conditions, which we could obtain using our novel imaging cell. Using this, we studied Nafion 212 (N212) and 117 (N117) membranes under DMFC conditions using a variety of AFM techniques. The aim of this study was to determine what percentage of the surface of Nafion is ionically active/water rich, what percentage of those domains are highly conducting, and what the degree of swelling is under DMFC conditions at the nanoscale. Figure 4.2 depicts a block diagram for the experimental setup for the experiments that were carried out in this study.

4.2 Methods

N212 and N117 samples were purchased from the Fuel Cell Store (Texas, USA) and were boiled in 5% H_2O_2, DI water, 1M H_2SO_4, and finally DI water again for an hour each. The boiled Nafion samples were cut into circles with 25mm diameters using a utility knife. 6mm circles were punched out of a carbon cloth electrode with a microporous layer containing 2 mg Pt/cm^2 catalyst loading. With these electrodes, half membrane electrode assemblies (1/2 MEAs) were made by compressing prepared Nafion samples onto an electrode at 250 °C and 1500 PSI, using a hot-press. They were compressed for 3 minutes each, with the finished 1/2 MEAs stored in DI water until use. Nanoscale images of Nafion were acquired using an MFP-3D AFM from Oxford Instruments (Santa Barbara, CA). Pt-coated SiN cantilevers (Mikromasch, USA) were used to collect data. For tapping mode images, cantilevers had a force constant of 40 N m^{-1} and a resonant frequency of 75 kHz. For contact mode images, cantilevers had a force constant of 0.2 N m^{-1}. A 1.25V bias was applied to all samples during data collection to overcome the overpotentials for methanol oxidation.

To simulate a DMFC, we loaded prepared 1/2 MEAs onto our previously described imaging cell and filled the cell with various concentrations of methanol in DI water, with the carbon cloth electrode on each sample touching the graphite electrode of the cell. Samples were allowed to equilibrate for 45 minutes prior to data collection. Image analysis was performed using Gwyddion, an open-source scanning microscopy imaging analysis

software package. We performed grain segmentation using Otsu's method in Gwyddion to analyze the size and total areas of the ionic domains in the phase images of Nafion under DMFC conditions, as described in the previous chapter.

4.3 Phase Imaging Nafion exposed to Methanol Solutions

Figure 4.3 depicts the attractive mode tapping mode phase images of N212 and N117 while exposed to 0.2M, 0.5M, and 1M methanol solutions. The ionic domain average diameters of the samples in Figure 4.3 were analyzed and plotted in Figure 4.4. These samples show significant swelling compared to previous studies of Nafion under HFC conditions and exposure to V^{2+} electrolyte, which corroborates previous studies of Nafion exposed to methanol solutions[34][2]. As seen in the previous chapter, when exposed to only DI water, Nafion swells in comparison to solutions of high ionic strength, which show shrinkage. The mean grain diameter of both N117 and N212 exposed to 0.2M methanol are smaller than those found when exposed to only DI water in the previous chapter: 51nm versus 22nm and 40nm versus 26nm for N117 and N212, respectively. Due to the limited number of images taken, a relationship is difficult to establish. The differences in mean grain size may be due to the limitation of Otsu's method of thresholding[76] in comparing samples taken at different times and under different conditions. However, the

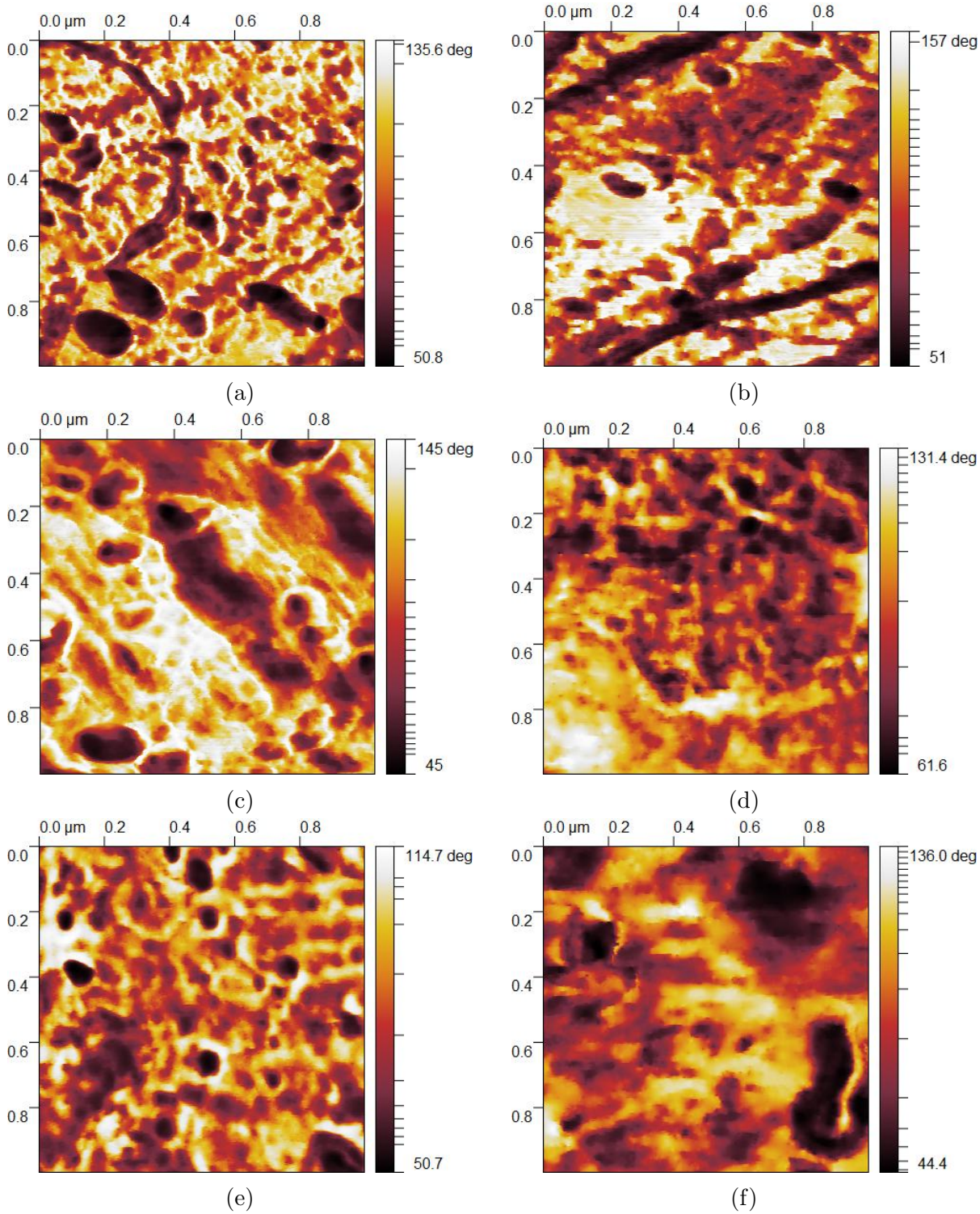

Figure 4.3: 1x1 µm attractive mode phase images of N212 (a-c) and N117 (d-f) 1/2 MEAs exposed to ((a) and (d)) 0.2M, ((b) and (e)) 0.5M, and ((c) and (f)) 1M methanol.

images in Figure 4.3 were acquired on the same two N212 and N117 1/2 MEA samples exposed to increasing concentrations of methanol and a trend is clear- the samples swell with increasing methanol exposure[103], as seen in Figure 4.4.

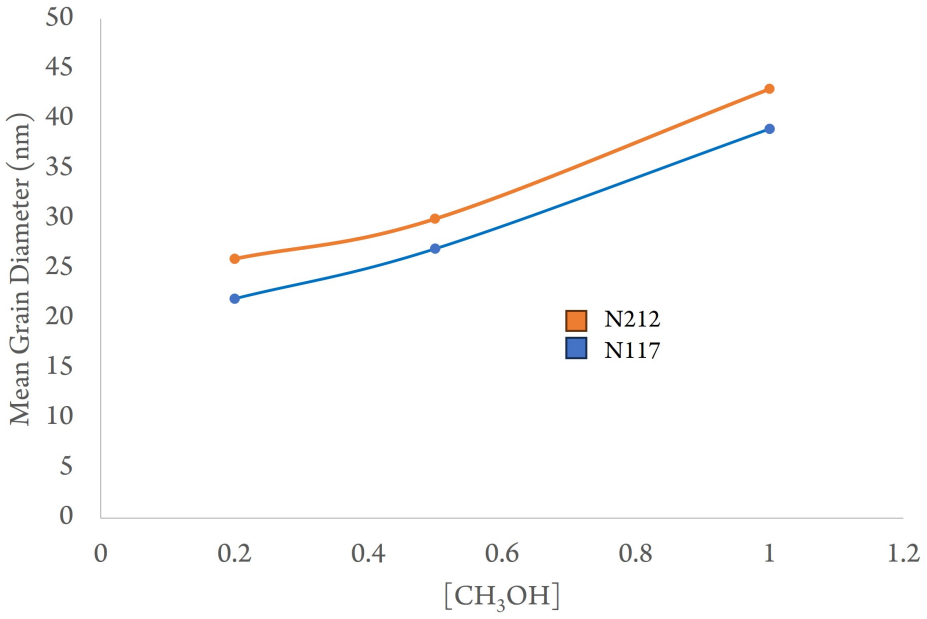

Figure 4.4: Chart depicting the mean ionic grain boundary diameters of the 1/2 MEAs in Figure 4.3 versus methanol concentration.

4.4 Conductive AFM of Nafion under DMFC conditions

Figure 4.5 depicts the contact-mode AFM current images obtained of N212 and N117 1/2 MEAs with 2mg Pt cm^{-}2 catalyst loading while exposed to 1M methanol. Figures 4.5a and 4.5b show clear Faradaic proton conductivity due to the oxidation of methanol at the

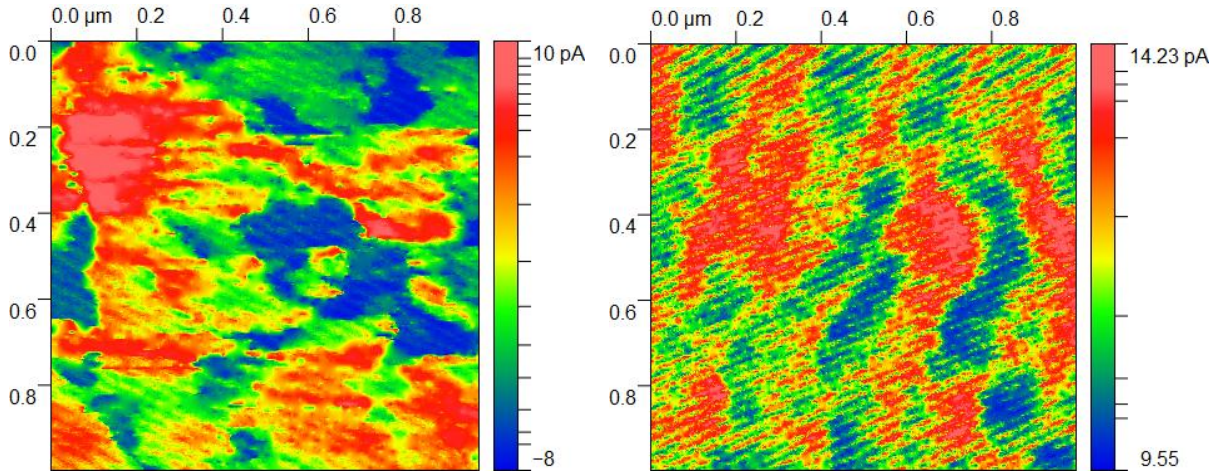

(a) (b)

Figure 4.5: 1x1 µm contact-mode current images of N212 (a) and N117 (b) 1/2 MEAs exposed to 1M methanol.

Pt-rich anode. The scale bars on each image show similar (∼10-15 pA) ranges of proton conductivity, which is less than both the VOFC samples studied in the previous chapter (∼2-3 nA) and less than tapping-mode current images of DMFC samples previously obtained by our group (∼100-400 pA)[34]. The ohmic resistance due to imperfect contact between the MEA (held down using a plastic clamp) and the graphite would lower MOR current density. Other factors contributing to the low conductivity while in contact mode could have been:

- **Low temperature.** The cell was kept at room temperature (∼20 °C), while DMFC operation is normally between 50-80 °C[62].

- **Methanol crossover.** Methanol that had diffused through the Nafion could be catalytically oxidized at the Pt-coated cantilever tip in the presence of atmospheric oxygen[60]. Partial oxidation would create CO adsorbents which could decrease

the activity of the tip towards oxygen reduction to water[9].

- **Anodic catalyst.** The catalyst layers in the electrodes used to create the 1/2 MEAs for this study only contained Pt, while PtRu co-catalysts are known to be more effective for the MOR and are less prone to CO-poisoning[77].

Using the same simultaneous phase-current imaging techniques that were used in the previous chapter to study Nafion under VOFC conditions, we imaged the N212 and N117 1/2 MEAs in repulsive tapping mode using Pt-coated cantilevers with the cell filled with 1M methanol. As seen in Figure 4.6, the results align with those found by Economou et al[34], showing ∼100-300 pA of current on the highly-conducting areas. Unlike the samples used to simulate a VOFC, there are large areas that are non-conducting, which is also seen in the contact-mode images in Figure 4.5. It is unknown why we see higher currents in the tapping mode images compared to the contact mode images, which should be the opposite case. The tips used for contact-mode imaging may have been degraded from previous use. For the samples in Figure 4.6, the total ionic areas were found to be 22% and 48% for N212 and N117, respectively. The highly conducting areas (>70 pA) were found to be 2.5% and 1% of the total area for N212 and N117, respectively. These values are smaller than those found under VOFC conditions in the previous chapter, where ∼17% and ∼6% of the total areas were found to be highly conducting under 0V bias for N212 and N117 samples, respectively. In terms of phase-current correlation, there is obvious correlation between the N212 images in Figures 4.6a and 4.6b, but less so for the N117 images in Figures 4.6c and 4.6d. The same pattern of high phase-current

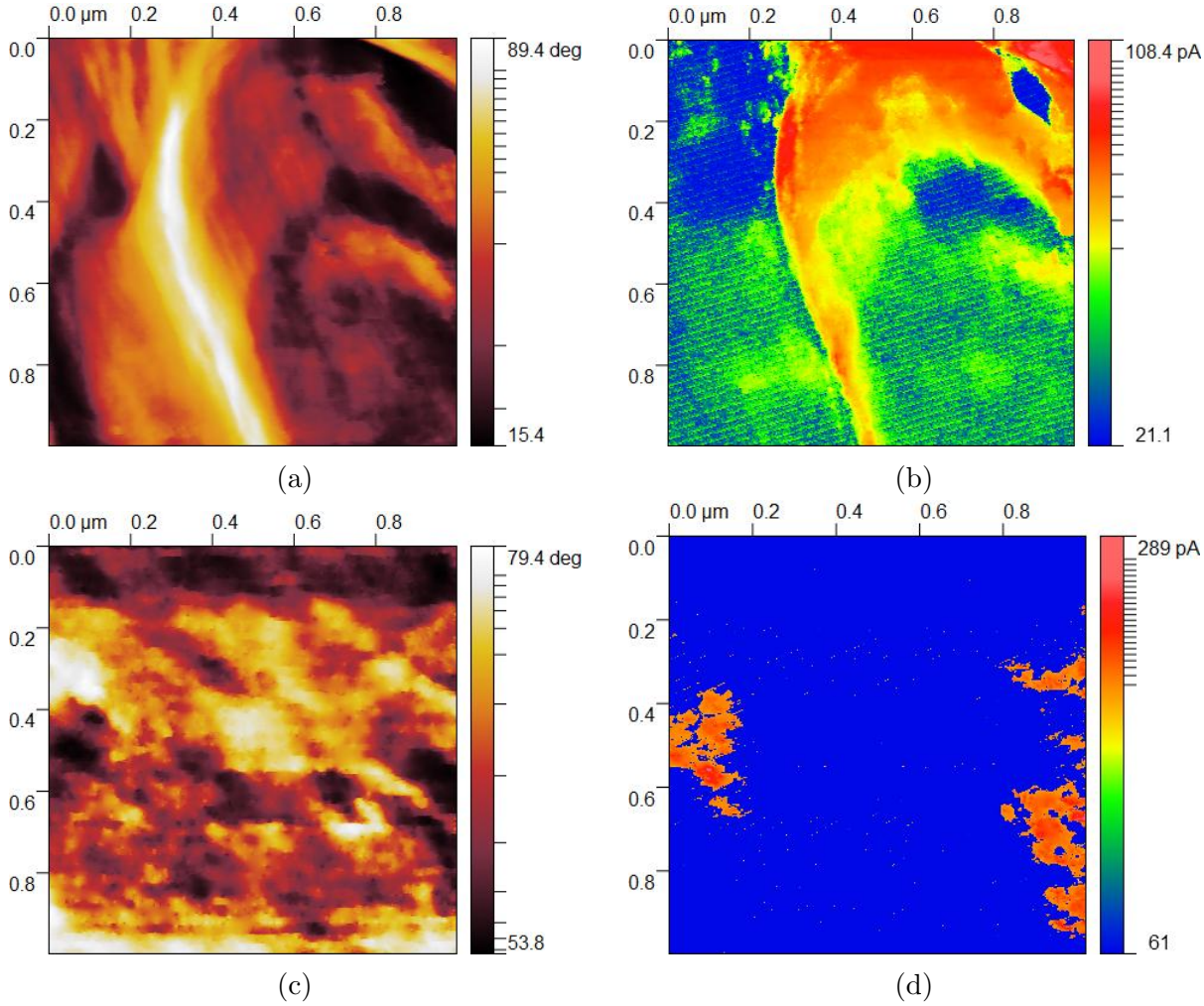

Figure 4.6: 1x1 µm repulsive force regime tapping mode images of Nafion exposed to 1M methanol. (a) N212 phase. (b) N212 current. (c) N117 phase. (d) N117 current.

correlation for N212 as well as low phase-current correlation for N117 in repulsive tapping mode was seen as in the previous chapter (see Figures 3.4 and 3.7).

4.5 Conclusions and Future Work

Bulk, ex situ studies on the conductivity of Nafion under DMFC conditions have shown that moderate current densities on the order several hundred mA cm^{-1} are possible at temperatures over 50 °C[17], which we were unable to corroborate due acquiring our data at 23 °C. Future studies using our novel imaging cell at elevated temperatures will allow for more accurate insight into the nanoscale structure-function of Nafion under true DMFC operating conditions. We found that both N212 and N117 show minimal proton conductivity at room temperature using contact-mode AFM, however we did observe moderate current densities using repulsive tapping mode AFM that corroborated previous findings[34]. As expected, we observed that both N212 and N117 swell when exposed increasing concentrations of methanol, showing a linear relationship between domain feature size and concentration. This work represents only the first steps in establishing a baseline for evaluating the performance and structure-function of polymer electrolyte membranes in the context of DMFCs.

Future work includes studying the effect of anode catalyst loading and composition, which should show a prominent effect on the nanoscale current density. This platform may prove useful in benchmarking new methanol oxidation catalysts against the standard

PtRu catalysts. Other future studies could investigate the nanoscale structure-function of new membranes that have been developed for mitigating methanol crossover by measuring the degree of swelling in phase images.

Appendix A

VRFB Electrolyte Synthesis

A.1 Introduction

The original goal of this thesis project was to study ion conducting polymer membranes in operando within VRFBS using AFM. Thus, we needed to procure or synthesize the vanadium electrolyte to fully simulate the conditions of a VRFB. In its original form as published by its inventor Skylass-Kazacos, the VRFB uses two equimolar aqueous solutions of dissolved vanadium salts and sulfuric acid, with the concentration of vanadium ions being no more than 1.5M and the sulfuric acid between 2 to 3M per solution[110]. Below 2M sulfuric acid concentrations the conductivity of the electrolytes is low enough to negatively affect the performance of VRFB cycling, while greater than 3M sulfuric acid can destabilize the V^{3+} ions in solution, leading to degradation of storage capacity over time[125]. Vanadium ions are kept to no more than 1.5M total concentration due to the instability of the VO_2^+ ions, which above 1.5M will precipitate into V_2O_5 in

solution[89]. Since its inception, there has been many advancements in the formulation of the electrolytes for VRFBs, which have largely overcome the deficiencies of the original formulation, those being low vanadium ion concentrations[89], small operating temperature range[122], and high diffusion coefficients/kinetic barriers at the electrodes[47][25].

As this work breaks new ground into in-operando flow battery membrane research, we opted to use the original electrolyte formulations to be comparable to a wider body of research and to not introduce compounding variables into the study. Thus, we targeted 1.5M total vanadium concentrations and 2.5M total sulfuric acid concentrations for both the anolyte and catholyte used in this study, with no other additives.

V^{2+} ions are unstable in the presence of atmospheric oxygen and will be rapidly oxidized to V^{3+} and VO^{2+}[37], thus we were unable to purchase preprepared anolyte solutions and needed to synthesize them ourselves. In the original VRFB description by Skylass-Kazacos, one of the approaches she and her team used to prepare the electrolytes was dissolving V_2O_5 in dilute sulfuric acid while introducing SO_2 gas as a reducing agent[110]. This would result in a solution of vanadyl sulfate (VO^{2+}) in sulfuric acid. Her team had originally synthesized the electrolytes by dissolving vanadyl sulfate salt in sulfuric acid, however, alternative synthesis routes to produce aqueous vanadyl sulfate such as the one which used V_2O_5 powder were included in the original VRFB patent to overcome the high cost of vanadyl sulfate salt[47]. Most research into VRFB

electrolyte synthesis is focused on lowering the cost by making use of vanadium-rich raw materials such as V_2O_5[82] or V_2O_3 powders[47]. Since our study was focused on the VRFB membrane, we opted to use vanadyl sulfate salt as our source of vanadium, although throughout the synthesis attempts, we explored dissolving V_2O_3 powder as another source of vanadium.

In the next sections, we will overview the different synthesis routes we used along with the results of each attempt, culminating in the final, successful synthesis of V^{2+} electrolyte along with the supporting data. As we will show, obtaining V^{2+} electrolyte was the most difficult step, and various routes failed in producing it.

A.2 Large Volume Glass Electrolytic Cell Route

In our first attempt to produce V^{2+} electrolyte, we acquired a custom glass electrolytic cell, as seen in Figure A.1. The glass compartments each had over 500 mL total volume and were connected via a flange with 50mm inner diameter. Each side was capped with a rubber stopper, with each stopper having a 10mm graphite rod embedded through it along with glass tubing on the anodic side for nitrogen gas. To increase the surface area of each electrode, we added 10x10x0.5cm carbon felt to each side, folding it several times, and pushing the graphite rod through it to make electrical contact. Each side included a magnetic stir bar. For this synthesis, we planned to fill each side with equal volumes of $VOSO_4/H_2SO_4$ and apply a voltage to convert the anodic side from VO^{2+} to V^{3+} and

the cathodic side from VO^{2+} to VO_2^+. We would then replace the cathodic side with fresh VO^{2+} electrolyte and run the cell again, reducing the anodic side from V^{3+} to V^{2+}.

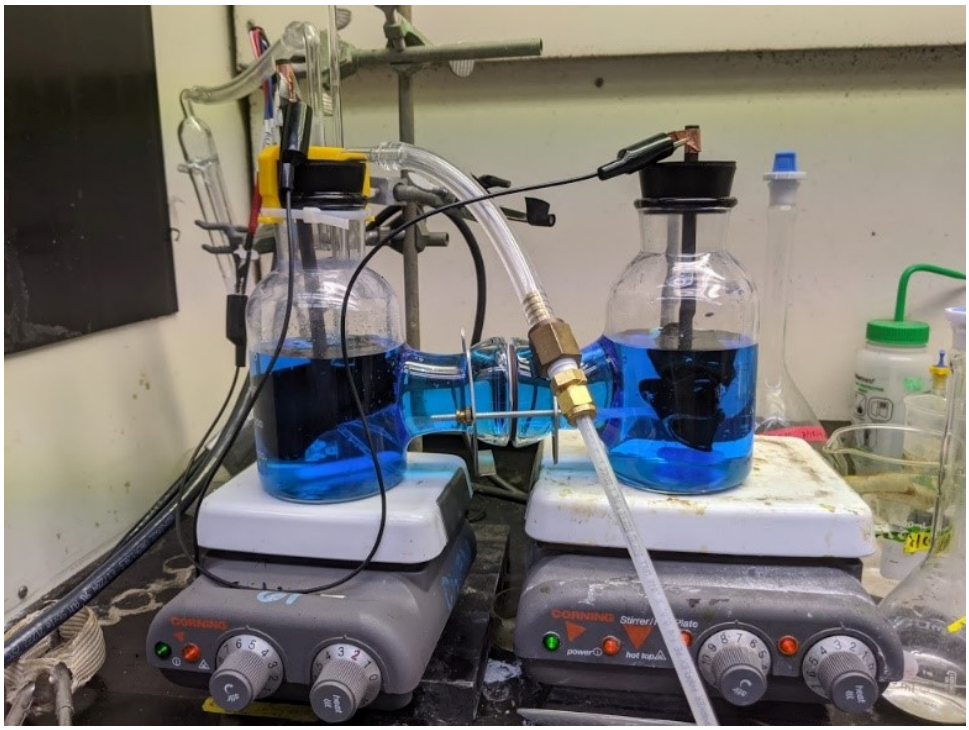

Figure A.1: Photograph of the 1 L total volume glass electrochemical cell, showing the large 50mm diameter flange, the graphite rod electrodes, and the 0.1M $VOSO_4$ electrolyte used.

To begin the process of making V^{2+} electrolyte, we first made 1 L of 0.1M vanadyl sulfate ($VOSO_4$) in 0.2M sulfuric acid (H_2SO_4). Due to the large volume of the solution, we opted to use a lower concentration as making a liter of full concentration electrolyte would consume 244 g of $VOSO_4$. The large size of the cell was chosen to allow for a large flange diameter and thus a large proton exchange membrane area to reduce the cell resistance, and thus the time required for electroreduction of the vanadium ions in the anodic cell. We assembled the electrolytic cell by sandwiching a 5x5cm square of Nafion

212 that had been boiled in 1M H_2SO_4 for 1 hour in preparation, between the cell flanges with gaskets and clamping them together, as shown in Figure A.1. Once assembled, we added 500 mL of $VOSO_4/H_2SO_4$ solution to each side of the cell. Applying Faraday's law:

$$t = \frac{e\ n\ N_a}{I} \tag{A.1}$$

Where t is time in seconds, e is the elementary charge in coulombs, n is the moles of ions in the cell, N_a is Avogadro's number, and I is the current, we theorized that 50 mA of current due to an applied voltage would require 2.23 days to completely convert the 0.1 moles of VO^{2+} ions to V^{3+} and VO_2^+ ions. Before starting the conversion, we attached a hose to the glass tubing on the anodic half of the cell which was connected to a 50L tank of pressurized Nitrogen. We flowed nitrogen through the anodic half of the cell through this hose over the duration of the run. The cell halves were placed atop two magnetic stir plates which were turned on to help evenly distribute the ions in solution. We used a DC power supply (Instek, Taiwan) to apply enough voltage (2.5 V) to the cell until 50 mA of current was observed. This gave a cell resistance of 50 Ω, which was the sum of the electrolyte, Nafion, and electrode resistances. Over time, the resistance of the cell increased, and the current steadily decreased, dropping to 10 mA after the first day. After 5 days, the current had dropped to only a few mA and the cell voltage was turned off. Figure A.2 shows the photos taken of the cell after 5 days, before and after the catholyte (right side) was replaced to restart the cell.

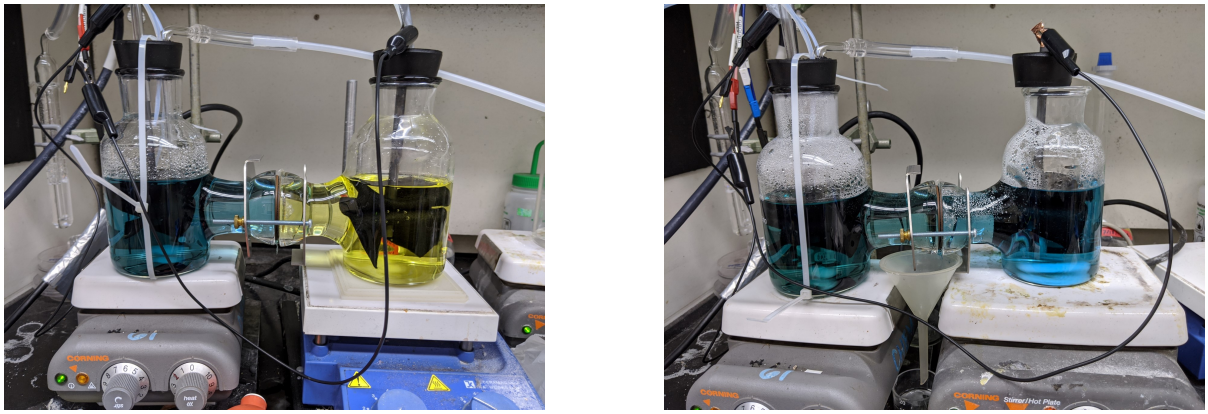

(a) (b)

Figure A.2: (a) Photograph of the large glass electrochemical cell after 24 hours at 2.5V. (b) Photograph of the large glass electrochemical cell once the cathode side was replenished with fresh $VOSO_4$ electrolyte.

After running the cell again for 5 days, it became clear that the conversion from V^{3+} to V^{2+} was not occurring at an observable rate on the anodic side, as the color had not changed from dark green to violet as seen in the photo in Figure A.3. Instead, the cathodic side had remained blue while the anodic side turned to a dark blue color.

Thus, the first attempt at synthesizing V^{2+} electrolyte ended in failure. The process was reevaluated, and the following problems were identified:

- **High Cell Resistance.** Despite using a 50 cm diameter Nafion membrane, the cell suffered from high resistance which was due to both the low concentration of sulfuric acid and the high contact resistance between the carbon felt electrodes and the graphite rods.

- **Large Volume.** Due to needing an entire liter of electrolyte, it was prohibitively

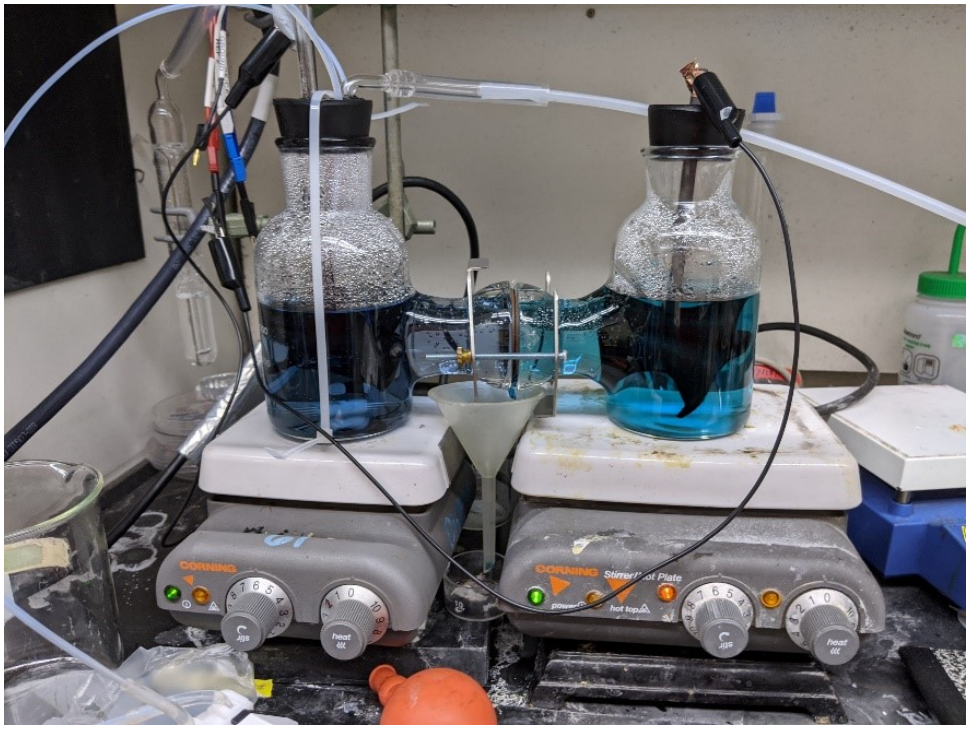

Figure A.3: Photograph of the large glass electrochemical cell after 48 hours post-cathode side replenishment.

costly to fill the cell with fully concentrated electrolyte. Using diluted electrolyte reduced the conductivity of the electrolyte.

- **Air Infiltration.** After the failure of the synthesis, we turned off the nitrogen gas to the anodic side and over the course of a few hours the solution was oxidized until it was back to the original color it had after the first run. While ion crossover through the membrane most likely contributed to this, the color of the cathode side remained unchanged during this process, which led us to believe that air was leaking into the cell.

Two new approaches were put into place for the next attempts we made at synthesizing V^{2+} electrolyte. These were:

- Using a separate flow cell stack to perform the electrochemical reactions instead of one connected glass cell. We reasoned that having this would lower the cell resistance and decrease the time for conversion.

- Sourcing the vanadium from V_2O_3 powder, as this would, in theory, allow us to begin the process starting with V^{3+} electrolyte. This would save us the step of first converting VO^{2+} electrolyte into V^{3+} electrolyte.

A.3 Sourcing Vanadium Ions from V_2O_3

To make V^{2+} electrolyte, we planned to dissolve V_2O_3 powder in degassed sulfuric acid, according to the following reaction:

$$V_2O_3 + 3H_2SO_4 \rightarrow V_2(SO_4)_3 + 3H_2O \tag{A.2}$$

We planned to have the final concentration of V^{3+} be 1.5M and the final concentration of H_2SO_4 be 2.5M, with a final volume of 50 mL. Thus, we first degassed 50 mL of 7M H_2SO_4 (made by diluting concentrated H_2SO_4 in DI water) with nitrogen for 1 hour. Once degassed, we transferred the acid to a two-neck round-bottom flask, with one neck connected to a reflux condenser and the other to a hose connected to a tank of nitrogen. The entire assembly was held over a hot plate set to 80 °C. We weighed 5g of V_2O_3 powder into the flask and connected the top of the condenser to a bubbler filled with mineral oil. Finally, we turned on the nitrogen flow to the setup as well as the water flow through the condenser. This was allowed to reflux overnight. The setup is shown in

Figure A.4.

Figure A.4: Photograph of the reflux setup to dissolve 5g of V_2O_3 powder in 7M H_2SO_4 under flowing nitrogen.

Once cooled, we filtered the dark green liquid from the flask through filter paper into a polypropylene bottle for storage under nitrogen inside of a glove bag. Unfortunately, there was a mixture of orange and black powder caught on the filter paper, which meant that the final concentration of V^{3+} and H_2SO_4 in the solution was unknown.

A.4 Total Vanadium Ion Analysis

To determine the actual concentration of vanadium and acid in the solution, we took six 2mL aliquots using a volumetric pipet for analysis. We diluted half of these aliquots in DI water to 50 mL using volumetric flasks. We stirred all six samples using magnetic stirring while exposed to air for 1 hour each to allow all the V^{3+} ions to oxidize to VO^{2+} ions.

To determine the concentration of vanadium in our synthesized electrolyte, we first standardized a 0.1M solution of $KMnO_4$ using oxalic acid. The $KMnO_4$ solution was made by dissolving 0.15g of KMnO4 powder in DI water using a 50 mL volumetric flask. A 0.1M solution of oxalic acid was made by dissolving 0.45g into 2M sulfuric acid in a 50 mL volumetric flask. We used a 50 mL burette to titrate 10 mL of the oxalic acid solution with our $KMnO_4$ titrant, which gave us the actual concentration of $KMnO_4$: 0.016M. The titration equivalence point was determined visually by noting the point when a slight reddish color persisted after 5 minutes of stirring the sample.

Having standardized the $KMnO_4$ solution, we took three of the vanadium electrolyte samples and titrated them visually, observing a color change from green during the titration to yellow at the equivalence point, as seen in Figure A.5.

The average concentration of the three samples was found to be 1.38M total vanadium, which was less than the target of 1.5M. This was due to the incomplete dissolution of the V_2O_3 powder.

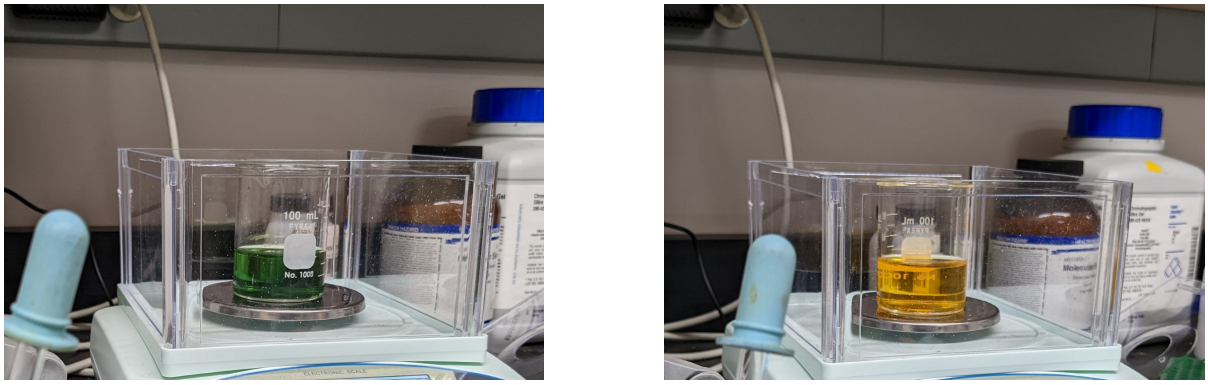

(a) (b)

Figure A.5: Photographs of the V_2O_3-sourced electrolyte sample (a) before and (b) at the equivalence point during the titration with KMnO4.

A.5 Total Sulfate Analysis

To determine the concentration of H_2SO_4 in our electrolyte, we performed a total sulfate analysis based on the work of Noriega Oreiro et al, who showed that the total moles of sulfate in solution can be determined with high precision (0.7%) by measuring the density of a sample of vanadium electrolyte before and after adding a solution of 0.5 M $BaCl_2$ of known density[91]. She and her colleagues determined that the moles of sulfate $n_{SO_4^{2-}}$ in a sample can be calculated using the following formula:

$$n_{SO_4^{2-}} = \frac{V_{BaCl_2} \times (\rho_{BaCl_2} - \rho_{Supernatant}) + V_{Sample} \times (\rho_{Sample} - \rho_{Supernatant})}{MW_{BaSO_4} \times (1 - \frac{\rho_{Supernatant}}{\rho_{BaSO_4}}) + \rho_{Supernatant} \times \Delta V} \tag{A.3}$$

Where V represents volume in mL, ρ represents density in g mL^{-1}, MW represents molecular weight, and ΔV represents a calibration factor determined to be 21.5 mL mol^{-1} by the authors. A 100 mL solution of 0.5M $BaCl_2$ was made by dissolving 11.669 g of $BaCl_2$ powder in a volumetric flask with DI water. By subtracting the mass of the

dry volumetric flask from the flask with the $BaCl_2$ solution, we determined the density (ρ_{BaCl_2}) of the $BaCl_2$ solution. We used the same volumetric flask technique to measure the density of the vanadium electrolyte samples and subsequent liquids. We measured 12 mL of 0.5M $BaCl_2$ solution to each of the three undiluted electrolyte samples by weight using the density of the $BaCl_2$ solution. Figure A.6a depicts the samples before and after of the addition of $BaCl_2$ solution. The samples were allowed to settle for 24 hours before further analysis, as seen in Figure A.6b.

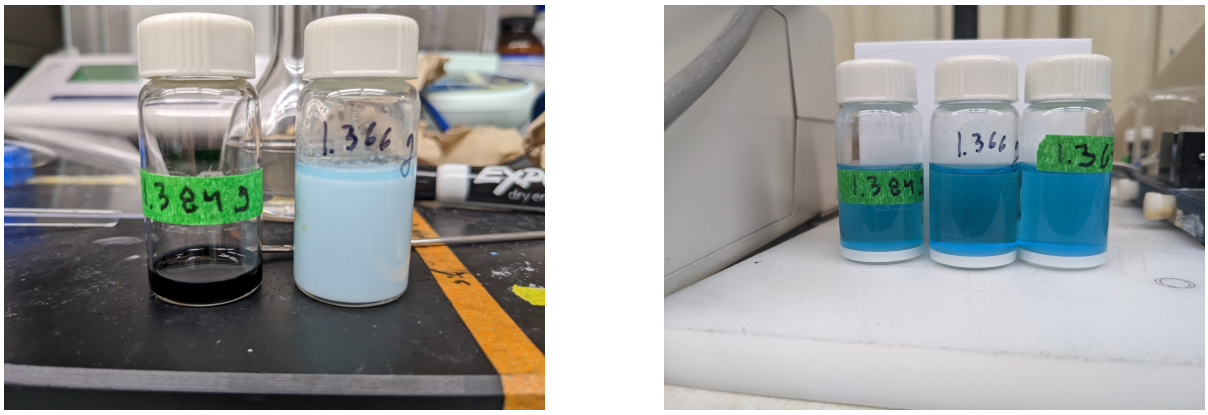

(a) (b)

Figure A.6: (a) Photograph of the V_2O_3-sourced electrolyte samples before and after the addition of 0.5M $BaCl_2$ solution. (b) Photograph of the V_2O_3-sourced samples after 24 hours with $BaSO_4$ precipitated out of solution.

The density of the supernatant was measured by weighing 5 mL from each sample dosed into a tared beaker using a volumetric pipette. Using Equation A.3, we calculated that the vanadium electrolyte samples contained 3.78M total sulfate on average. Subtracting the concentration of vanadium found through KMnO4 titration, this yielded a 2.45M sulfuric acid concentration for the synthesized vanadium electrolyte.

A.6 Revised Electrochemical Cell

We went through the process of fabricating 2 separate flow battery-type electrochemical cells which had very small volumes in relation to the electrode and membrane areas, with each shown in Figure A.7.

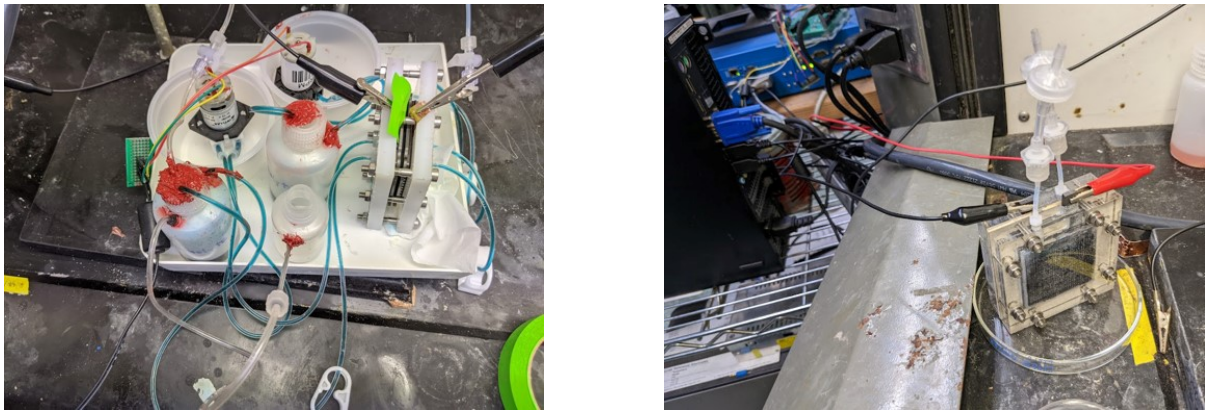

(a) (b)

Figure A.7: (a) Photograph of a single cell flow battery stack with peristaltic pumps and electrolyte reservoirs. (b) Photograph of a single cell stack with no peristaltic pumps or electrolyte reservoirs.

The goal in making these cells was to overcome the high ohmic resistance of the original larger glass cell. Both cells had flaws, namely:

- **Leaks:** due to needing external reservoirs, the first flow battery cell (Figure A.7a) suffered from air leaking into the anodic side and oxidizing the V^{2+} ions.

- **Low volume:** we removed the external reservoirs in the second design (Figure

A.7b), which meant we could only attempt to create 3-4 mL of V^{2+} electrolyte at a time.

- **Corrosion:** due to the highly corrosive electrolyte, pumps and connectors would degrade over time for both cells.

Thus, we opted to return to the original glass cell design with a few modifications, those being:

- **Smaller size:** we reduced the volume of the glass cell halves from 500 mL to 50 mL.
- **3D printing:** we 3D printed the clamp holding the cell halves together (see Figure A.8) and the caps for each half out of polypropylene, a thermoplastic that can withstand the corrosive environment.

The newly designed glass cell is shown in Figure A.8. This cell had the advantages of the original glass cell: fewer connections for leaks to occur, simple design, and high corrosion resistance.

A.6.1 Using the Revised Electrochemical Cell to Synthesize V^{2+} Electrolyte

Using the 1.38M $V^{\sim 3+}$ electrolyte synthesized from V_2O_3 and the redesigned small glass electrochemical cell, we again attempted to reduce the valency of the vanadium in the electrolyte down to V^{2+}. The cell was first partially assembled by clamping a prepared

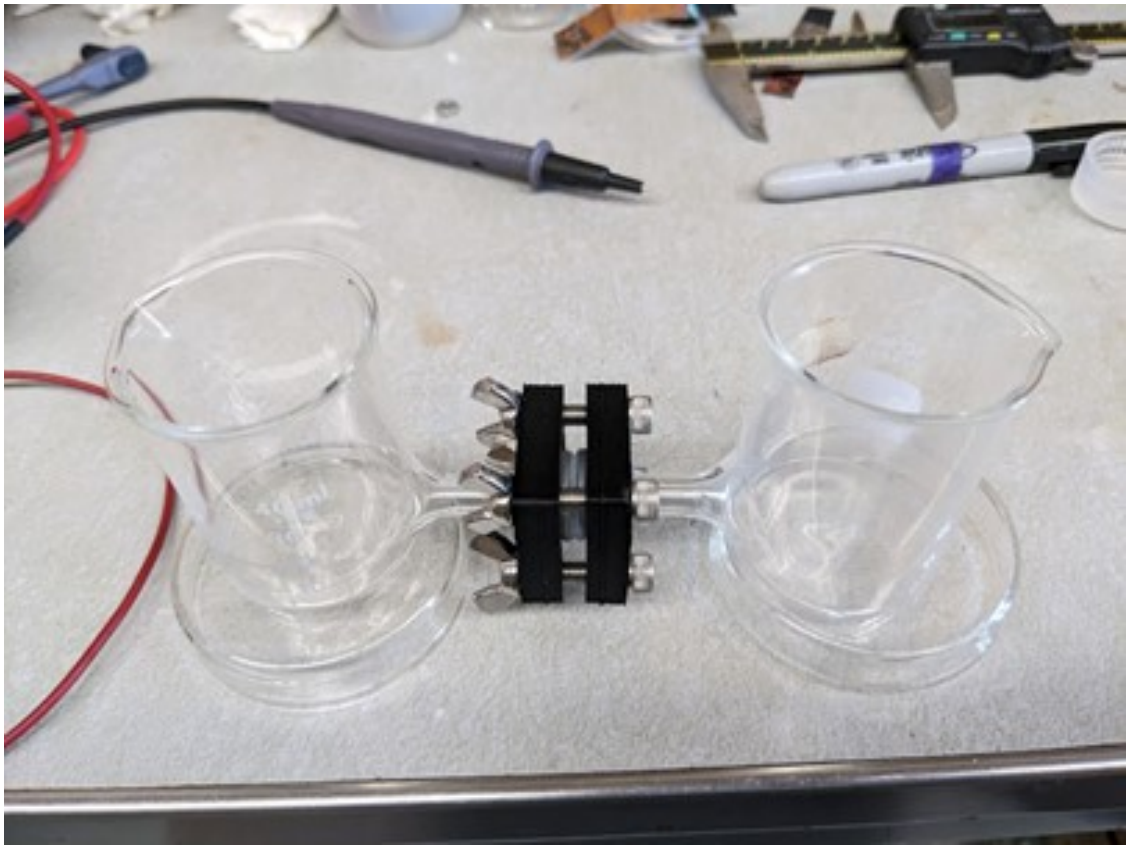

Figure A.8: Photograph of the redesigned glass electrochemical cell with a 3D-printed polypropylene clamp to hold the flanges together.

10mm diameter Nafion 117 membrane between the two halves of the cell using the 3D printed clamp, as shown in Figure A.8.

Equal volumes of the V_2O_3-sourced electrolyte were placed in the cell halves inside of a glove bag filled with nitrogen. Stir bars were added and the cell halves were closed with the 3D printed caps which had graphite electrodes embedded within each of them. Finally, the cell was connected to a DC power supply and the ran for 24 hours at +4V while stirring each side with custom magnetic stir plates, as seen in Figure A.9.

Figure A.9: Photograph of the fully assembled redesigned glass electrochemical cell, with both sides filled with electrolyte and with custom-built DC-motor magnetic stirrer plates..

(a) (b)

Figure A.10: (a) Photograph of the small glass cell at the end of the V^{2+} electrosynthesis. (b) Photograph of the extraction of the finished product under nitrogen in a glove bag.

After 24 hours, the anode side had turned a dark green color, while the cathode side had turned a dark yellow color. At this point we replaced the cathode side with fresh electrolyte and applied +4V for another 24 hours. The cell at the final stage is depicted in Figure A.10a, with the dark yellow cathode side and the violet anode side visible. We disassembled the cell inside the glove bag under nitrogen and stored the anodic vanadium electrolyte in a sealed plastic container. We diluted 1 mL of the anodic electrolyte to 25 mL using a volumetric pipette and a volumetric flask, as seen in Figure A.10b. ∼5 mL of this solution was transferred to a threaded glass 1x1cm cuvette and sealed while still inside the glove bag under nitrogen.

Spectrophotometric Analysis of the V^{2+} Electrolyte

To confirm that we had produced the V^{2+} electrolyte, we acquired absorbance spectra of our electrochemical cell anodic product and 5 mL of a 1:25 diluted sample of our V_2O_3-

sourced electrolyte which we had allowed to be oxidized by air by stirring for an hour on a stir plate. We used an Ocean Optics USB4000 spectrophotometer with a tungsten-deuterium lamp and a 1cm pathlength. The samples and their spectra are depicted in Figure A.11, with the characteristic peaks for V^{2+} (567 nm) and VO^{2+} (760 nm) marked on the chart in Figure A.11b.

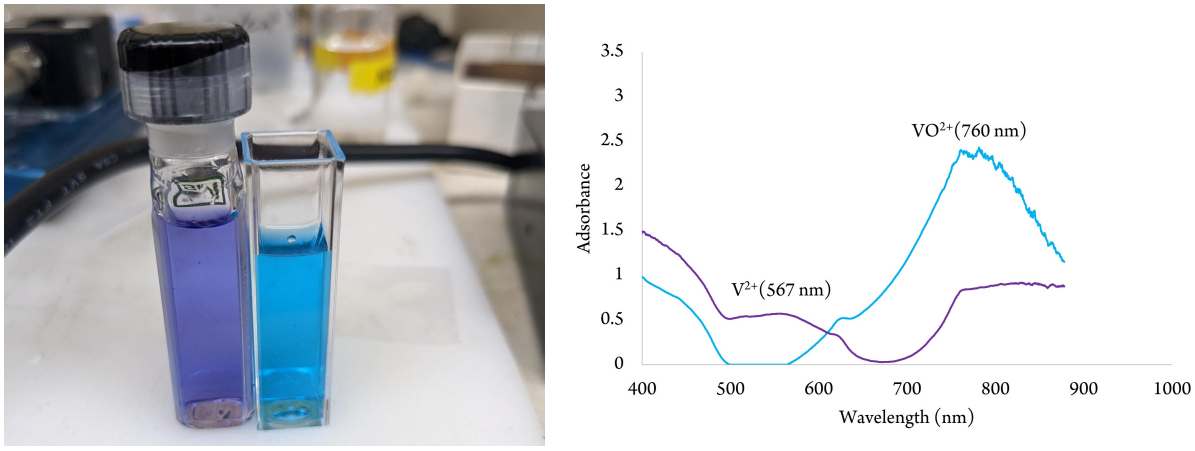

(a) (b)

Figure A.11: (a) Photograph of the finished V^{2+} electrolyte sample and the V_2O_3-sourced electrolyte from which it was made, each diluted by 1:25. (b) Spectra of the samples in (a), showing the absorbance typical of V^{2+} (violet) at 567 nm and VO^{2+} (blue) at 760 nm.

A.7 Conclusion

Despite several setbacks, we eventually succeeded in synthesizing 1.38M V^{2+} in 2.45M H_2SO_4 electrolyte using a starting electrolyte sourced from V_2O_3 powder which was then reduced using a custom-made and partially 3D-printed electrochemical cell. We performed analytical techniques to determine the concentrations of dissolved vanadium

and total sulfate and used spectrophotometry to confirm the presence of the V^{2+} ions in the final product. In the future, using $VOSO_4$ as the source of dissolved vanadium would remove the need to for titrimetric and densitometric analyses as there would be no vanadium/sulfuric acid lost in the synthesis compared to using V_2O_3 powder.

Appendix B

DFT Study of Methanol on VO/TiO_2

B.1 Introduction

Our research group has studied the catalytic activity of soft-landed VO_x clusters on rutile TiO_2 (r-TiO_2) using combined mass spectrometry (MS), ultra-high vacuum scanning tunneling microscopy (UHV-STM), and temperature-programmed desorption (TPD)[97][117][101]. The aim of these studies is to understand the catalytic behavior of these materials at the atomic level, and my contribution to this effort was, in part of a collaboration with other researchers, conducting plane-wave basis density functional theory (DFT) with Hubbard corrections to help elucidate the most energetically favorable reaction pathways for the oxidative dehydration of methanol to formaldehyde on both bare r-TiO_2(110) and VO-

modified r-TiO_2(110) surfaces. These catalysts have been shown to be active towards methanol oxidation to formaldehyde and water[8][101], and our group has shown this to be true using mass/charge (m/z) selected TPD spectra as seen in Figure B.1.

In these spectra, we can see peaks associated with the thermal desorption of both methanol (m/z:31, black) and formaldehyde (m/z:29, green) from both VO/TiO_2 (B.1a) and bare TiO_2 (B.1b) at ∼375K (R_1), ∼480K (R_2), ∼625K (D5c-Ti) and at ∼660K (D_{VO}), with formaldehyde being favored at higher temperatures on both surfaces. For the bare TiO_2, the reaction has been shown to occur at the 5-fold coordination Ti sites (5c-Ti). These results were found as part of a study covered in previous experimental research[101]. It is this disproportionate amount of formaldehyde at elevated temperatures that we wanted to investigate using DFT to better understand the most likely reaction pathways from a kinetic standpoint. The systems we modeled were idealized surfaces free from defects which are known to contribute to catalytic activity, which is discussed in later sections.

Hubbard-corrected density functional theory (DFT+U) is an extension of conventional DFT that incorporates a correction for the coulomb repulsion in transition metal d electrons, which is crucial when simulating catalytic reaction pathways involving the 3-d electrons present in VO/TiO_2, as it helps to address the limitations of standard DFT in simulating strongly correlated electronic systems[53]. By accounting for the localized

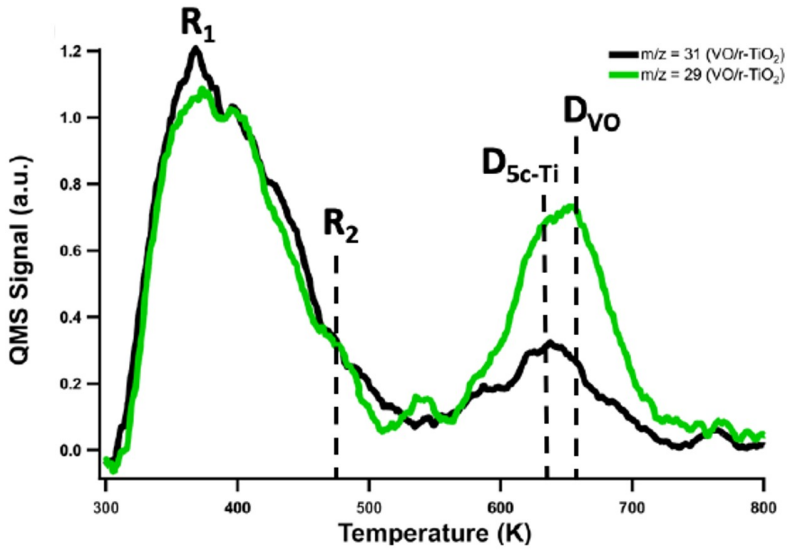

(a)

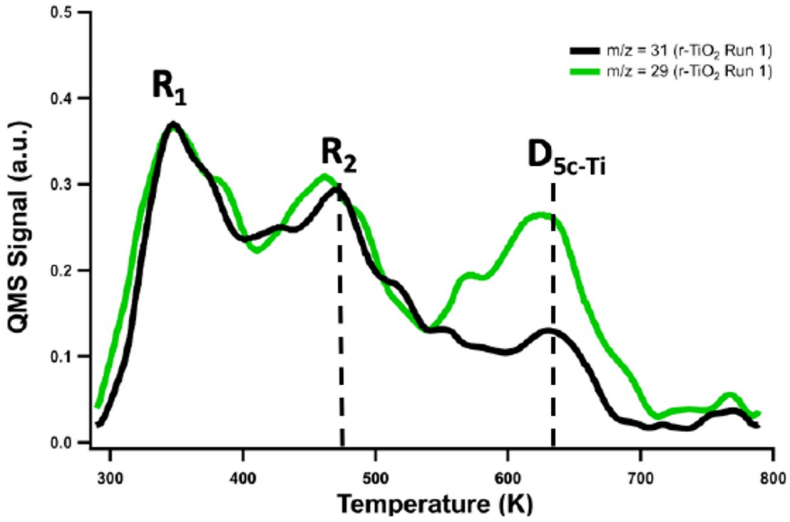

(b)

Figure B.1: TPD spectra of (a) soft-landed VO on r-TiO_2 and (b) bare r-TiO_2 after exposure to 100 Langmuir (L) of methanol showing the mass-to-charge (m/z) signals of methanol (black) and formaldehyde (green)

nature of d electron interactions through the Hubbard correction, this method provides a more accurate description of electronic properties and energetics in catalytically active sites. Using this tool, we simulated the interaction of methanol with bare TiO_2 and VO-modified TiO_2 and uncover likely reaction pathways and intermediate configurations to help better explain the experimental results obtained from the TPD spectra.

B.2 Methods

All the calculations were performed with density functional theory (DFT) using the PBE functional1 and the D3 van der Waals correction[45] to approximate exchange-correlation effects. In addition, DFT+U corrections of 4 eV and 3.5 eV are applied to vanadium and titanium d-states, respectively[39]. The calculations were performed in the plane-wave program Vienna Ab-Initio Simulation Package (VASP)[68]. The projector-augmented wave (PAW) approach[69][15] were used for the core electron representation and a plane wave basis set with an energy cutoff of 400 eV was used to represent wavefunctions and the electron density[121]. Reciprocal space was sampled using $2\times2\times1$ k-points due to relative large size of the supercell. The geometry and volume of bulk r-TiO_2 was optimized and subsequently cut to expose the (110) surface with a slab thickness of four TiO_2 tri-layers. A neutral vanadium oxide cluster (V(II)O) is placed in the previously found most energetically favorable position, the three-fold coordinated surface titanium hollow site[107] shown in the Figure B.2 inset. The electronic configuration of the VO/TiO_2

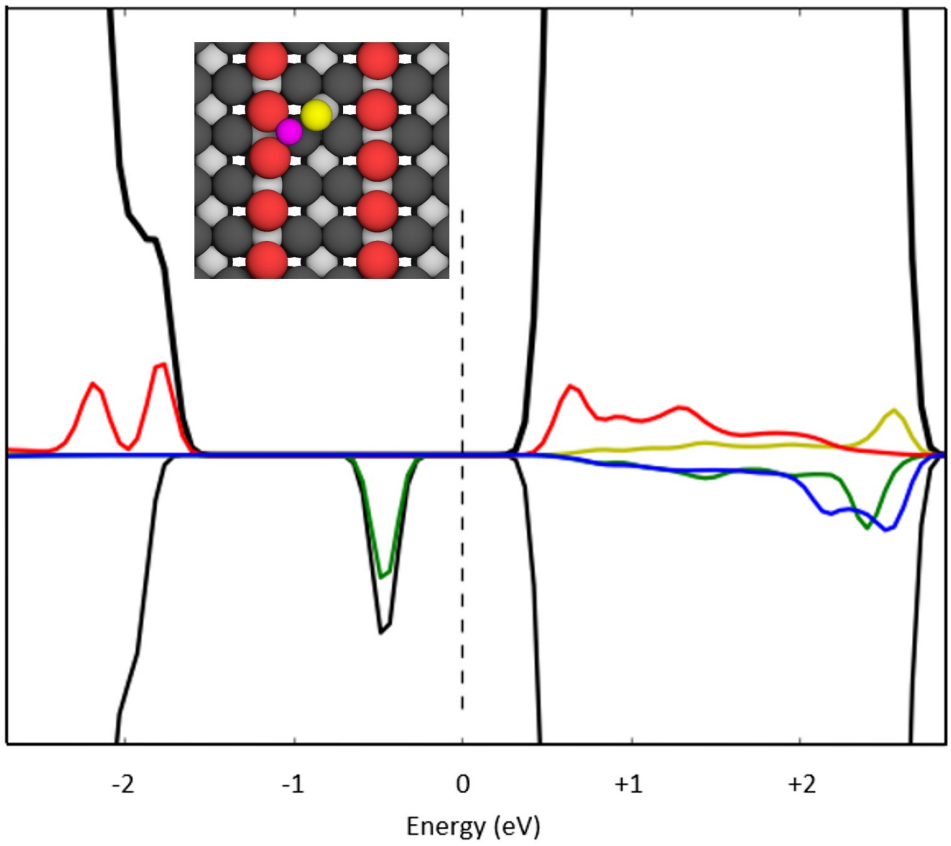

Figure B.2: Density of States (DOS) plot of VO on TiO_2(110). The DOS was extracted from VASP after relaxation. Vanadium d-states are plotted in red (spin up) and blue (spin down). The reduced 3rd tri-layer titanium atomic d-states are plotted in yellow (spin up) and green (spin down). Inset: Top-down view of VO/TiO_2 system showing V atom (purple), vanadyl O atom (yellow), surface O_{br} atoms (red), and bulk r-TiO_2 (gray).

system is illustrated by the projected density of states plot (Figure B.2). The V atom has transferred a spin down electron to a Ti atom in the slab making a Ti^{3+} polaron and a localized Ti d-state situated in the band gap at -0.5 eV. The V atom becomes V^{3+} and the two remaining d-electrons align in a triplet spin-up configuration situated at the top of the valence band (the states shown in red at $\sim$-2 eV). We did not calculate the energies of having the Ti^{3+} polaron situated on different Ti atoms. Instead, we made sure that

the electron localized on a Ti atom in the 3rd TiO_2 tri-layer, which was previously found to be an energetically favorable location for the Ti^{3+} polaron[26].

B.3 Results and Discussion

B.3.1 Methanol Surface Adsorption

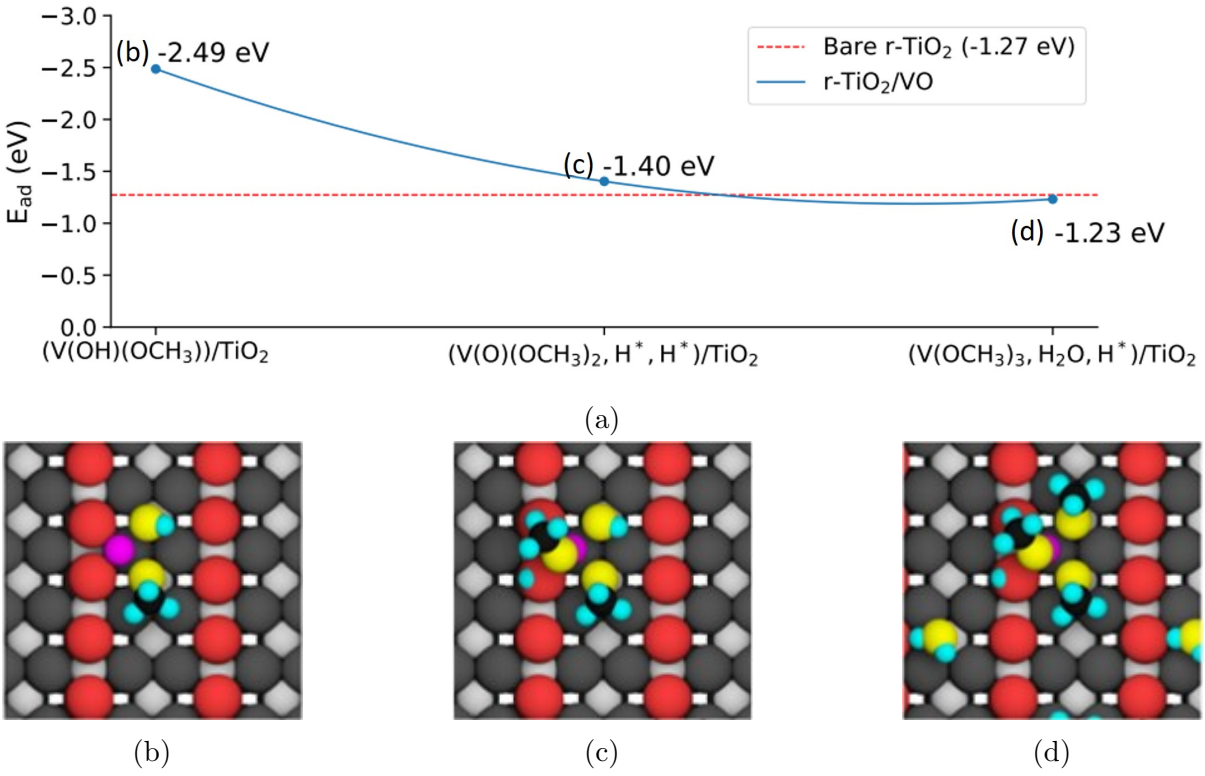

Figure B.3: (a) (Blue) plot of differential adsorption energies vs the number of adsorbed methanol molecules to the VO-(OCH_3)n complex. (Red) methanol adsorption energy on bare TiO_2(100). (b), (c), (d); Top down views of surfaces with one, two and three adsorbed methanol on the VO cluster. Vanadium (purple), O_{br} (red), vanadyl and methanol oxygen (yellow), hydrogen (blue), and the bulk surface (gray).

Using the VO/TiO_2 supercell, the formation of a VO-(OCH_3)n complex was inves-

tigated by sequentially adding methanol to the VO cluster in VASP and letting each structure relax. It has been shown that methanol readily dissociates to methoxide on TiO_2(110)[101], so after each methanol addition, several conformations with the hydroxyls placed on different O atoms were investigated until the most stable conformation was found. Figure B.3 shows the adsorption energy for the lowest energy conformers of VO-(OCH_3)n where n=1 and 2. The adsorption energy was calculated using the following:

$$E_{Adsorption} = E_{Complex} - E_{Surface} - E_{Gas} \tag{B.1}$$

The most stable pathway to n=3 involves creating water from the vanadyl oxygen and desorbed protons from the two adsorbed methoxides. Without this water formation step, the VO cluster is sterically hindered from binding to more than two methoxides. The adsorption energy of methanol on bare TiO_2(110) was used to benchmark the adsorption energies of each sequential methoxide to the VO-(OCH_3)n complex. We find that dissociative adsorption of one and two methanol molecules at the VO cluster is more favorable than adsorption on the bare TiO_2(110) surface, whereas adsorption of the third methanol (via water formation) is +0.07 eV less stable. In the absence of large kinetic barriers, we therefore expect that at least two methanol molecules will dissociatively adsorb on each VO cluster. Under the idealized case where there are no surface defects, some VO clusters may adsorb a third methanol molecule and release a water molecule, since the energy is close to methanol adsorption on bare TiO_2(100).

B.3.2 Methanol Oxidative Dehydration to Formaldehyde

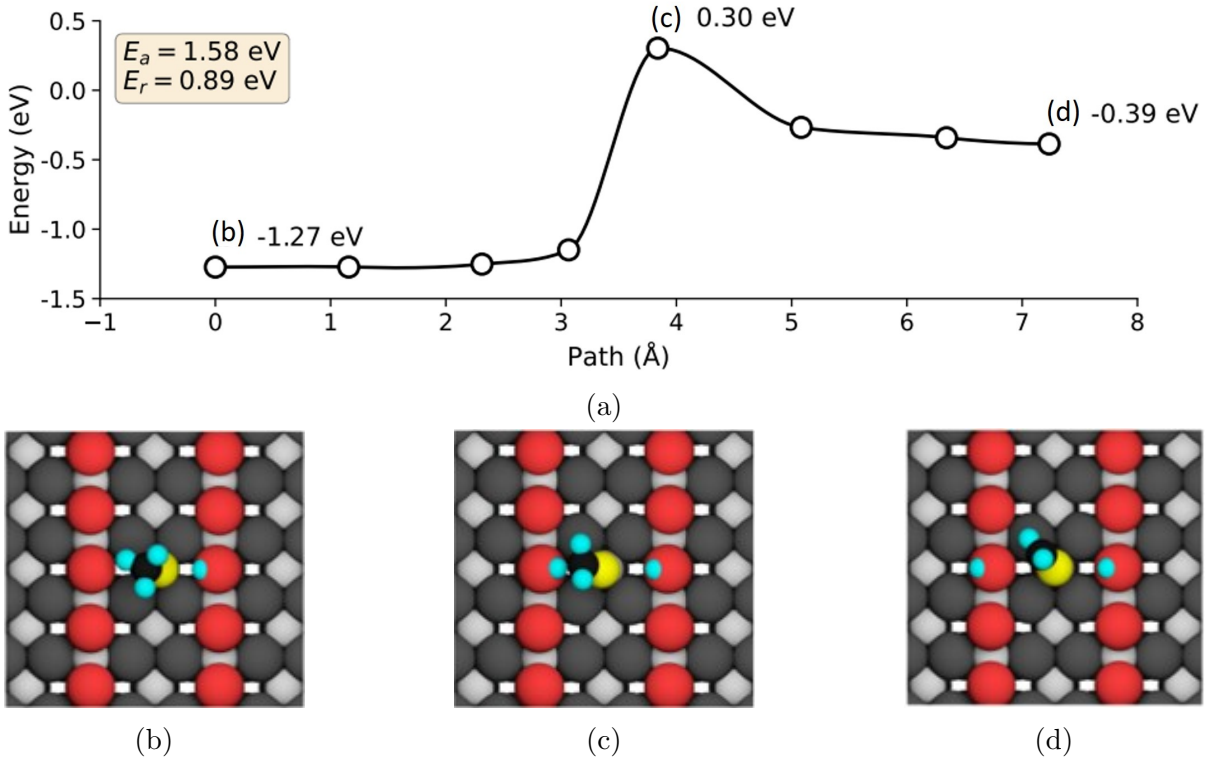

Figure B.4: (a) Plot of reaction snapshot energies in eV vs reaction pathway in angstroms (Å). (b), (c), (d). Top down views of snapshots with Obr (red), methanol/formaldehyde oxygen (yellow), hydrogen (blue), and the bulk surface (gray).

For comparison, we modeled the oxidative dehydration (OD) reaction of methanol to formaldehyde on the bare TiO_2(110) surface using the Climbing Nudged Elastic Band (CNEB) method in VASP[48]. CNEB is useful for finding saddle points and minimum energy pathways in the reaction landscape. Several "snapshots" in time are used as points along the reaction pathway. VASP takes the highest energy image and maximizes its energy along the band, thus when it is converged it will be the exact saddle point. Figure B.4 shows snapshots of a possible OD reaction pathway in which a methoxide bound to a

5c-Ti undergoes OD with a bridging oxygen to form a hydroxyl and formaldehyde. This reaction was estimated using the relaxed transition state energy to have an activation barrier of 1.58 eV.

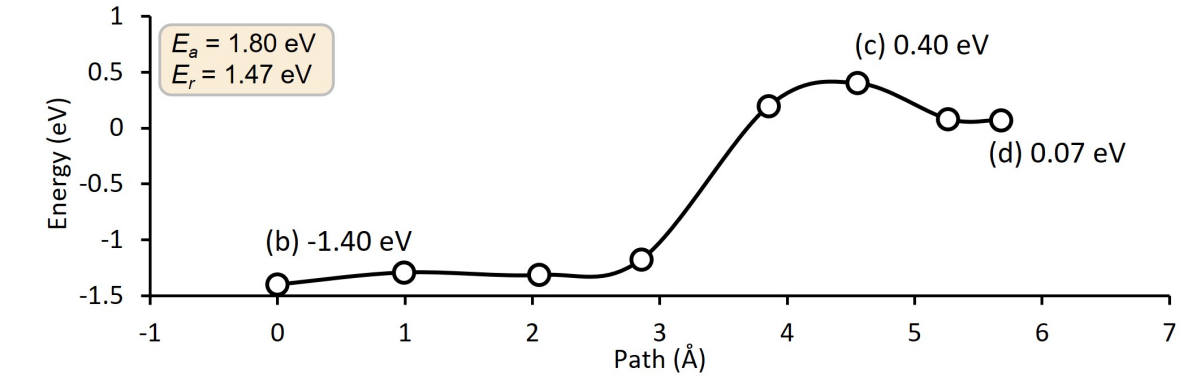

(a)

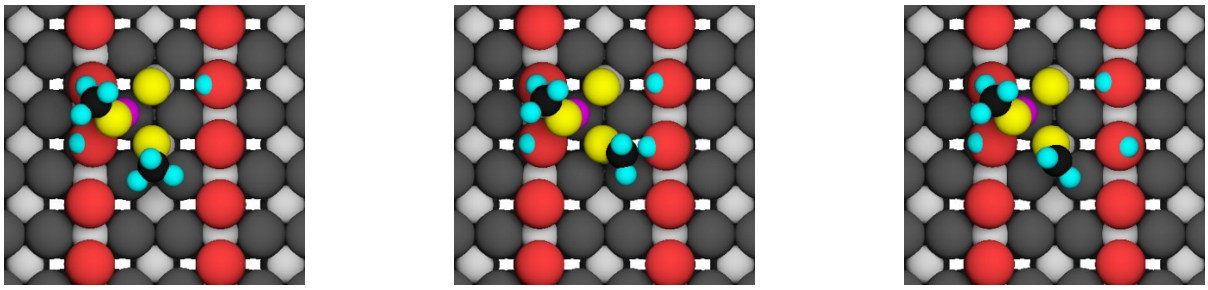

(b) (c) (d)

Figure B.5: (a) Plot of reaction snapshot energies in eV vs reaction pathway in Å for OD with VO-$(OCH_3)_2$. (b), (c), (d): Top down views of snapshots with vanadium (purple), O_{br} (red), vanadyl and methanol/formaldehyde oxygen (yellow), hydrogen (blue), and the bulk surface (gray).

Figure B.5 shows snapshots of a possible OD reaction pathway in which one of the methoxides bound to the VO-$(OCH_3)_2$ complex undergoes OD with a bridging oxygen to form a hydroxyl and formaldehyde. This reaction was estimated to have an activation barrier of 1.8 eV. The TPD data in Figure B.1a shows that when the VO decorated sur-

face is flashed to the bare rutile disproportionation temperature (660K), formaldehyde is detected. Using the Eyring equation[38] to estimate a ∼0.25 eV reaction barrier increase per 100 K increase in temperature of the surface, the calculated oxidative dehydrogenation would occur at ∼720 K. This assumes that the reaction rate doubles per increase in temperature by 10K. Importantly, the OD pathway on bare r-TiO_2 has a 0.32 eV smaller reaction barrier than VO/TiO_2 which is in qualitative agreement with the spectra, which shows a lower disproportionation temperature (D5c-Ti peak) than VO/TiO_2 (D_{VO}).

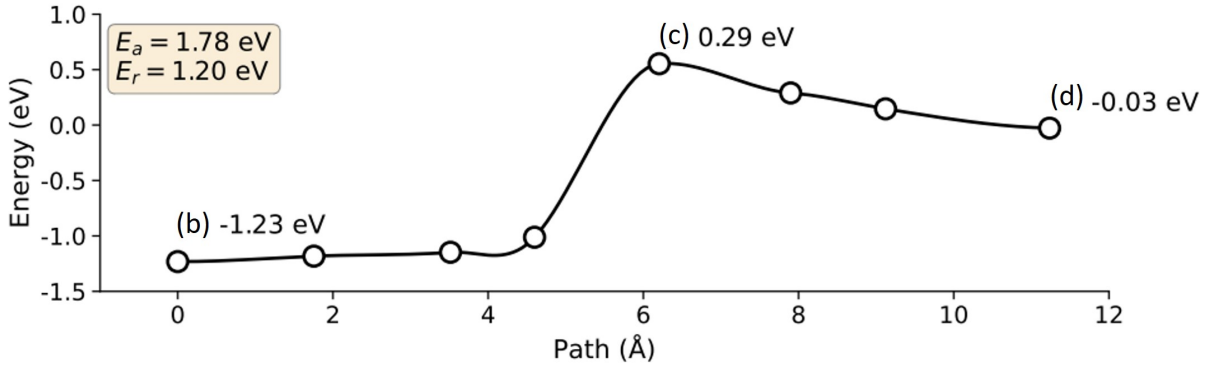

(a)

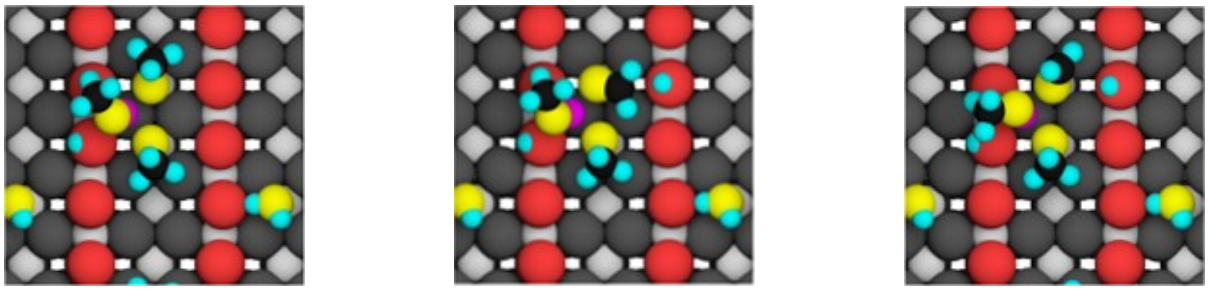

(b) (c) (d)

Figure B.6: (a) Plot of reaction snapshot energies in eV vs reaction pathway in Å for OD with VO-$(OCH_3)_3$. (b), (c), (d): Top down views of snapshots with vanadium (purple), O_{br} (red), vanadyl and methanol/formaldehyde oxygen (yellow), hydrogen (blue), and the bulk surface (gray).

In UHV-STM data it was observed that the VO-$(OCH_3)_3$ complex would form after exposure to methanol, despite the lower adsorption energy compared to bare r-TiO_2[101]. Thus, we performed CNEB calculations to determine the reaction barrier for the OD pathway with a VO-$(OCH_3)_3$ complex, seen in Figure B.6. We found that the energy barrier for this pathway was 1.78 eV, slightly lower than for the n=2 complex. This aligns slightly better with the TPD spectra, which if using the Eyring equation estimation, would correspond to a disproportionation temperature of $\sim$712K.

B.4 Conclusion

The results we obtain qualitatively match those found in the TPD spectra, showing that the OD reaction occurs at a lower activation energy on bare r-TiO_2 than VO/TiO_2, and that the n=3 complex formation is a likely step in the formation of formaldehyde on the VO/TiO_2 surface. This shows that this method could be used to further elucidate the proposed disproportionation pathways.

Our investigations did not consider surface defects such as oxygen vacancies, which are known to be highly chemically active Lewis acid sites for catalysis on bare r-TiO_2[70]. Furthermore, we used neutral VO instead of the ion-sourced VO^+ in the UHV-STM experimental work[101]. The absence of these features in our studies may explain the discrepancy between the activation barriers found using DFT and the measured TPD

disproportionation onset temperatures. Future work involving oxygen vacancies and water formation from surface hydroxyl groups of O_{br} atoms may provide more accurate reaction pathways. Water was not detected in the experiment which produced the spectra in Figure B.1, which points to oxygen vacancies playing an important role in reducing steric hindrance of VO clusters to allows n=3 clusters to form more easily.

Bibliography

[1] Qaisar Abbas, Mojtaba Mirzaeian, Michael R.C. Hunt, Peter Hall, and Rizwan Raza. Current state and future prospects for electrochemical energy storage and conversion systems. 13:5847, November 2020.

[2] Abed M. Affoune, Akifumi Yamada, and Minoru Umeda. Surface observation of solvent-impregnated nafion membrane with atomic force microscopy. *Langmuir*, 20(17):6965–6968, July 2004.

[3] Abed M Affoune, Akifumi Yamada, and Minoru Umeda. Conductivity and surface morphology of nafion membrane in water and alcohol environments. *Journal of power sources*, 148:9–17, 2005.

[4] Elena Aleksandrova, Renate Hiesgen, K Andreas Friedrich, and Emil Roduner. Electrochemical atomic force microscopy study of proton conductivity in a nafion membrane. *Physical Chemistry Chemical Physics*, 9(21):2735–2743, 2007.

[5] Piergiorgio Alotto, Massimo Guarnieri, and Federico Moro. Redox flow batteries for the storage of renewable energy: A review. *Renewable and Sustainable Energy Reviews*, 29:325–335, January 2014.

[6] Mathew Aneke and Meihong Wang. Energy storage technologies and real life applications–a state of the art review. *Applied Energy*, 179:350–377, 2016.

[7] E. Antolini and E.R. Gonzalez. Alkaline direct alcohol fuel cells. *Journal of Power Sources*, 195(11):3431–3450, June 2010.

[8] Luca Artiglia, Stefano Agnoli, Andrea Vittadini, Alberto Verdini, Albano Cossaro, Luca Floreano, and Gaetano Granozzi. Atomic structure and special reactivity toward methanol oxidation of vanadia nanoclusters on tio2(110). *Journal of the American Chemical Society*, 135(46):17331–17338, 2013.

[9] VS Bagotzky, Yu B Vassiliev, and OA Khazova. Generalized scheme of chemisorption, electrooxidation and electroreduction of simple organic compounds on platinum group metals. *Journal of Electroanalytical Chemistry and Interfacial Electrochemistry*, 81(2):229–238, 1977.

[10] Austin M Barnes, Brendan Liu, and Steven K Buratto. Humidity-dependent surface structure and hydroxide conductance of a model quaternary ammonium anion exchange membrane. *Langmuir*, 35(44):14188–14193, 2019.

[11] Keith M Beers, Daniel T Hallinan Jr, Xin Wang, John A Pople, and Nitash P Balsara. Counterion condensation in nafion. *Macromolecules*, 44(22):8866–8870, 2011.

[12] Hector Beltran, Pablo Ayuso, and Emilio Pérez. Lifetime expectancy of li-ion batteries used for residential solar storage. *Energies*, 13(3):568, 2020.

[13] Jay Benziger, Andrew Bocarsly, May Jean Cheah, Paul Majsztrik, Barclay Satterfield, and Qiao Zhao. Mechanical and transport properties of nafion: Effects of temperature and water activity. *Fuel Cells and Hydrogen Storage*, pages 85–113, 2011.

[14] Enrico Berretti, Luigi Osmieri, Vincenzo Baglio, Hamish A. Miller, Jonathan Filippi, Francesco Vizza, Monica Santamaria, Stefania Specchia, Carlo Santoro, and Alessandro Lavacchi. Direct alcohol fuel cells: A comparative review of acidic and alkaline systems. *Electrochemical Energy Reviews*, 6(1), August 2023.

[15] P. E. Blöchl. Projector augmented-wave method. *Physical Review B*, 50(24):17953–17979, 1994.

[16] Nikolai F. Bunkin, Valeriy A. Kozlov, Alexey V. Shkirin, Barry W. Ninham, Anatoliy A. Balashov, and Sergey V. Gudkov. Dynamics of nafion membrane swelling in h2o/d2o mixtures as studied using ftir technique. *The Journal of Chemical Physics*, 148(12), March 2018.

[17] Hakan Burhan, Kemal Cellat, Gazi Yılmaz, and Fatih Şen. Direct methanol fuel cells (dmfcs). *Direct Liquid Fuel Cells*, page 71–94, 2021.

[18] Nancy A Burnham and Richard J Colton. Measuring the nanomechanical properties and surface forces of materials using an atomic force microscope. *Journal of Vacuum Science & Technology A: Vacuum, Surfaces, and Films*, 7(4):2906–2913, 1989.

[19] David A Bussian, James R O'Dea, Horia Metiu, and Steven K Buratto. Nanoscale current imaging of the conducting channels in proton exchange membrane fuel cells. *Nano Letters*, 7(2):227–232, 2007.

[20] Hans-Jüurgen Butt. Electrostatic interaction in atomic force microscopy. *Biophysical journal*, 60(4):777–785, 1991.

[21] Steven G. Chalk and James F. Miller. Key challenges and recent progress in batteries, fuel cells, and hydrogen storage for clean energy systems. *Journal of Power Sources*, 159(1):73–80, September 2006.

[22] RR Chandran, RS Yeo, and D-T Chin. Sorption and transport behavior of perfluorinated ionomer membranes in concentrated naoh solution. *Electrochimica acta*, 30(12):1585–1590, 1985.

[23] Jiří Charvát, Petr Mazúr, Martin Paidar, Jaromír Pocedič, Jiří Vrána, Jindřich Mrlík, and Juraj Kosek. The role of ion exchange membrane in vanadium oxygen fuel cell. *Journal of Membrane Science*, 629:119271, 2021.

[24] Yuqing Chen, Yuqiong Kang, Yun Zhao, Li Wang, Jilei Liu, Yanxi Li, Zheng Liang, Xiangming He, Xing Li, Naser Tavajohi, et al. A review of lithium-ion battery safety concerns: The issues, strategies, and testing standards. *Journal of Energy Chemistry*, 59:83–99, 2021.

[25] Chanyong Choi, Soohyun Kim, Riyul Kim, Yunsuk Choi, Soowhan Kim, Ho-young Jung, Jung Hoon Yang, and Hee-Tak Kim. A review of vanadium electrolytes for vanadium redox flow batteries. *Renewable and Sustainable Energy Reviews*, 69:263–274, 2017.

[26] Steeve Chrétien and Horia Metiu. Electronic structure of partially reduced rutile tio2(110) surface: Where are the unpaired electrons located? *The Journal of Physical Chemistry C*, 115(11):4696–4705, 2011.

[27] Eleanor H Cwirko and Ruben G. Carbonell. Ionic equilibria in ion-exchange membranes: a comparison of pore model predictions with experimental results. *Journal of Membrane Science*, 67(2):211–226, 1992.

[28] Robert M Darling, Adam Z Weber, Michael C Tucker, and Mike L Perry. The influence of electric field on crossover in redox-flow batteries. *Journal of The Electrochemical Society*, 163(1):A5014, 2015.

[29] Nuno M Delgado, Ricardo Monteiro, M Abdollahzadeh, Paulo Ribeirinha, Anders Bentien, and Adélio Mendes. 2d-dynamic phenomenological modelling of vanadium redox flow batteries–analysis of the mass transport related overpotentials. *Journal of Power Sources*, 480:229142, 2020.

[30] Nicholas W. DeLuca and Yossef A. Elabd. Polymer electrolyte membranes for the direct methanol fuel cell: A review. *Journal of Polymer Science Part B: Polymer Physics*, 44(16):2201–2225, July 2006.

[31] The Nam Long Doan, Tuan K. A. Hoang, and P. Chen. Recent development of polymer membranes as separators for all-vanadium redox flow batteries. *RSC Advances*, 5(89):72805–72815, 2015.

[32] Andrey V Dobrynin, Ralph H Colby, and Michael Rubinstein. Scaling theory of polyelectrolyte solutions. *Macromolecules*, 28(6):1859–1871, 1995.

[33] Frederick George Donnan. The theory of membrane equilibria. *Chemical reviews*, 1(1):73–90, 1924.

[34] Nicholas Economou. *Investigation of Morphology and Proton Conductivity in Proton Exchange Membranes under Variable Operating Conditions by Atomic Force Microscopy*. PhD thesis, University of California, Santa Barbara, 2014.

[35] Nicholas J Economou, Austin M Barnes, Andrew J Wheat, Mark S Schaberg, Steven J Hamrock, and Steven K Buratto. Investigation of humidity dependent surface morphology and proton conduction in multi-acid side chain membranes by conductive probe atomic force microscopy. *The Journal of Physical Chemistry B*, 119(44):14280–14287, 2015.

[36] Khaled Elsaid, Shereen Abdelfatah, Ahmed Maher Abdel Elabsir, Raid J. Hassiba, Zafar Khan Ghouri, and Luc Vechot. Direct alcohol fuel cells: Assessment of the fuel's safety and health aspects. *International Journal of Hydrogen Energy*, 46(59):30658–30668, August 2021.

[37] Marianne Engeser, Thomas Weiske, Detlef Schröder, and Helmut Schwarz. Oxidative degradation of small cationic vanadium clusters by molecular oxygen: On the way from v n+(n= 2- 5) to vo m+(m= 1, 2). *The Journal of Physical Chemistry A*, 107(16):2855–2859, 2003.

[38] Henry Eyring. The activated complex in chemical reactions. *The Journal of Chemical Physics*, 3(2):107–115, February 1935.

[39] Emanuele Finazzi, Cristiana Di Valentin, Gianfranco Pacchioni, and Annabella Selloni. Excess electron states in reduced bulk anatase tio2: Comparison of standard gga, gga+u, and hybrid dft calculations. *The Journal of Chemical Physics*, 129(15), 2008.

[40] Ricardo García and Alvaro San Paulo. Attractive and repulsive tip-sample interaction regimes in tapping-mode atomic force microscopy. *Physical Review B*, 60(7):4961–4967, August 1999.

[41] Xiaolin Ge, Fan Zhang, Liang Wu, Zhengjin Yang, and Tongwen Xu. Current challenges and perspectives of polymer electrolyte membranes. *Macromolecules*, 55(10):3773–3787, May 2022.

[42] Timothy D Gierke, GE Munn, and FCd Wilson. The morphology in nafion perfluorinated membrane products, as determined by wide-and small-angle x-ray studies. *Journal of Polymer Science: Polymer Physics Edition*, 19(11):1687–1704, 1981.

[43] Liyuan Gong, Zhiyuan Yang, Kui Li, Wei Xing, Changpeng Liu, and Junjie Ge. Recent development of methanol electrooxidation catalysts for direct methanol fuel cell. *Journal of Energy Chemistry*, 27(6):1618–1628, November 2018.

[44] R GOSALAWIT, S CHIRACHANCHAI, S SHISHATSKIY, and S NUNES. Krytox–montmorillonite–nafion® nanocomposite membrane for effective methanol crossover reduction in dmfcs. *Solid State Ionics*, 178(29–30):1627–1635, December 2007.

[45] Stefan Grimme, Jens Antony, Stephan Ehrlich, and Helge Krieg. A consistent and accurate ab initio parametrization of density functional dispersion correction (dft-d) for the 94 elements h-pu. *The Journal of Chemical Physics*, 132(15), 2010.

[46] Lorenz Gubler. Membranes and separators for redox flow batteries. *Current Opinion in Electrochemistry*, 18:31–36, 2019.

[47] Yun Guo, Jie Huang, and Jun-Kai Feng. Research progress in preparation of electrolyte for all-vanadium redox flow battery. *Journal of Industrial and Engineering Chemistry*, 118:33–43, February 2023.

[48] Graeme Henkelman, Gísli Jóhannesson, and Hannes Jónsson. Methods for finding saddle points and minimum energy paths. *Theoretical methods in condensed phase chemistry*, pages 269–302, 2002.

[49] A Herrera and HL Yeager. Halide and sulfate ion diffusion in nafion membranes. *Journal of The Electrochemical Society*, 134(10):2446, 1987.

[50] R Hiesgen, E Aleksandrova, G Meichsner, I Wehl, E Roduner, and K Andreas Friedrich. High-resolution imaging of ion conductivity of nafion® membranes with electrochemical atomic force microscopy. *Electrochimica Acta*, 55(2):423–429, 2009.

[51] Renate Hiesgen, Stefan Helmly, Tobias Morawietz, Xiao-Zi Yuan, Haijiang Wang, and K Andreas Friedrich. Atomic force microscopy studies of conductive nanostructures in solid polymer electrolytes. *Electrochimica Acta*, 110:292–305, 2013.

[52] Renate Hiesgen, Tobias Morawietz, Michael Handl, Martina Corasaniti, and K Andreas Friedrich. Atomic force microscopy on cross sections of fuel cell membranes, electrodes, and membrane electrode assemblies. *Electrochimica Acta*, 162:86–99, 2015.

[53] Burak Himmetoglu, Andrea Floris, Stefano de Gironcoli, and Matteo Cococcioni. Hubbard-corrected dft energy functionals: The lda+u description of correlated systems. *International Journal of Quantum Chemistry*, 114(1):14–49, July 2013.

[54] Nadia N Intan, Konstantin Klyukin, Tawanda J Zimudzi, Michael A Hickner, and Vitaly Alexandrov. A combined theoretical-experimental study of interactions between vanadium ions and nafion membrane in all-vanadium redox flow batteries. *Journal of Power Sources*, 373:150–160, 2018.

[55] Brian David James, Jennie Moton Huya-Kouadio, Cassidy Houchins, and Daniel Allen DeSantis. Mass production cost estimation of direct h2 pem fuel cell systems for transportation applications (2012-2016). Technical report, Strategic Analysis Inc., Arlington, VA (United States), 2016.

[56] PJ James, M Antognozzi, J Tamayo, TJ McMaster, JM Newton, and MJ Miles. Interpretation of contrast in tapping mode afm and shear force microscopy. a study of nafion. *Langmuir*, 17(2):349–360, 2001.

[57] PJ James, JA Elliott, TJ McMaster, JM Newton, AMS Elliott, S Hanna, and MJ Miles. Hydration of nafion® studied by afm and x-ray scattering. *Journal of Materials Science*, 35:5111–5119, 2000.

[58] Sanghyun Jeong, Lae-Hyun Kim, Yongchai Kwon, and Sunhoe Kim. Effect of nafion membrane thickness on performance of vanadium redox flow battery. *Korean Journal of Chemical Engineering*, 31:2081–2087, 2014.

[59] Bo Jiang, Lantao Wu, Lihong Yu, Xinping Qiu, and Jingyu Xi. A comparative study of nafion series membranes for vanadium redox flow batteries. *Journal of Membrane Science*, 510:18–26, 2016.

[60] Rongzhong Jiang and Deryn Chu. Comparative studies of methanol crossover and cell performance for a dmfc. *Journal of The Electrochemical Society*, 151(1):A69, 2004.

[61] Shengjuan Jiang, Shanfu Lu, Yan Xiang, and San Ping Jiang. The structure–activity relationship in membranes for vanadium redox flow batteries. *Advanced Sustainable Systems*, 3(8):1900020, 2019.

[62] Guo-Bin Jung, Ay Su, Cheng-Hsin Tu, and Fang-Bor Weng. Effect of operating parameters on the dmfc performance. *Journal of Fuel Cell Science and Technology*, 2(2):81–85, August 2004.

[63] S.K. Kamarudin, F. Achmad, and W.R.W. Daud. Overview on the application of direct methanol fuel cell (dmfc) for portable electronic devices. *International Journal of Hydrogen Energy*, 34(16):6902–6916, 2009. 4th Dubrovnik Conference.

[64] K Kimoto. Water absorption and donnan equilibria of perfluoro ionomer membranes for the chlor-alkali process. *Journal of The Electrochemical Society*, 130(2):334, 1983.

[65] KW Knehr, Ertan Agar, CR Dennison, AR Kalidindi, and EC Kumbur. A transient vanadium flow battery model incorporating vanadium crossover and water transport through the membrane. *Journal of The Electrochemical Society*, 159(9):A1446, 2012.

[66] M Koinuma and K Uosaki. An electrochemical afm study on electrodeposition of copper on p-gaas (100) surface in hcl solution. *Electrochimica acta*, 40(10):1345–1351, 1995.

[67] Karl Kordesch, Viktor Hacker, Josef Gsellmann, Martin Cifrain, Gottfried Faleschini, Peter Enzinger, Robert Fankhauser, Markus Ortner, Michael Muhr, and Robert R. Aronson. Alkaline fuel cells applications. *Journal of Power Sources*, 86(1–2):162–165, March 2000.

[68] G. Kresse and J. Hafner. Ab initiomolecular dynamics for liquid metals. *Physical Review B*, 47(1):558–561, 1993.

[69] G. Kresse and D. Joubert. From ultrasoft pseudopotentials to the projector augmented-wave method. *Physical Review B*, 59(3):1758–1775, 1999.

[70] Henrik H. Kristoffersen, Hunter L. Neilson, Steven K. Buratto, and Horia Metiu. Stability of v2o5 supported on titania in the presence of water, bulk oxygen vacancies, and adsorbed oxygen atoms. *The Journal of Physical Chemistry C*, 121(15):8444–8451, April 2017.

[71] Yo Han Kwon, Sung Chul Kim, and Sang-Young Lee. Nanoscale phase separation of sulfonated poly(arylene ether sulfone)/poly(ether sulfone) semi-ipns for dmfc membrane applications. *Macromolecules*, 42(14):5244–5250, July 2009.

[72] Tiago Lagarteira, Pedro Pacheco, Carlos Almeida, Anders Bentien, Ricardo Monteiro, and Adélio Mendes. In-situ measurement of vanadium crossover for the vanadium redox flow battery. *Journal of The Electrochemical Society*, 166(16):A4067, 2019.

[73] A Lehmani, S Durand-Vidal, and P Turq. Surface morphology of nafion 117 membrane by tapping mode atomic force microscope. *Journal of applied polymer science*, 68(3):503–508, 1998.

[74] Xianfeng Li, Huamin Zhang, Zhensheng Mai, Hongzhang Zhang, and Ivo Vankelecom. Ion exchange membranes for vanadium redox flow battery (vrb) applications. *Energy & Environmental Science*, 4(4):1147–1160, 2011.

[75] Hyebin Lim, S Yi Jung, and Doohwan Lee. Operando studies on through-plane cell voltage losses in vanadium redox flow battery. *Journal of Power Sources*, 422:65–72, 2019.

[76] Dongju Liu and Jian Yu. Otsu method and k-means. In *2009 Ninth International conference on hybrid intelligent systems*, volume 1, pages 344–349. IEEE, 2009.

[77] Hansan Liu, Chaojie Song, Lei Zhang, Jiujun Zhang, Haijiang Wang, and David P. Wilkinson. A review of anode catalysis in the direct methanol fuel cell. *Journal of Power Sources*, 155(2):95–110, April 2006.

[78] J.G. Liu, T.S. Zhao, R. Chen, and C.W. Wong. The effect of methanol concentration on the performance of a passive dmfc. *Electrochemistry Communications*, 7(3):288–294, March 2005.

[79] Kyle Lourenssen, James Williams, Faraz Ahmadpour, Ryan Clemmer, and Syeda Tasnim. Vanadium redox flow batteries: A comprehensive review. *Journal of Energy Storage*, 25:100844, October 2019.

[80] Qingtao Luo, Liyu Li, Wei Wang, Zimin Nie, Xiaoliang Wei, Bin Li, Baowei Chen, Zhenguo Yang, and Vincent Sprenkle. Capacity decay and remediation of nafion-based all-vanadium redox flow batteries. *ChemSusChem*, 6(2):268–274, 2013.

[81] Gerald S Manning. Limiting laws and counterion condensation in polyelectrolyte solutions i. colligative properties. *The journal of chemical Physics*, 51(3):924–933, 1969.

[82] Jan Martin, Katharina Schafner, and Thomas Turek. Preparation of electrolyte for vanadium redox-flow batteries based on vanadium pentoxide. *Energy Technology*, 8(9), August 2020.

[83] Maximiliano Martínez, Marcelo Gustavo Molina, and Pedro Enrique Mercado. Optimal sizing method of vanadium redox flow battery to provide load frequency control in power systems with intermittent renewable generation. *IET Renewable Power Generation*, 11(14):1804–1811, 2017.

[84] Kenneth A Mauritz and Robert B Moore. State of understanding of nafion. *Chemical reviews*, 104(10):4535–4586, 2004.

[85] R Scott McLean, Marc Doyle, and Bryan B Sauer. High-resolution imaging of ionic domains and crystal morphology in ionomers using afm techniques. *Macromolecules*, 33(17):6541–6550, 2000.

[86] MR Mohamed, PK Leung, and MH Sulaiman. Performance characterization of a vanadium redox flow battery at different operating parameters under a standardized test-bed system. *Applied energy*, 137:402–412, 2015.

[87] Jens Noack, Gwenn Cognard, Meryem Oral, Michael Küttinger, Nataliya Roznyatovskaya, Karsten Pinkwart, and Jens Tübke. Study of the long-term operation of a vanadium/oxygen fuel cell. *Journal of Power Sources*, 326:137–145, 2016.

[88] Jens Noack, Carsten Cremers, Domnik Bayer, Jens Tübke, and Karsten Pinkwart. Development and characterization of a 280 cm2 vanadium/oxygen fuel cell. *Journal of Power Sources*, 253:397–403, 2014.

[89] Daniela Oboroceanu, Nathan Quill, Catherine Lenihan, Deirdre Ní Eidhin, Sergiu Petru Albu, Robert Patrick Lynch, and D. Noel Buckley. Stability of catholytes in vanadium redox flow batteries and the kinetics of precipitation of vv. *ECS Meeting Abstracts*, MA2016-02(1):32–32, September 2016.

[90] James O'dea. *Probing ion conducting domains and localizing catalysts in proton exchange membrane fuel cells*. PhD thesis, University of California, Santa Barbara, 2010.

[91] Sara Noriega Oreiro, Perizat Berdiyeva, and Anders Bentien. Facile density measurement method for high-concentration sulfate determination. *ECS Advances*, 1(4):042501, November 2022.

[92] James R O'Dea and Steven K Buratto. Phase imaging of proton exchange membranes under attractive and repulsive tip- sample interaction forces. *The Journal of Physical Chemistry B*, 115(5):1014–1020, 2011.

[93] Stephen J Paddison and Reginald Paul. The nature of proton transport in fully hydrated nafion®. *Physical Chemistry Chemical Physics*, 4(7):1158–1163, 2002.

[94] Mingzhang Pan, Chengjie Pan, Chao Li, and Jian Zhao. A review of membranes in proton exchange membrane fuel cells: Transport phenomena, performance and durability. *Renewable and Sustainable Energy Reviews*, 141:110771, 2021.

[95] Jong Ho Park, Jung Jin Park, Hyun Ju Lee, Byung Seok Min, and Jung Hoon Yang. Influence of metal impurities or additives in the electrolyte of a vanadium redox flow battery. *Journal of The Electrochemical Society*, 165(7):A1263, 2018.

[96] Peter N Pintauro and Douglas N Bennion. Mass transport of electrolytes in membranes. 2. determination of sodium chloride equilibrium and transport parameters for nafion. *Industrial & engineering chemistry fundamentals*, 23(2):234–243, 1984.

[97] Scott P. Price, Xiao Tong, Claron Ridge, Vladimir Shapovalov, Zhenpeng Hu, Paul Kemper, Horia Metiu, Michael T. Bowers, and Steven K. Buratto. Stm characterization of size-selected v1, v2, vo, and vo2 clusters on a tio2(110)-(1×1) surface at room temperature. *Surface Science*, 605(9–10):972–976, 2011.

[98] Helen Prifti, Aishwarya Parasuraman, Suminto Winardi, Tuti Mariana Lim, and Maria Skyllas-Kazacos. Membranes for redox flow battery applications. *Membranes*, 2(2):275–306, 2012.

[99] A Ranjan, KL Pey, and SJ O'Shea. The interplay between drift and electrical measurement in conduction atomic force microscopy. *Review of Scientific Instruments*, 90(7), 2019.

[100] Mandar Risbud, Chris Menictas, Maria Skyllas-Kazacos, and Jens Noack. Vanadium oxygen fuel cell utilising high concentration electrolyte. *Batteries*, 5(1):24, 2019.

[101] J.C. Robins. *Fundamental Studies on the Origin of the Support Effect in VO/TiO2 (110) Model Catalysts*. PhD thesis, University of California, Santa Barbara, 2019.

[102] Nataliya Roznyatovskaya, Jens Noack, Karsten Pinkwart, and Jens Tübke. Aspects of electron transfer processes in vanadium redox-flow batteries. *Current Opinion in Electrochemistry*, 19:42–48, 2020.

[103] V Saarinen, KD Kreuer, Michael Schuster, R Merkle, and J Maier. On the swelling properties of proton conducting membranes for direct methanol fuel cells. *Solid State Ionics*, 178(7-10):533–537, 2007.

[104] Klaus Schmidt-Rohr and Qiang Chen. Parallel cylindrical water nanochannels in nafion fuel-cell membranes. *Nature materials*, 7(1):75–83, 2008.

[105] Birgit Schwenzer, Jianlu Zhang, Soowhan Kim, Liyu Li, Jun Liu, and Zhenguo Yang. Membrane development for vanadium redox flow batteries. *ChemSusChem*, 4(10):1388–1406, October 2011.

[106] N. Shahrubudin, T.C. Lee, and R. Ramlan. An overview on 3d printing technology: Technological, materials, and applications. *Procedia Manufacturing*, 35:1286–1296, 2019.

[107] Vladimir Shapovalov and Horia Metiu. Vox (x = 14) submonolayers supported on rutile tio2(110) and ceo2(111) surfaces: The structure, the charge of the atoms, the xps spectrum, and the equilibrium composition in the presence of oxygen. *The Journal of Physical Chemistry C*, 111(38):14179–14188, 2007.

[108] Yu Shi, Chika Eze, Binyu Xiong, Weidong He, Han Zhang, Tuti Mariana Lim, A Ukil, and Jiyun Zhao. Recent development of membrane for vanadium redox flow battery applications: A review. *Applied Energy*, 238:202–224, 2019.

[109] Z Siroma and K Yasuda. Imaging of ion channels on the surface of recast nafion film by current-sensing atomic force microscopy. *ITE LETTERS ON BATTERIES NEW TECHNOLOGIES AND MEDICINE*, 6(3):B5, 2005.

[110] M. Skyllas-Kazacos, M. Rychcik, R. G. Robins, A. G. Fane, and M. A. Green. New all-vanadium redox flow cell. *Journal of The Electrochemical Society*, 133(5):1057–1058, May 1986.

[111] M Stopka, L Hadjiiski, E Oesterschulze, and R Kassing. Surface investigations by scanning thermal microscopy. *Journal of Vacuum Science & Technology B: Microelectronics and Nanometer Structures Processing, Measurement, and Phenomena*, 13(6):2153–2156, 1995.

[112] Rahul Sujanani, Lynn E. Katz, Donald R. Paul, and Benny D. Freeman. Aqueous ion partitioning in nafion: Applicability of manning's counter-ion condensation theory. *Journal of Membrane Science*, 638:119687, November 2021.

[113] Chenxi Sun, Jian Chen, Huamin Zhang, Xi Han, and Qingtao Luo. Investigations on transfer of water and vanadium ions across nafion membrane in an operating vanadium redox flow battery. *Journal of Power Sources*, 195(3):890–897, 2010.

[114] Miriam M. Tellez-Cruz, Jorge Escorihuela, Omar Solorza-Feria, and Vicente Compañ. Proton exchange membrane fuel cells (pemfcs): Advances and challenges. *Polymers*, 13(18):3064, September 2021.

[115] Baye Gueye Thiam and Sébastien Vaudreuil. Recent membranes for vanadium redox flow batteries. *Journal of The Electrochemical Society*, 168(7):070553, 2021.

[116] Nobuyuki Tokuda, Takahiro Kumamoto, Toshio Shigematsu, Hiroshige Deguchi, Takefumi Ito, Noriyasu Yoshikawa, and Takushi Hara. Development of a redox flow battery system. *SUMITOMO ELECTRIC TECHNICAL REVIEW-ENGLISH EDITION-*, pages 88–94, 1998.

[117] Xiao Tong, Scott P. Price, Jeremy C. Robins, Claron Ridge, Hyun You Kim, Paul Kemper, Horia Metiu, Michael T. Bowers, and Steven K. Buratto. Vo cluster-stabilized h2o adsorption on a tio2 (110) surface at room temperature. *The Journal of Physical Chemistry C*, 126(42):17975–17982, 2022.

[118] Vilayanur Viswanathan, Alasdair Crawford, David Stephenson, Soowhan Kim, Wei Wang, Bin Li, Greg Coffey, Ed Thomsen, Gordon Graff, Patrick Balducci, et al. Cost and performance model for redox flow batteries. *Journal of Power Sources*, 247:1040–1051, 2014.

[119] Jiří Vrána, Jiří Charvát, Petr Mazúr, Petr Bělskỳ, Jan Dundálek, Jaromír Pocedič, and Juraj Kosek. Commercial perfluorosulfonic acid membranes for vanadium redox flow battery: Effect of ion-exchange capacity and membrane internal structure. *Journal of Membrane Science*, 552:202–212, 2018.

[120] Xin Xie, Osung Kwon, Da-Ming Zhu, Trung Van Nguyen, and Guangyu Lin. Local probe and conduction distribution of proton exchange membranes. *The Journal of Physical Chemistry B*, 111(22):6134–6140, 2007.

[121] X.-L. Yin, M. Calatayud, H. Qiu, Y. Wang, A. Birkner, C. Minot, and Ch. Wöll. Diffusion versus desorption: Complex behavior of h atoms on an oxide surface. *ChemPhysChem*, 9(2):253–256, 2008.

[122] C. Zhang, T.S. Zhao, Q. Xu, L. An, and G. Zhao. Effects of operating temperature on the performance of vanadium redox flow batteries. *Applied Energy*, 155:349–353, October 2015.

[123] Lesi Zhang, Ling Ling, Min Xiao, Dongmei Han, Shuanjin Wang, and Yuezhong Meng. Effectively suppressing vanadium permeation in vanadium redox flow battery application with modified nafion membrane with nacre-like nanoarchitectures. *Journal of Power Sources*, 352:111–117, June 2017.

[124] Yang Zhao, Le Liu, Xinping Qiu, and Jingyu Xi. Revealing sulfuric acid concentration impact on comprehensive performance of vanadium electrolytes and flow batteries. *Electrochimica Acta*, 303:21–31, April 2019.

[125] Yang Zhao, Le Liu, Xinping Qiu, and Jingyu Xi. Revealing sulfuric acid concentration impact on comprehensive performance of vanadium electrolytes and flow batteries. *Electrochimica Acta*, 303:21–31, April 2019.

[126] John G Ziegler and Nathaniel B Nichols. Optimum settings for automatic controllers. *Transactions of the American society of mechanical engineers*, 64(8):759–765, 1942.